2015-09-29

Effective Thermal Conductivity of Porous Media: An Integrated Approach

Skripkin, Evgeny

UNIVERSITY OF CALGARY

Effective Thermal Conductivity of Porous Media: An Integrated Approach

by

Evgeny Skripkin

A THESIS

SUBMITTED TO THE FACULTY OF GRADUATE STUDIES

IN PARTIAL FULFILMENT OF THE REQUIREMENTS FOR THE

DEGREE OF MASTER OF SCIENCE

GRADUATE PROGRAM IN CHEMICAL AND PETROLEUM ENGINEERING

CALGARY, ALBERTA

SEPTEMBER, 2015

Abstract

In this thesis an integrated approach to predict the effective thermal conductivity of porous media is presented. A pore scale level heat transfer model is developed and used to generate a custom mixing rule for thermal conductivity prediction. The novel mixing rule is developed based on particle size distribution data for unconsolidated porous media. The fluid and solid phase are considered, with fluid phase being stagnant. The point contact between the grains and spherical shape of the grains are also assumed. The model and mixing rule are validated and sensitivity analysis is performed.

The question of upscaling the results of pore scale level modeling is also addressed. Two approaches are presented: equivalent network model and upscaling using computer tomography images. Equivalent network model was validated using model-by-model validation approach. Computer tomography images upscaling approach was applied to predict the scaled up thermal conductivity of oil sand core samples.

Acknowledgements

Dedicated to my daughter Alexandra Skripkina

Table of contents

List of tables

List of figures

x

List of symbols and abbreviations

Symbols:

A	Matrix of connections (Section 5.1)
a, c, d	Coefficients in Woodside-Messmer model (Section 2.4)
a, b, c, d	Sigmoid mixing rule parameters (Section 4.1)
a_{ij}	Elements of matrix A (Section 5.1)
$a_1, a_2, a_3, \theta_0, n, \phi_1, \phi_2$	Coefficients of Kunii-Smith model (Section 2.4)
B	Coefficient in Zehner-Schlunder model (Section 2.4)
CT	CT number (Section 5.3)
c_p	Specific heat capacity at constant pressure (Section 2.2)
D_p	Mean particle (grain, bead) diameter (Section 2.5)
d	Particle diameter; distance between two spheres in Chapter 3, Numerical experiment #01 (Section 3.3)
ds	Surface element (Section 3.2)
dv	Volume element (Section 3.2)
$\boldsymbol{e}$	Column vector of sources of electromotive forces (Section 5.1)
GS	Greyscale value (Section 5.3)
I	Electrical current through at the edge of EMF source (Section 5.1)
I_k	Electrical current going to or from node k (Section 5.1)
J	Density of electrical current (Section 5.1)
$\boldsymbol{j}$	Column vector of sources of electrical current in edges (Section 5.1)
K_e	Effective thermal conductivity normalized by fluid thermal conductivity (Section 2.4)
K_s	Solid thermal conductivity normalized by fluid thermal conductivity (solid to fluid thermal conductivity ratio) (Section 2.4)
$\boldsymbol{k}$	Thermal conductivity tensor (Section 2.1)
k	Thermal conductivity (Section 2.1)
k_{eq}	Equivalent value of a property (electrical conductivity, thermal

	conductivity, fluid mobility) (Section 5.1)
k_f	Fluid thermal conductivity (Section 2.3)
k_g	Thermal conductivity of gas (Section 4.4)
k_{grain}	Grain thermal conductivity (Section 5.3)
k_i	Thermal conductivity of phase i, where i can take one of the values o, w or g (Section 4.4)
k_{ij}	Thermal conductivity in i direction when the temperature gradient is applied in j direction, where i and j can take one of the values x, y or z (Section 2.1)
k_{mask}	Effective thermal conductivity of a mask (Section 5.3)
k_o	Thermal conductivity of oil (Section 4.4)
k_s	Solid thermal conductivity (Section 2.3)
k_s	Thermal conductivity of sand (Section 4.4)
k_w	Thermal conductivity of water (Section 4.4)
k_1	Value of a property (electrical conductivity, thermal conductivity, fluid mobility) in block 1 (Section 5.1)
k_2	Value of a property (electrical conductivity, thermal conductivity, fluid mobility) in block 2 (Section 5.1)
k_e^i	Effective thermal conductivity of porous media saturated with phase i, where i can take one of the values o, w or g (Section 4.4)
ln	Natural logarithm (Section 2.4)
log	Logarithm to base 10 (Section 2.4)
m, b	Slope and intercept of CT calibration line (Section 5.3)
n_{fs}	Vector normal to the fluid-solid interface (Section 2.3)
P	Pressure (Section 5.1)
phi	Units used in grain size distribution data (Section 3.1)
$\boldsymbol{q}$	Heat flux density vector (Section 2.1)
q	One dimensional heat flux density (Section 2.1)

q_{ave}	Average one dimensional heat flux density (Section 3.2)
r_s	Sphere radius (Section 3.3)
S_g	Gas saturation (Section 4.4)
S_o	Oil saturation (Section 4.4)
S_w	Water saturation (Section 4.4)
T	Temperature (Section 2.1)
T_f	Temperature of fluid phase (Section 2.3)
T_s	Temperature of solid phase (Section 2.3)
T_1, T_2	Temperature values at opposite boundaries (Section 3.2)
U	Voltage of electromotive forces source (Section 5.1)
u	Fluid velocity (Section 5.1)
$\boldsymbol{u}_0$	Column vector of node potentials (Section 5.1)
$\boldsymbol{u}_{oi}$	Voltage at edge i (Section 5.1)
V	Total volume of porous media sample (Section 3.2)
V_L	Volume of liquid (Section 3.2)
V_k	Potential difference at the edge k (Section 5.1)
x	Spatial variable along X coordinate direction (Section 2.1)
x_1, x_2	X-coordinates of opposite boundaries (Section 3.2)
Y	Matrix of electrical conductivities of edges (Section 5.1)
Y_{eq}	Equivalent electrical conductivity of a network (Section 5.1)
Y_{ii}	Electrical conductivity of edge i (Section 5.1)
y	Spatial variable along Y coordinate direction (Section 2.1)
y_1, y_2	Y-coordinates of opposite boundaries (Section 3.2)
z	Spatial variable along Z coordinate direction (Section 2.1)
z_1, z_2	Z-coordinates of opposite boundaries (Section 3.2)
Δ	Finite difference operator (Section 4.3)
λ	Fluid mobility (Section 5.1)
ρ	Density (Section 2.2)

ρ_b	Bulk density of porous media (Section 5.3)
ρ_{gr}	Grain density (Section 5.3)
ρ_i	Density of fluid i, where i can take one of the values o, w or g (Section 5.3)
σ	Electrical conductivity (Section 5.1)
Φ	Charge density (Section 5.1)
ϕ	Porosity (Section 2.3)
∇	Gradient (Section 2.1)
∇^2	Laplace operator (Section 2.3)

Indexes:

b	Bulk
e	Effective
eq	Equivalent
f	Fluid
fs	Fluid to solid
g	Gas
gr	Grain
o	Oil
p	Particle
s	Solid, sand, sphere
w	Water

Abbreviations:

AER	Alberta Energy Regulator
bbl	Barrel
CAD	Computer Aided Design
CFD	Computational fluid dynamics

CSOR	Cumulative Steam to Oil Ratio
CSS	Cyclic Steam Stimulation
CT	Computer Tomography
EMT	Effective Medium Theory
ERCB	Energy Resources Conservation Board
ETC	Effective thermal conductivity
GJ	Gigajoule
GS	Greyscale
MIHS	Muddy Inclined Heterolithic Stratification
MMDB	Millions of Barrels of Oil Per Day
MMBtu	Millions of British Thermal Units
NER	Net Energy Return
NMR	Nuclear Magnetic Resonance
PSD	Particle Size Distribution
SAGD	Steam Assisted Gravity Drainage
SIHS	Sandy Inclined Heterolithic Stratification
SOR	Steam to Oil Ration
TC	Thermal conductivity
USD	United States Dollar
WCSB	Western Canadian Sedimentary Basin
WTI	Western Texas Intermediate
XRD	X-ray Powder Difraction

Chapter 1: **Introduction**

Energy is one of the key factors for sustainable development of any country in the modern world. Natural resources such as oil and gas are the main contributors to the energy industry of all leading countries. According to Oil and Gas Journal (Xu and Bell 2014) Canada has estimated proven reserves around 172.5 billion barrels of oil. Proven reserves are reserves which can be recovered in an economic manner. Canadian estimated remaining ultimate potential is 339 billion barrels as of December 2012. Oil sands bitumen is the major source of crude oil in Canada: 90% of total reserves, 98% of proven reserves (National Energy Board 2013).

Alberta and Saskatchewan are the two main heavy oil and bitumen provinces in Canada. Alberta accounts for the most of the oil sands reserves. The three main oil sands areas in Alberta are Athabasca, Cold Lake and Peace River (Figure 1-1). Athabasca can be subdivided into three regions: Athabasca North, Wabiskaw and Conklin (Figure 1-2).
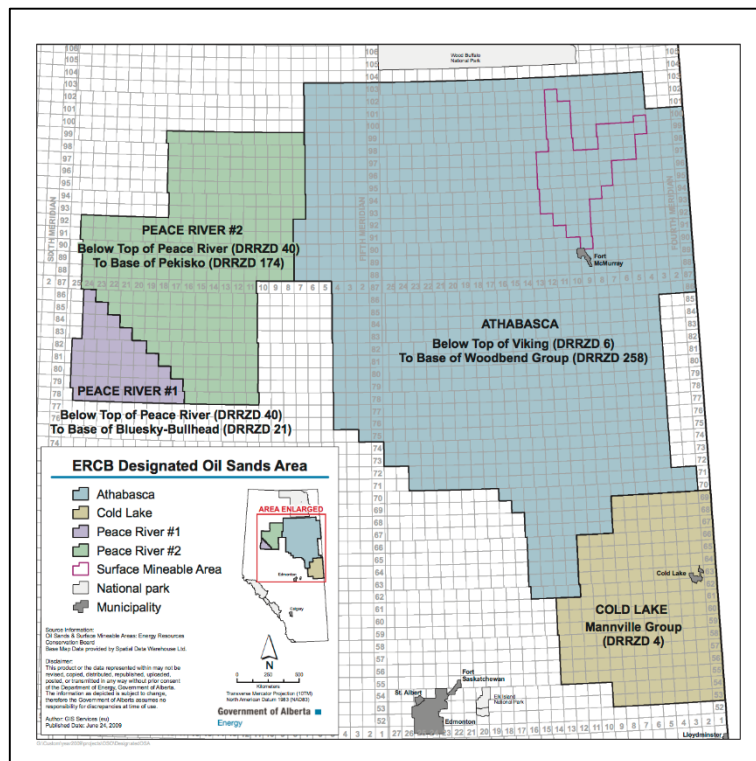
Figure 1-1 – ERCB designated oil sands area
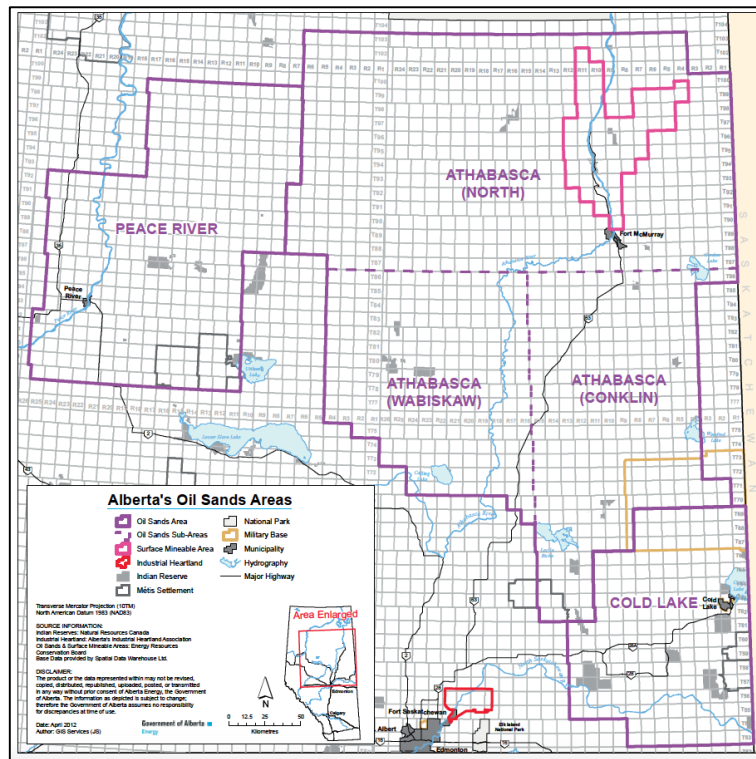
Figure 1-2 – Alberta's oil sands areas

Heavy oil and bitumen recovery technologies can be divided into two main categories: mining and in-situ. Mining involves truck and shovel technology to deliver oil sand to an extraction facility, where the bitumen is cleaned of sand and then refined or upgraded. In-situ is the technology of bitumen recovery by means of wells. In-situ methods can be classified into two major types: primary/enhanced oil recovery and thermal recovery techniques. Primary/enhanced oil recovery techniques include primary recovery (pressure drive, gas drive, water drive, etc.) and secondary and tertiary (enhanced) oil recovery (waterflooding, gas injection, chemical (polymer/surfactant/alkali/foam) flooding, etc.). The key point of thermal recovery methods is to heat the reservoir to the temperature at which the viscosity of heavy oil reduces enough for it to become mobile. Thermal recovery techniques include cyclic steam stimulation (CSS), steam assisted gravity drainage (SAGD) and their modifications.

Cyclic steam stimulation uses one well as an injector and producer. Production goes in cycles. A cycle begins with the first stage where steam is injected for a period of time into a formation under high pressure which causes the fracture of formation and thus propagation of steam for a longer distance. The second stage is soaking, when the steam gives its latent heat to formation.

The final stage of a cycle is production of heated oil for a period of time. Schematically stages are presented in Figure 1-3. After a period of time the cycle is repeated.
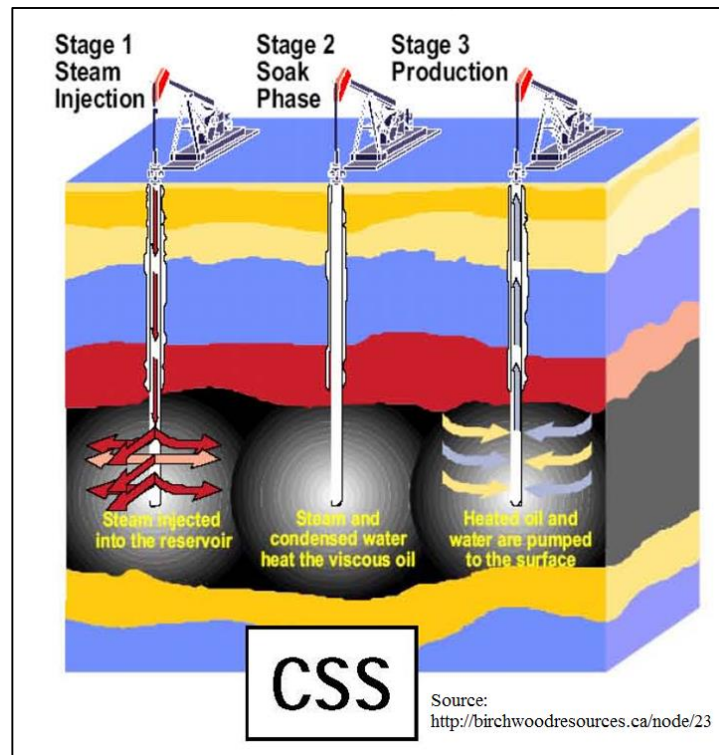
Figure 1-3 – Typical CSS cycle

Steam assisted gravity drainage uses two horizontal wells (injector and producer) one above the other. The top well is injector and the bottom well is producer (see Figure 1-4). Typical length of the horizontal section is 500 to 1000 meters. The reservoir is heated by steam injection through the top well and after a period of time a so-called steam chamber develops. Steam gives its latent heat to the formation at the edge of the steam chamber where bitumen drains under the forces of gravity into the production well.
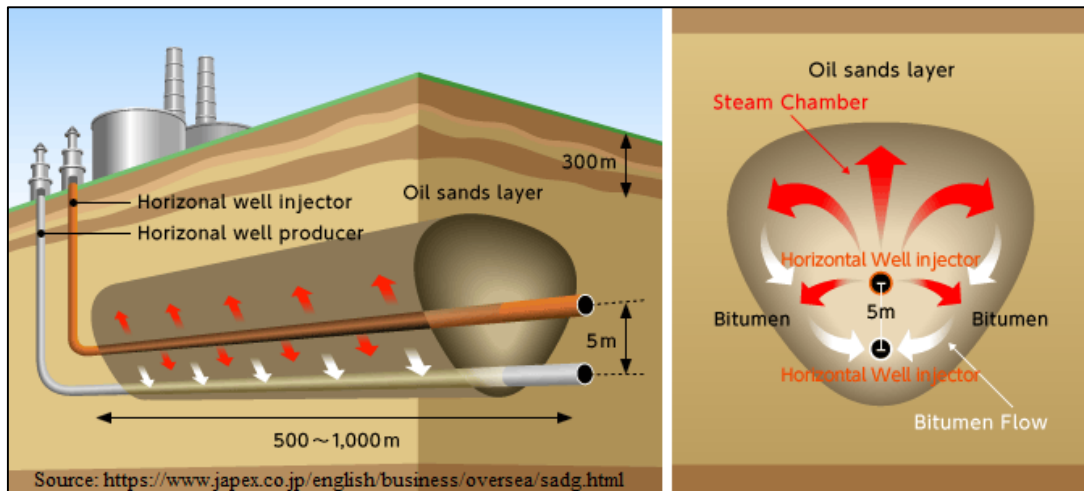
Figure 1-4 – SAGD diagram

According to the Alberta Department of Energy (Holly, Mader and Toor 2012) in 2010 the compounded growth rate was 34.2% for SAGD, 7.6% for Primary/enhanced oil recovery, 5.9% for mining and 5.3% for CSS. Also SAGD shows exponential growth, while the other types of production show linear trends. These parameters indicate that SAGD becomes more and more applicable and economically viable nowadays.

In a reference case (WTI Oil Price $110 USD/bbl, Henry Hub Natural Gas Price $6.2 USD/MMBtu) crude oil production will increase by 75% (to 5.8 MMBD) in 2035. The oil sands portion of production will increase from 57% in 2012 to 86% in 2035 (Figure 1-5). Investments in oil sands tend to shift from mining towards in-situ SAGD (National Energy Board 2013). It should be mentioned that low oil prices of 2015 will definitely adjust the forecast, but the trend will remain the same (Canadian Association of Petroleum Producers 2015).
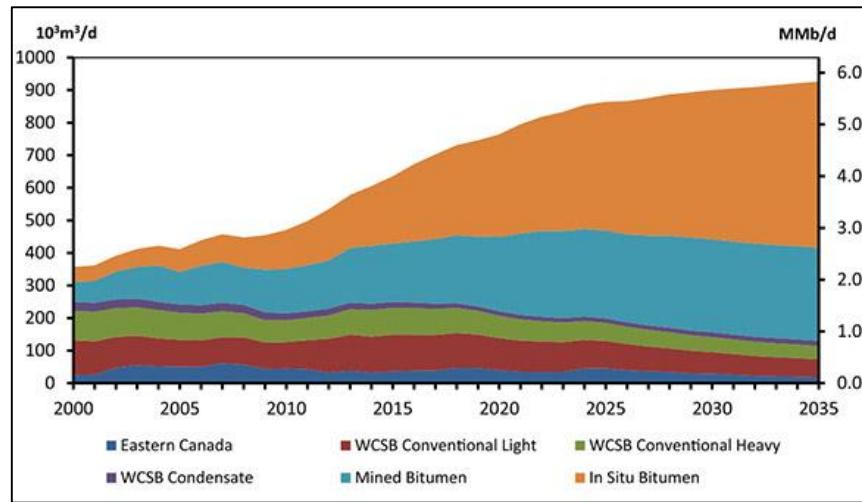
Figure 1-5 – Crude oil forecast to 2035 (National Energy Board 2013)

Energy efficiency and steam to oil ratio (SOR) are the most important economic parameters in evaluating SAGD field application. The net energy return (NER) ratio shows the amount of energy produced per amount of energy consumed (in GJ/GJ) by the technology. For SAGD NER varies from 4 to 7 GJ/GJ (Brandt, Englander and Bharadwaj 2013). Cumulative steam to oil ratio (CSOR) shows the amount of steam in cold water equivalents injected to oil produced (in m^3/m^3) for the production period of a well pair. Average CSOR of a SAGD well pair decreases with time and stabilizes around 3-4 m^3/m^3 (Gates and Larter 2014). These two parameters among others indicate that SAGD is very sensitive to the economic situation, in particular to market price of crude oil and natural gas. Thereby any enhancement to SAGD technology that will allow to improve accuracy of prediction of SAGD production rates is worth of effort and time.

Thermal recovery methods use different sources of energy to increase the temperature of heavy oil, the viscosity of which significantly decreases with temperature (several orders of magnitude). In a SAGD project the latent heat of steam is used to increase the temperature of heavy oil.

Typical SAGD project consists of a start-up phase, an intermediate phase and the normal SAGD phase. During the start-up phase steam is circulated in both horizontal wells to establish thermal communication between injector and producer. Heat is transferred primarily by conduction during the start-up phase. It is known that the effective thermal conductivity of oil sand changes with temperature (Butler 1991). During the intermediate phase (steam boost) the steam is

injected into the reservoir and displaces bitumen towards the producer. Heat is transferred by conduction and convection. As a result a so-called steam chamber develops. It is believed that mature steam chamber consists of sand, residual oil saturation, condensate and steam. The final phase is a normal SAGD production when the steam chamber is already developed. During this phase steam gives its latent heat to bitumen and condenses at the edge of the steam chamber. Condensate and heated oil drain towards the producer under the force of gravity. Heat is conducted from the edge of steam chamber toward the reservoir outside of steam chamber. In terms of composition the edge of steam chamber represents an intermediate zone between steam chamber and reservoir.

As shown above, thermal conduction plays an important role during each phase of a SAGD project. In composite materials such as oil sands heat conduction equation is usually written in terms of effective thermal conductivity of that material. It is known that thermal conductivity of oil sand depends on thermal conductivity of components (water, oil, gas and sand), temperature of oil sand material, contact area between the grains, porosity and fluid saturations (Butler 1991). The term mixing rule will be used for any formula which will allow to calculate effective thermal conductivity of porous media based on the parameters listed above.

1.1 Objectives

The primary goal of this thesis is to propose and develop an integrated approach of calculating the effective thermal conductivity of porous media type materials. In order to reach the goal of this thesis a set objectives was addressed:

- Set up a heat transfer model at a pore scale level
- Implement this model in virtual porous media
- Develop novel mixing rule for unconsolidated porous media based on particle size distribution of the media
- Validate the mixing rule with literature and experimental data
- Analyze the effects of meshing on the effective thermal conductivity
- Set up a heat transfer model at a core scale level
- Apply scaling up techniques to upscale the effective thermal conductivity from the pore scale level to the core scale level

1.2 Thesis organization

Chapter 1 of the thesis contains introduction to heavy oil industry in Canada, description of oil sands reserves, forecast in production and major thermal recovery methods. SAGD process is described in some details. Shortcomings in using effective thermal conductivity to model SAGD are discussed. The objectives of the thesis are set.

Chapter 2 describes the Fourier's Law at the pore and at the core scale levels. Literature review on calculations and measurements of effective thermal conductivity of porous media is presented. Measurement approaches and mixing rules are discussed as well as their applicability.

In Chapter 3 the pore scale modelling is addressed in detail. Methods of generation of virtual porous media geometry are provided. A pore level heat transfer model is presented. Modelling results are compared to existing mixing rules. Voxel based and geometry based meshing approaches are compared.

Chapter 4 contains a novel effective thermal conductivity mixing rule and physical explanation of its parameters. The mixing rule is based on the particle size distribution of a porous medium. Comparison of the novel mixing rule to available literature data is provided.

In Chapter 5 the scale up algorithm is presented which allows to propagate rock properties from pore scale level to core scale level and further to grid block size. A scale up approach using computer tomography (CT) images of core is described.

Main results, conclusions and recommendations for future work are presented in Chapter 6.

Chapter 2: **Overview of heat transfer in porous media**

Heat transfer in porous media is a complex process. It can include the following heat transfer related phenomena:

1. Heat transfer by conduction within fluid(s), within solids and from solid(s) to fluid(s)
2. Heat transfer by convection of fluid(s) (forced and natural)
3. Heat transfer by radiation from the solid surface
4. Viscous heat dissipation

Figure 2-1 shows an example of microscopic structure of porous media. Fluid is represented by blue color and solid by grey. Heat conduction occurs in the fluid, in the solid and at the interphase between fluid and solid (area A on Figure 2-1). Heat transfer by convection can be further subdivided into heat transfer by forced convection and by natural convection. Forced convection occurs where the fluid flows in porous media under external driving forces (area B on Figure 2-1), such as a pressure gradient. Natural convection occurs due to the buoyancy force which is caused by density differences in the fluid(s). Density difference in single fluid flow is caused by of non-uniform temperature distribution in the fluid and as a result of variable thermal expansion within the fluid. Heat radiation is the heat transfer phenomenon when heat is transferred from the surface of a body by emission of electromagnetic waves. Radiation becomes significant at high temperatures.

For the purposes of this thesis only heat conduction in porous media with a single stagnant fluid is considered. In the next section approaches and equations that describe heat conduction in porous media are discussed.
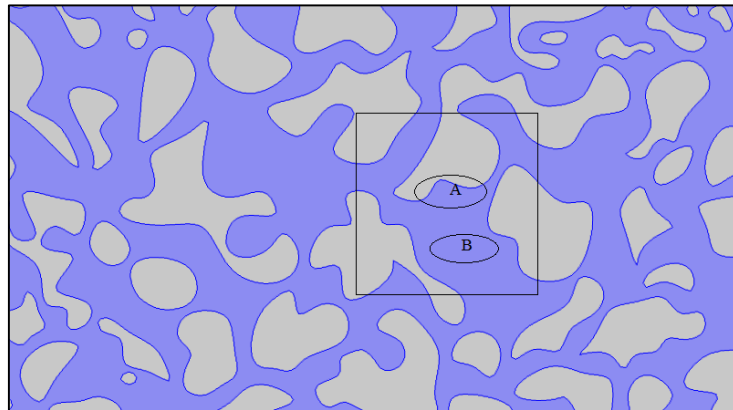
Figure 2-1 – Heat transport in porous media

2.1 Fourier's Law

Fourier's Law of heat conduction states that heat flux through a material is proportional to the temperature gradient. The general form of Fourier's Law for an anisotropic homogeneous medium is

$$\boldsymbol{q} = -\boldsymbol{k} \cdot \nabla T \qquad \text{2.1}$$

where

$\boldsymbol{q} = [q_x, q_y, q_z]'$ is a three-dimensional heat flux vector,

$$\boldsymbol{k} = \begin{bmatrix} k_{xx} & k_{xy} & k_{xz} \\ k_{yx} & k_{yy} & k_{yz} \\ k_{zx} & k_{zy} & k_{zz} \end{bmatrix} \text{ is a symmetric second order tensor called the thermal conductivity tensor,}$$

$\nabla T = \left[\frac{\partial T}{\partial x}, \frac{\partial T}{\partial y}, \frac{\partial T}{\partial z}\right]'$ is a three-dimensional temperature gradient vector,

$T = T(x, y, z)$ is a spatial distribution of temperature in a medium.

Using full notation the Fourier's Law can be rewritten as follows:

$$\begin{aligned}
q_x &= -\left(k_{xx}\frac{\partial T}{\partial x} + k_{xy}\frac{\partial T}{\partial y} + k_{xz}\frac{\partial T}{\partial z}\right) \\
q_y &= -\left(k_{yx}\frac{\partial T}{\partial x} + k_{yy}\frac{\partial T}{\partial y} + k_{yz}\frac{\partial T}{\partial z}\right) \qquad \text{2.2} \\
q_z &= -\left(k_{zx}\frac{\partial T}{\partial x} + k_{zy}\frac{\partial T}{\partial y} + k_{zz}\frac{\partial T}{\partial z}\right)
\end{aligned}$$

In a simple case when the one dimensional heat conduction in isotropic media is considered the Fourier's Law takes the following form:

$$q = -k\nabla T \qquad \text{2.3}$$

where

q is the heat flux in direction of heat flow,

k is the thermal conductivity of media,

∇T is the temperature gradient in the direction of heat flow.

The negative sign is because heat flux and temperature gradient has different directions. With respect to heat transfer "isotropic" means that thermal conductivity is the same in all directions, thus k is a scalar. Thermal conductivity of homogeneous material is a property of that material

and generally it depends on temperature and pressure. For materials such as rock minerals and liquid fluids, dependence on pressure can be neglected with good accuracy.

2.2 Transient heat conduction

The general form of the heat transfer shell balance equation for representative elementary volume is as follows (Bird, Stewart and Lightfoot 2007):

$$
\left\{ \begin{array}{c} rate\ of \\ energy\ in \\ by\ convective \\ transport \end{array} \right\} - \left\{ \begin{array}{c} rate\ of \\ energy\ out \\ by\ convective \\ transport \end{array} \right\} + \left\{ \begin{array}{c} rate\ of \\ energy\ in \\ by\ conduction \\ transport \end{array} \right\} - \left\{ \begin{array}{c} rate\ of \\ energy\ out \\ by\ conduction \\ transport \end{array} \right\} +
$$

$$
+ \left\{ \begin{array}{c} rate\ of \\ energy \\ production \end{array} \right\} = \left\{ \begin{array}{c} rate\ of \\ energy\ change \\ in\ the\ system \end{array} \right\}
$$

Using the general form of shell balance equation and considering heat conduction only with no convection and no heat generation one can write the following transient heat conduction equation:

$$
\left(\rho c_p \right) \frac{\partial T}{\partial t} = \nabla \cdot k \nabla T
$$

2.4

This equation describes time dependent temperature distribution profiles in media due to heat conduction. In order to solve the above equation appropriate boundary conditions are required.

2.3 Heat conduction in porous media

For heterogeneous media such as fully saturated porous media thermal conductivity depends on pore space structure and the thermal conductivity of constituents (rock, oil, water, gas).

Usually porous media are presented in terms of continuous media with effective properties. Given that the size of pores is much smaller than the size of whole system one can average the microscopic heterogeneous properties and derive equations in terms of effective (averaged properties). One of the well-known examples is Darcy's equation of flow. The same approach is applicable for heat transfer through porous media.

For each phase transient heat conduction equation can be written as

$$\left(\rho c_p\right)_s \frac{\partial T_s}{\partial t} = \nabla \cdot k_s \nabla T_s \tag{2.5}$$

$$\left(\rho c_p\right)_f \frac{\partial T_f}{\partial t} = \nabla \cdot k_f \nabla T_f \tag{2.6}$$

Boundary conditions on the interface between rock and fluid are continuity of temperature and heat flux:

$$T_s = T_f \tag{2.7}$$

$$n_{fs} \cdot k_f \nabla T_f = n_{fs} \cdot k_s \nabla T_s \tag{2.8}$$

Assuming local thermal equilibrium (negligible local temperature difference between the phases) and applying local volume averaging (Kaviany 1999) one can derive the following equation for porous media in terms of its effective properties:

$$\left(\rho c_p\right)_e \frac{\partial T}{\partial t} = \nabla \cdot (k_e \nabla T) \tag{2.9}$$

where

$\left(\rho c_p\right)_e$ is the effective volumetric heat capacity of porous media,

k_e is the effective thermal conductivity of porous media.

Effective volumetric heat capacity of porous media can be easily determined through the properties of constituents as follows:

$$\left(\rho c_p\right)_e = \phi\left(\rho c_p\right)_f + (1-\phi)\left(\rho c_p\right)_s \tag{2.10}$$

where

ϕ is the porosity of the medium (fraction of void space),

$(\rho c_p)_f$ is the volumetric specific heat capacity of the fluid,

$(\rho c_p)_s$ is the volumetric specific heat capacity of the solid.

As for the effective thermal conductivity of porous media there is no easy formula that can be derived as in case of effective volumetric heat capacity. The attempts to predict the effective thermal conductivity of porous materials are discussed in the next subsection.

In the assumption of steady state heat conduction equation 2.9 can be written as

$$\nabla \cdot (k_e \nabla T) = 0 \qquad\qquad \textbf{2.11}$$

Finally assuming the isotropic media we obtain the steady state heat transfer equation which describes temperature distribution in isotropic porous media:

$$\nabla^2 T = 0 \qquad\qquad \textbf{2.12}$$

2.4 Prediction of the effective thermal conductivity of porous media

In heat conduction in porous media the effective thermal conductivity is the main parameter that affects the temperature distribution profiles. There are two main approaches to determine effective thermal conductivity of a porous material:

1. Conduct experiments
2. Apply correlations

There are two types of porous materials: with internal porosity and with external porosity (Carson, et al. 2005). Porous media with internal porosity can be described as materials with interconnected solid matrix that contain pores/bubbles (i.e. sponge). Porous media with external porosity can be described as granular materials with fluid in-between (i.e. oil sands). In the first case the solid phase is continuous and the fluid phase can be either dispersed or continuous. In the second case the fluid phase is continuous and the solid phase can be either dispersed or continuous. Dispersed phase (as opposed to continuous) means that there is no continuous pathway from inlet to outlet.

There are many correlations available in the literature, which allow prediction of effective thermal conductivity of porous materials given other known properties. Effective thermal conductivity (k_e) depends on the following parameters:

- porosity (ϕ)
- thermal conductivity of fluid (k_f), thermal conductivity of solid (k_s)
- structure of pore space
- contact area between grains
- shape of grains
- grains size distribution

In terms of physics involved the effective thermal conductivity depends on:

- heat conduction
- heat convection
- heat radiation
- viscous heat dissipation

15

Correlations that allow prediction of one property of a mixture through properties of their constituents are usually called "mixing rules". Thermal conductivity mixing rules can be classified into the following categories (Tsotsas and Martin 1987):

- Type I – solution of Laplace equation either analytical or numerical.
- Type II – porous media are represented as a combination of thermal conductivities partially in parallel and partially in series.
- Type III – porous media are represented as a repeated unit cell for which exact or approximate solution is obtained.

The normalized effective thermal conductivities of the medium and the solid are defined as follows. Normalized thermal conductivity of solid and solid to fluid ratio will be used interchangeably throughout the text of the thesis.

$$K_e = \frac{k_e}{k_f} \qquad \text{2.13}$$

$$K_s = \frac{k_s}{k_f} \qquad \text{2.14}$$

It should also be mentioned that any mixing rule to be universal should satisfy the following limiting relations:

1. If $\phi \to 0$, then $k_e \to k_s$ ($K_e \to K_s$)
2. If $\phi \to 1$, then $k_e \to k_f$ ($K_e \to 1$)
3. If $k_s = k_f$ ($K_s = 1$), then $k_e = k_s = k_f$ ($K_e = 1$)
4. If $k_f \to \infty$
    a. then $k_e \to \infty$ if fluid is the continuous phase
    b. then k_e is finite if fluid is the dispersed phase
5. If $k_s \to \infty$
    a. then $k_e \to \infty$ if solid is the continuous phase
    b. then k_e is finite if solid is the dispersed phase
6. If $k_f \to 0$
    a. then $k_e \to 0$ if solid is the dispersed phase
    b. then k_e is finite if solid is the continuous phase
7. If $k_s \to 0$

16

a. then $k_e \to 0$ if fluid is the dispersed phase

b. then k_e is finite if fluid is the continuous phase

The first limiting relationship means that when the material porosity approaches zero, the overall effective thermal conductivity approaches the solid material thermal conductivity. The second limiting relationship means that when the porosity of material approaches one, the fluid fills more and more space and the effective thermal conductivity approaches that of the fluid. The third relationship shows that if the porous material components have the same thermal conductivity, then the composite material also has the same effective thermal conductivity (assuming there is no thermal resistance layer on the contact between the fluid and solid). Relations 4 and 5 are similar but apply to different phases (solid and fluid) and mean that when thermal conductivity of the continuous phase approaches infinity the overall effective thermal conductivity approaches infinity as well. In contrast when the thermal conductivity of the dispersed phase approaches infinity the overall effective thermal conductivity stays finite and depends on the thermal conductivity of the continuous phase. Relationships 6 and 7 are similar but also apply to different phases (fluid and solid) and mean that when the thermal conductivity of one phase approaches zero the overall effective thermal conductivity depends on the continuity of the other phase. The distinction between materials in terms of internal vs. external porosity can be made based on limiting relationships that apply to that material. For materials with internal porosity 4b, 5a, 6b, 7a apply, while for materials with external porosity 4a, 5b, 6, 7b apply.

There are a lot of mixing rules available in the literature. The most commonly used are discussed below. All the mixing rules were normalized by the fluid thermal conductivity.

Parallel model

The parallel model assumes fluid and solid are arranged in layers which are parallel to heat flow. This model predicts the maximum effective thermal conductivity. The model is presented in Figure 2-2. The parallel model fulfills limiting relations 1-3, 4a, 5a, 6b, 7b.

$$K_e = \phi + (1 - \phi)K_s \qquad\qquad\qquad \textbf{2.15}$$
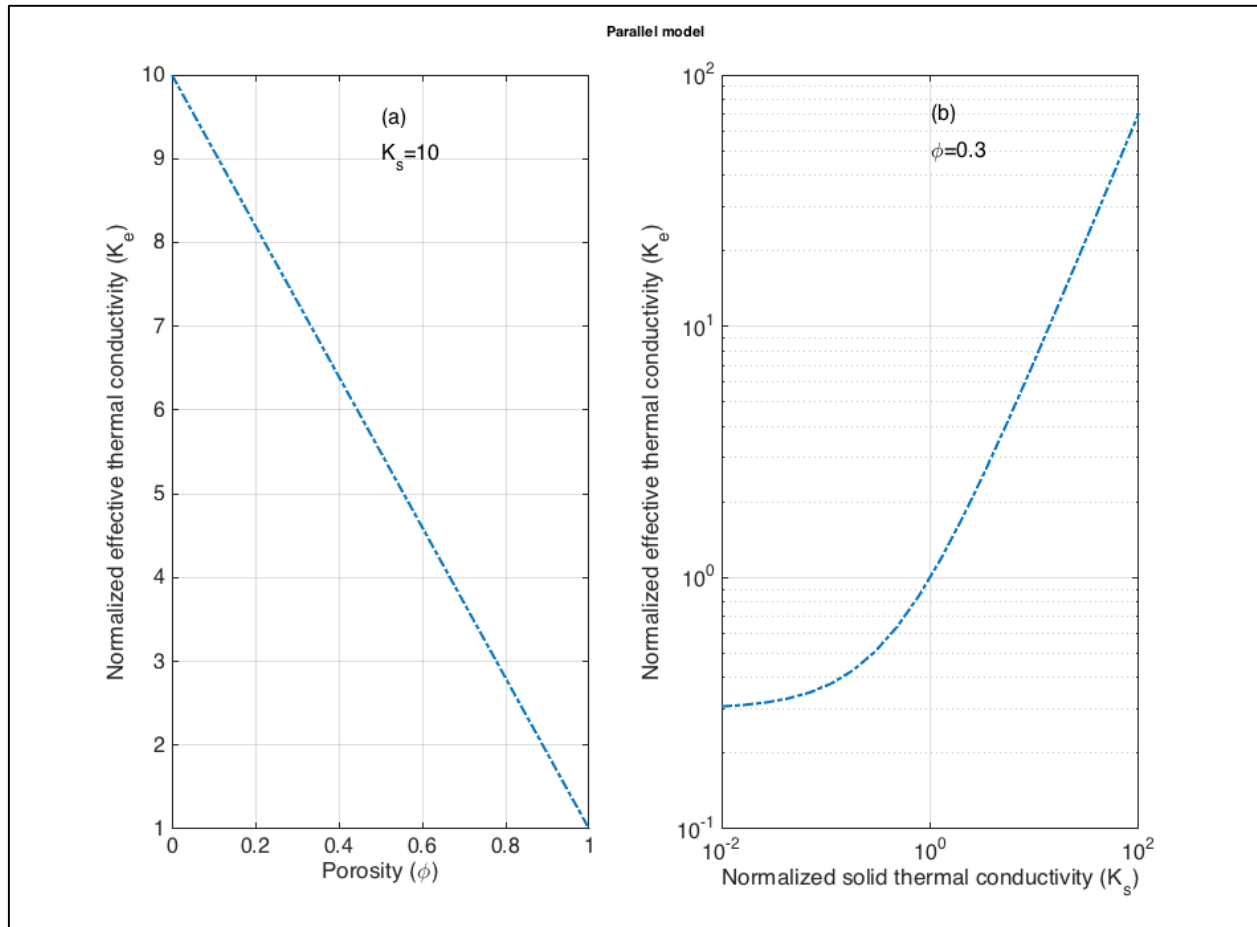
Figure 2-2 – Parallel model

Series model

The series model assumes the arrangement of fluid and solid in layers which are perpendicular to heat flow. This model predicts the minimum effective thermal conductivity. The model is presented in Figure 2-3. The series model fulfills limiting relations 1-3, 4b, 5b, 6a, 7a.

$$K_e = \frac{1}{\phi + \frac{1 - \phi}{K_s}}$$ **2.16**
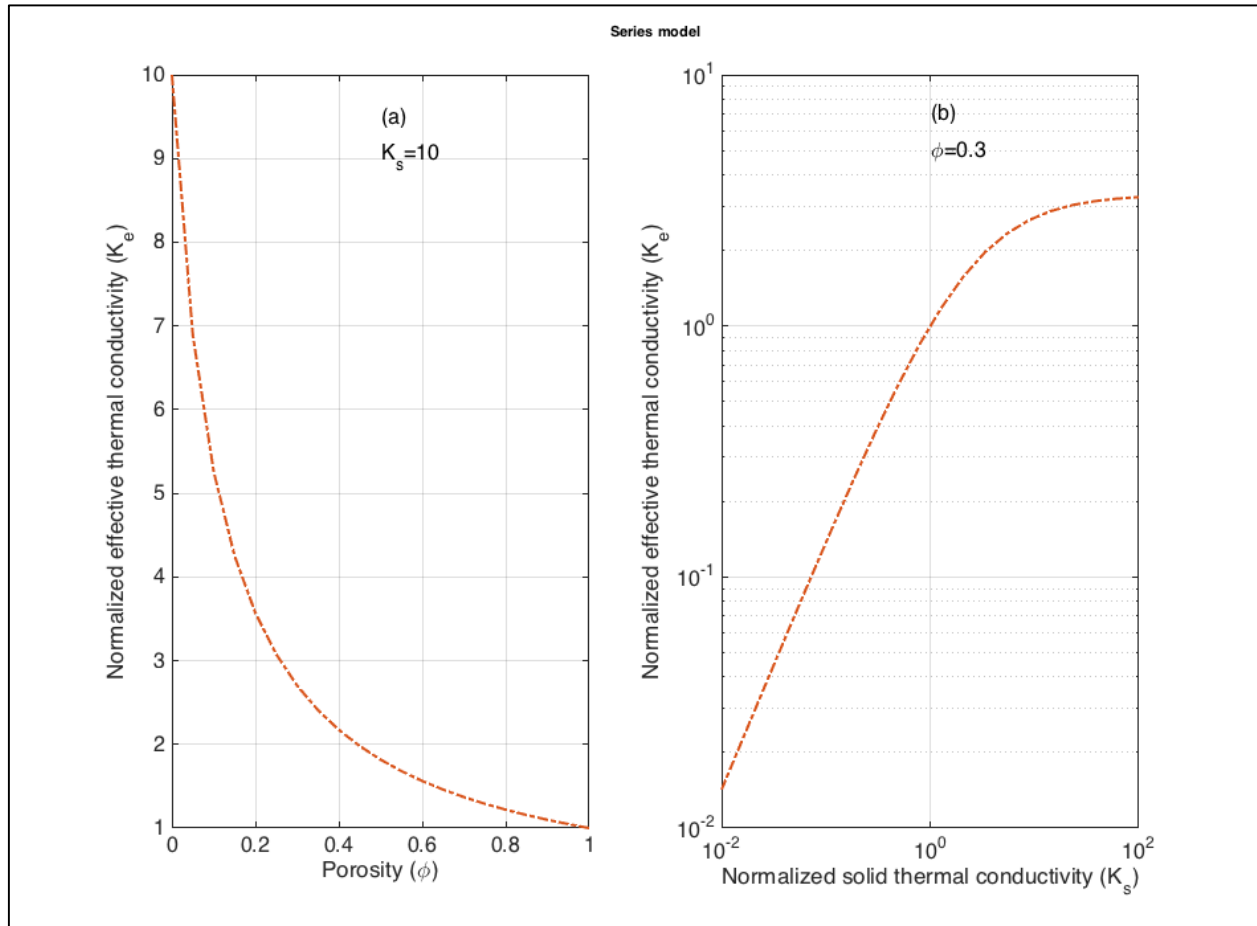
Figure 2-3 – Series model

19

Geometric mean model

The geometric mean model (Nield 1991) does not have any underlying structure of fluid and liquid, rather than common sense, as the weighted geometric mean lies between weighted harmonic mean (series model) and weighted arithmetic mean (parallel model). The model is presented in Figure 2-4. Geometric mean model fulfills limiting relations 1-3, 4a, 5a, 6a, 7a.

$$K_e = K_s^{1-\phi} \hspace{4cm} \textbf{2.17}$$
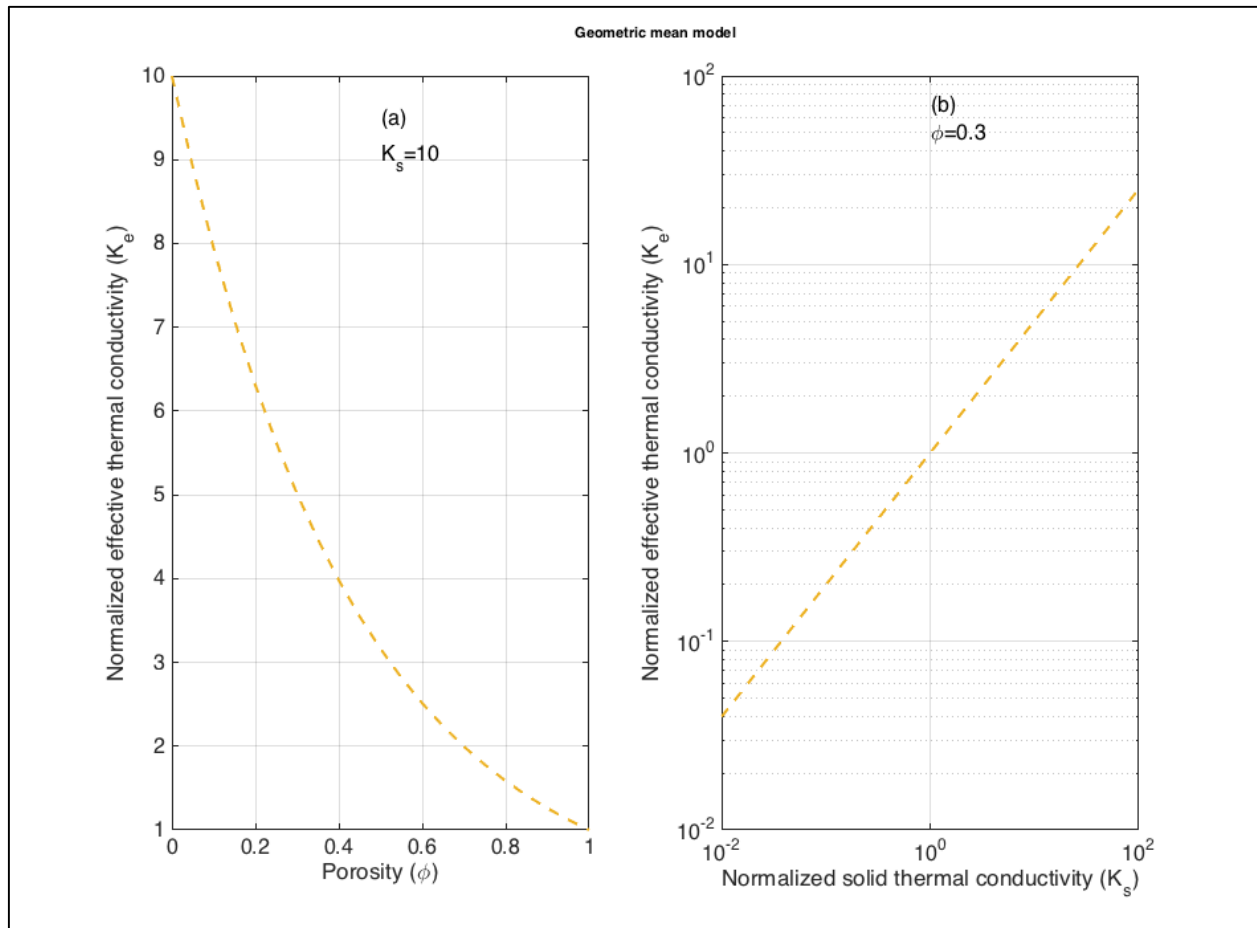
Figure 2-4 – Geometric mean model

Maxwell models

The model was originally developed by Maxwell (Maxwell 1873). It assumes that the dispersed phase is loosely packed so each grain does not affect the temperature profiles of the neighboring grains. Thus the Maxwell model is applicable to porous media with high porosity. This model is also known in the literature as the Hashin-Shtrinkman model (Hashin and Shtrikman 1962) which is mathematically equivalent to the Maxwell model, but was derived using a different approach. Eucken extended the Maxwell model to the case of multiple phases (Eucken 1932). In the case of $k_{cont} > k_{disp}$ equation 2.18 should be used and in the case of $k_{cont} < k_{disp}$ equation 2.19 should be used. Let us define these two cases as Maxwell-1 and Maxwell-2 models respectively. Both models are presented in Figure 2-5. The Maxwell-1 model fulfills limiting relations 1-3, 4a, 5b, 6a, 7b. The Maxwell-2 model fulfills limiting relations 1-3, 4b, 5a, 6b, 7a.

$$K_e = \frac{2 + K_s - 2(1 - K_s)(1 - \phi)}{2 + K_s + (1 - K_s)(1 - \phi)} \qquad \textbf{2.18}$$

$$K_e = \frac{2 + 1/K_s - 2(1 - 1/K_s)\phi}{2 + 1/K_s + (1 - 1/K_s)\phi} \qquad \textbf{2.19}$$
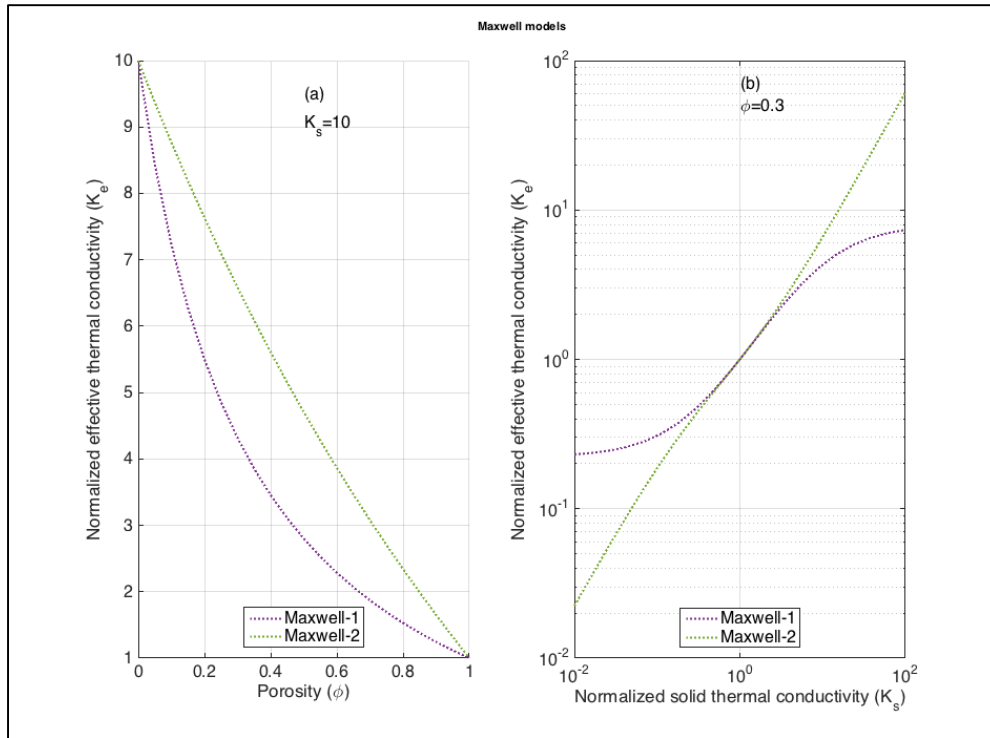
Figure 2-5 – Maxwell models

Kunii-Smith model

Kunii and Smith developed the following correlation assuming each phase acting separately and combined them as a combination of parallel and series models described above (Kunii and Smith 1960).

$$K_e = \phi + \frac{a_1(1-\phi)}{a_3 + \frac{a_2}{K_s}} \qquad \text{2.20}$$

$$a_1 = 1, \; a_2 = \frac{2}{3}, \; a_3 = \phi_2 + 4.63 \cdot (\phi - 0.26)(\phi_1 - \phi_2) \qquad \text{2.21}$$

$$\phi_{1,2} = \frac{0.5\left(\frac{K_s-1}{K_s}\right)^2 \sin^2\theta_0}{\ln(K_s - (K_s-1)\cos\theta_0) - \frac{K_s-1}{K_s}(1-\cos\theta_0)} - \frac{2}{3K_s}, \; \sin^2\theta_0 = \frac{1}{n} \qquad \text{2.22}$$

where $n = 1.5$ corresponds to ϕ_1 and $n = 4\sqrt{3}$ to ϕ_2. Kunii and Smith model is valid for the range of porosity from 0.26 to 0.476. It is recommended to use $a_3 = \phi_2$ for $\phi < 0.26$ and $a_3 = \phi_1$ for $\phi > 0.476$. The model is presented in Figure 2-6. The Kunii-Smith model fulfills the limiting relations 2, 3, 4a, 5a, 6a, 7b.
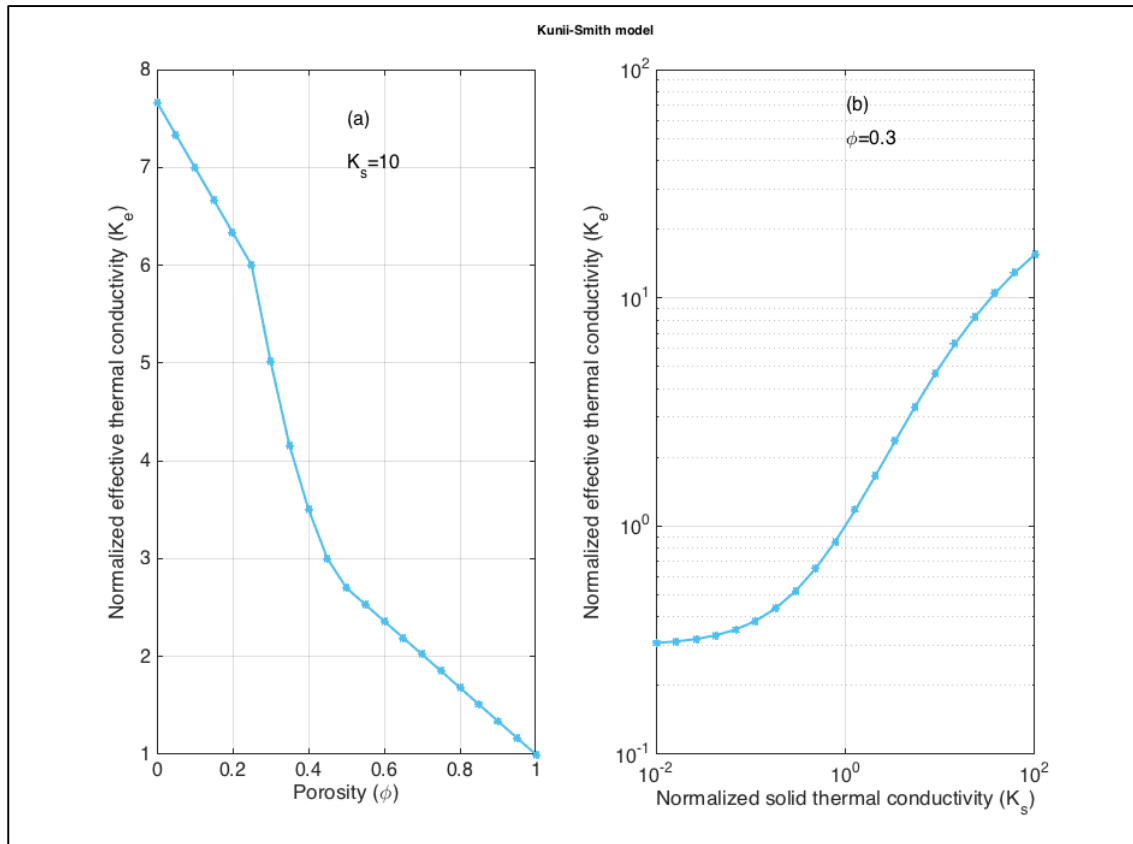
Figure 2-6 – Kunii-Smith model

Krupiczka model

The equations were derived for packings of long cylinders and cubic packings of spheres and then solutions were approximated by one correlation (Krupiczka 1967). The correlation is valid for the range of porosity from 0.215 to 0.476. The model is presented in Figure 2-7. Krupiczka model fulfills limiting relations 3, 4b, 5b, 6b, 7b.

$$K_e = K_s^{0.280-0.7571\cdot\log(\phi)-0.057\cdot\log(K_s)} \qquad\qquad \textbf{2.23}$$
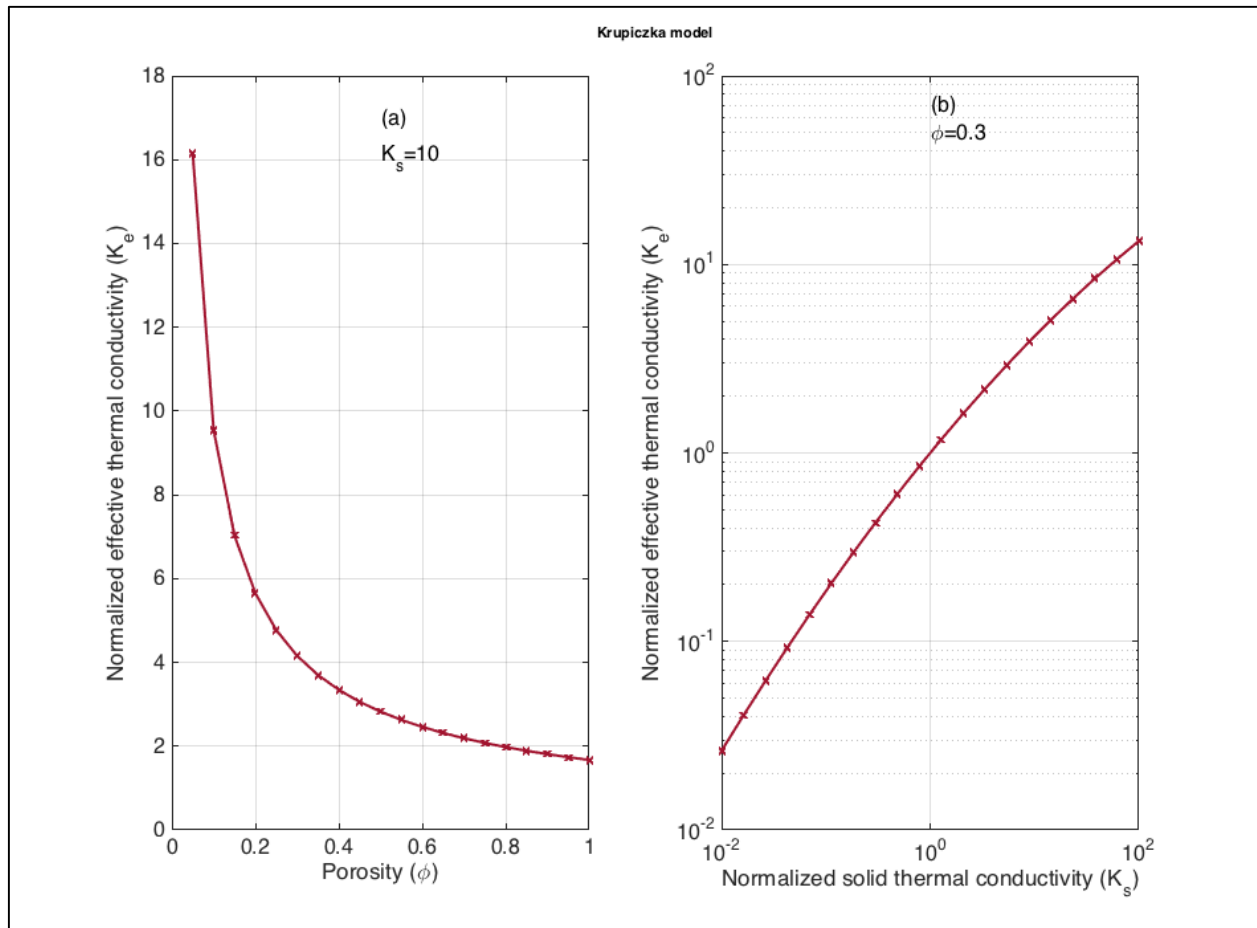
Figure 2-7 – Krupiczka model

Zehner-Schlunder model

Zehner and Schlunder assumed a unit cell of cylindrical shape with spherical particles inside (Zehner and Schlunder 1970). The heat transfer was considered through two parallel pathways: through the solid and fluid phase (near the center of cylinder) and through the fluid phase (near the edge of the cylinder). The model is presented in Figure 2-8. Zehner-Schlunder model fulfills limiting relations 1-3, 4a, 5a, 6a, 7b.

$$K_e = \left(1 - (1-\phi)^{0.5} + \frac{2(1-\phi)^{0.5}}{1-\frac{B}{K_s}} \left(\frac{\left(1-\frac{1}{K_s}\right)B}{\left(1-\frac{B}{K_s}\right)^2} \ln\left(\frac{K_s}{B}\right) - \frac{B+1}{2} - \frac{B-1}{1-\frac{B}{K_s}} \right) \right) \tag{2.24}$$

$$B = 1.25 \left(\frac{1-\phi}{\phi}\right)^{\frac{10}{9}} \tag{2.25}$$

Figure 2-8 – Zehner-Schlunder model

24
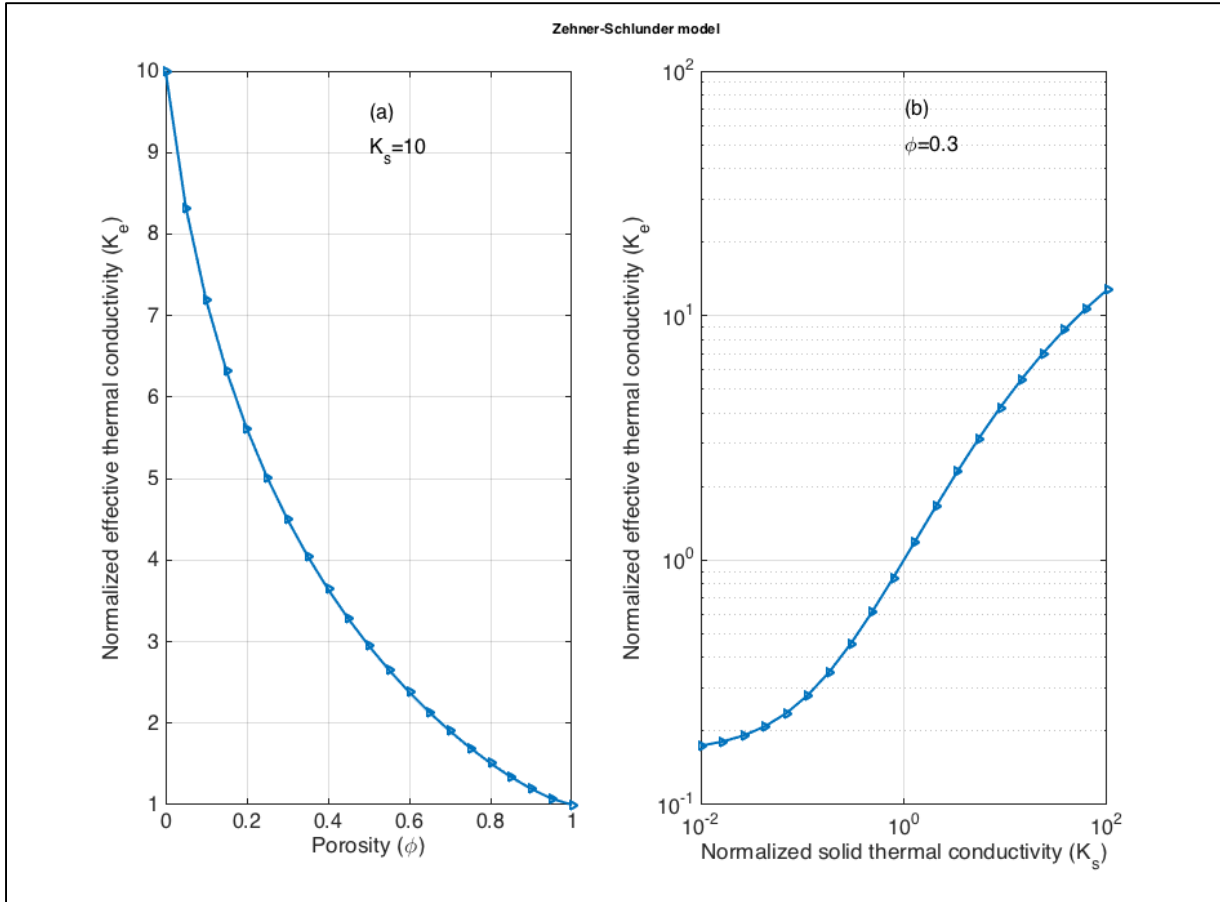
Woodside-Messmer model

Woodside and Messmer assumed an equivalent electrical resistivity model for conducting particles in a conducting electrolyte (Woodside and Messmer 1961). The equivalent model resulted in the following expression for the effective thermal conductivity:

$$K_e = \frac{aK_s}{K_s(1-d) + d} + c \qquad\qquad 2.26$$

$$c = \phi - 0.03, \; a = 1 - c, \; d = \frac{1-\phi}{a} \qquad\qquad 2.27$$

The model is presented in Figure 2-9. The Woodside-Messmer model fulfills limiting relations 2, 3, 4a, 5b, 6a, 7b.
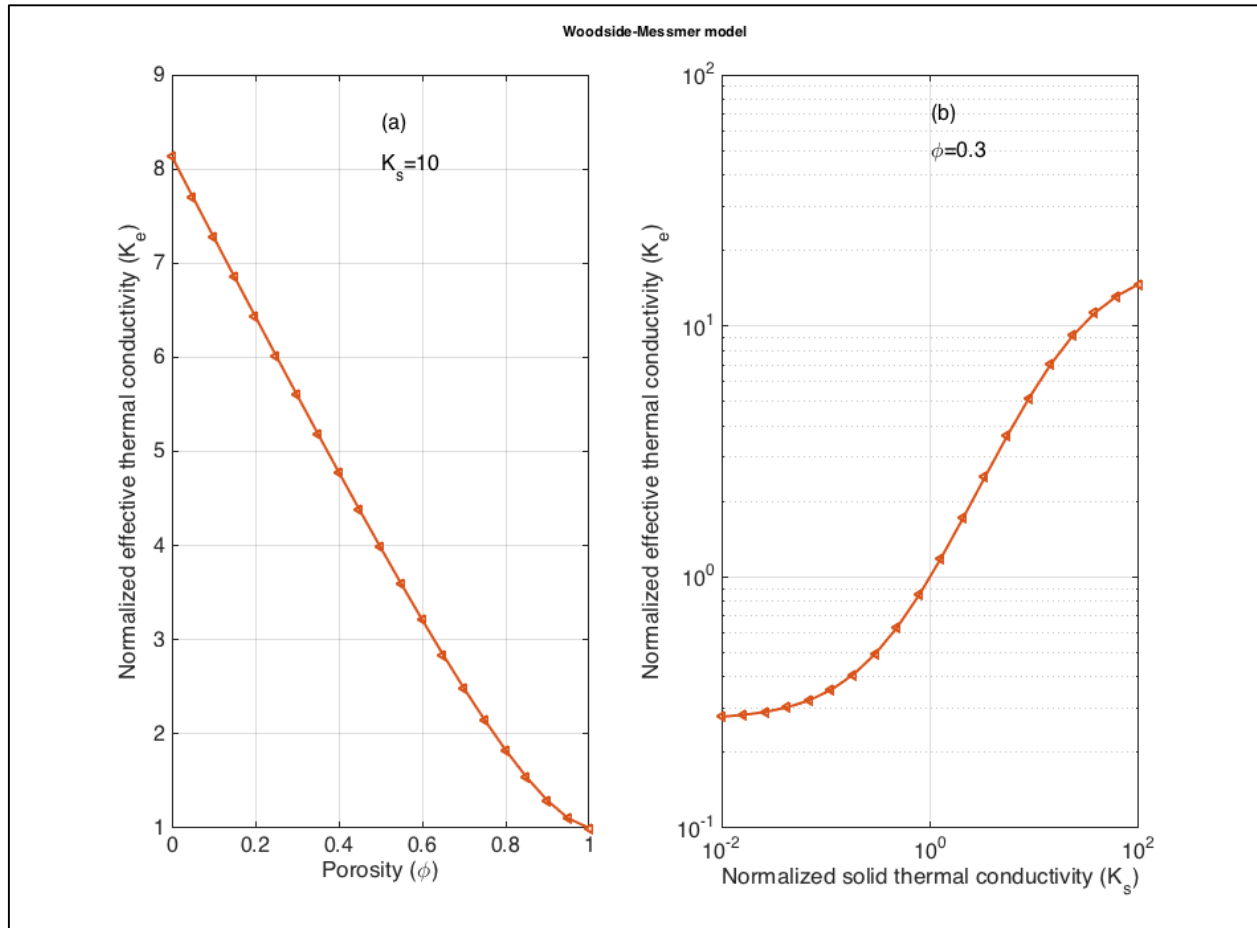
Figure 2-9 – Woodside-Messmer model

Effective Medium Theory model

Effective Medium Theory assumes random distribution of two phases within the whole volume. The model was developed for the case of electrical conductivity and is mentioned in Hashin and Shtrikman (Hashin and Shtrikman 1962), but also applies to thermal conductivity due to the similarity of the underlying equations. The model is presented in Figure 2-10. The Effective Medium Theory model fulfills the limiting relations 1, 2, 3, 4a, 5a, 6b, 7b.

$$(1 - \phi)\frac{K_s - K_e}{K_s + 2K_e} + \phi\frac{1 - K_e}{1 + 2K_e} = 0 \qquad \textbf{2.28}$$

$$K_e = \frac{1}{4}\left((3\phi - 1) + (3(1 - \phi) - 1)K_s + \sqrt{\left((3\phi - 1) + (3(1 - \phi) - 1)K_s\right)^2 + 8K_s} \right) \qquad \textbf{2.29}$$
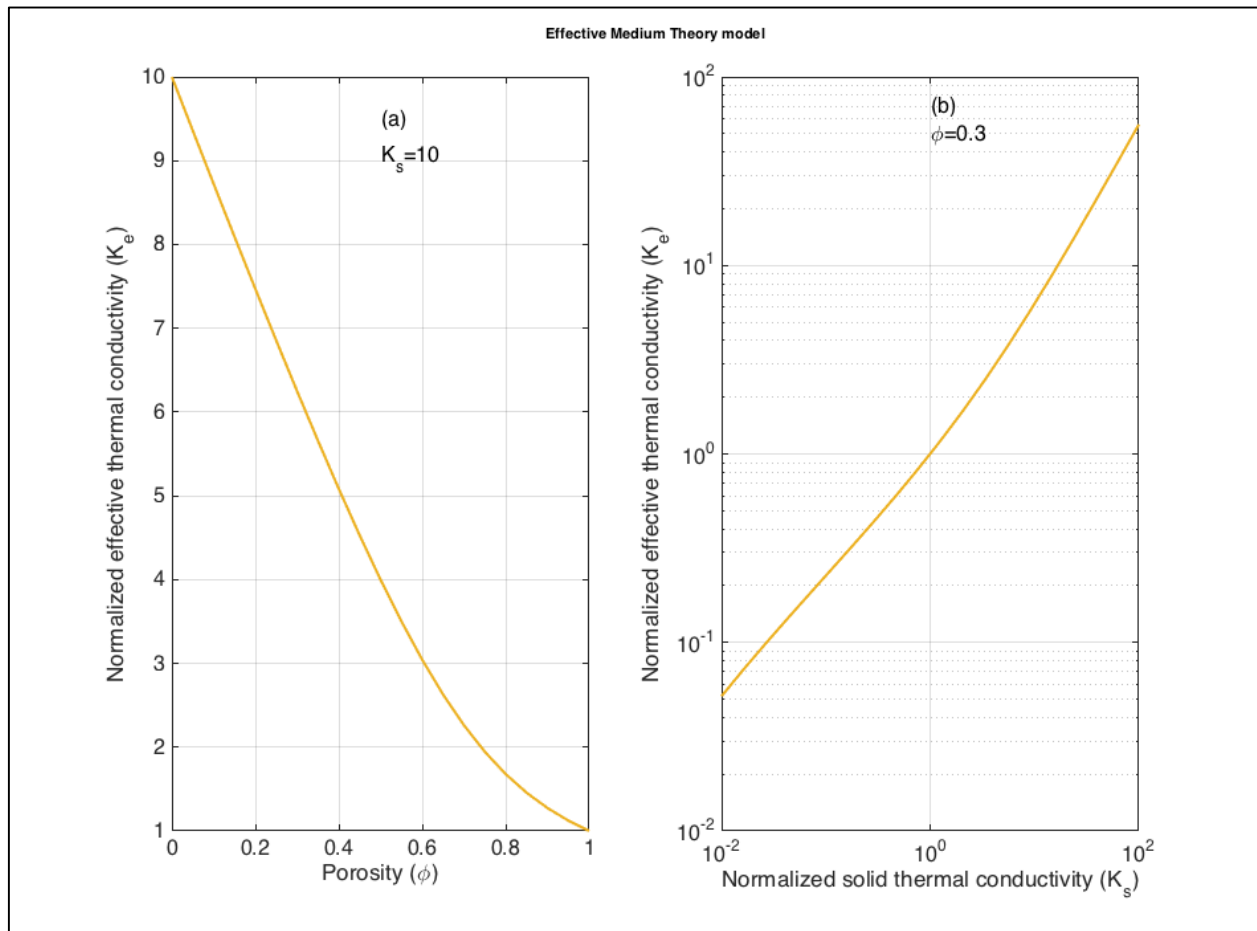
Figure 2-10 – Effective Medium Theory model

An extended literature review on the effective thermal conductivity models can be found in Tsostas and Martin (Tsotsas and Martin 1987). A very strong review of correlations related to different aspects of spherical packings (oscillatory porosity models, coordination number correlations, contact angles between adjacent particles and effective thermal conductivity) can be found in Van Antwerpen *et al.* (Van Antwerpen, Du Toit and Rousseau 2010).

There are two graphical ways to compare mixing rules: One way is to present them as a function of porosity for a fixed solid to fluid thermal conductivity ratio. The second way is to present them as a function of solid to fluid thermal conductivity ratio given a fixed porosity.

Figure 2-11 compares all of the above mixing rules using the first comparison approach, while Figure 2-12 depicts the second approach comparison. From Figure 2-11 one can conclude that the Krupiczka, Woodside-Messmer and Kunii-Smith models do not apply in the whole porosity range. The typical range of solid to fluid thermal conductivity ratio for the oil sands ranges from 1 to 100. From Figure 2-12 one can conclude that the values of the effective thermal conductivity of porous media predicted by different mixing rules in this region vary from one mixing rule to another. This in turn arises the question: which mixing rule to use? The detailed comparison of the described mixing rules is presented in Chapter 4 of the thesis.

The above presented models will be used for the purposes of this thesis, as they are the most cited and seem to provide fair results.
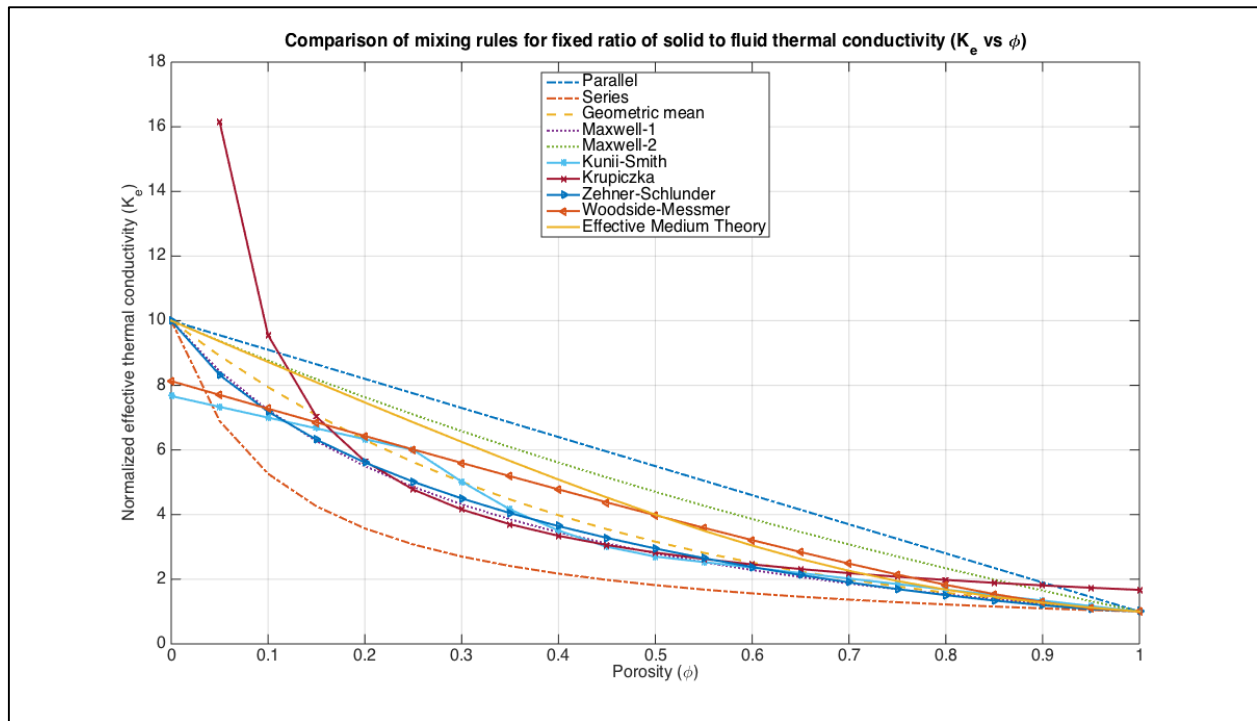
Figure 2-11 – Comparison of mixing rules for fixed K_s=10
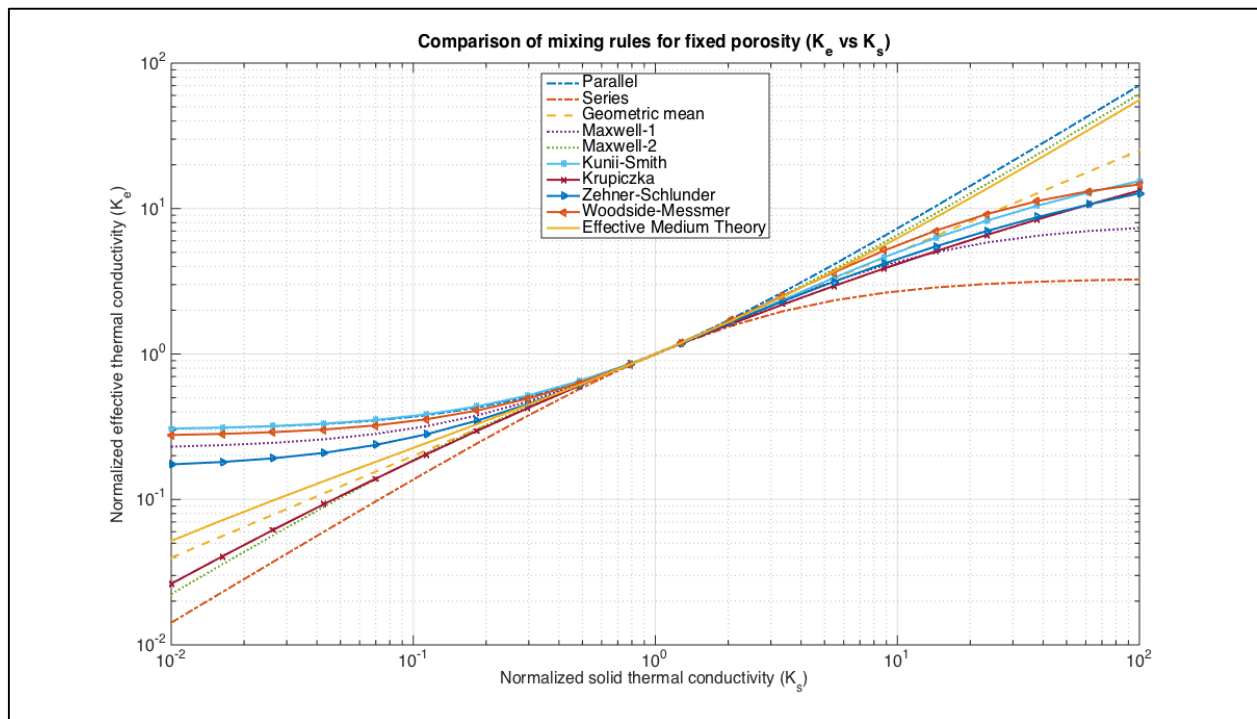
Figure 2-12 – Comparison of mixing rules for fixed ϕ=0.3

2.5 Measurement of thermal conductivity of porous media

There are many different experimental methods to determine the effective thermal conductivity of porous media. The methods can be classified in the following ways (Tsotsas and Martin 1987).

According to the equation to be solved:

- Steady-state. The experiment continues until the steady-state conditions are achieved along with specified boundary conditions (constant temperature or constant heat flux). Temperature is then measured at certain points of the test section and the thermal conductivity of unknown material is calculated from the solution of the steady-state heat conduction equation.

- Transient. The experiment starts with introducing a disturbance in temperature or heat flux and the response of the system is recorded. The response of the system is then fitted with a solution of the transient heat conduction equation in order to calculate the thermal conductivity of the unknown material.

According to the direction of the heat flux:

- Radial. In the radial systems heat propagates from the center of a cylindrical system towards the sides. In order to get the radial direction of heat flux, the heating rod is placed in the center of the cylindrical unknown material.

- Axial. In the axial systems heat propagates from one side of the sample to the other. In order to obtain the axial direction of heat flux the material is placed between a heater and a cooler.

According to the method:

- Absolute. In absolute methods the effective thermal conductivity of unknown material is calculated directly from the measured data.

- Comparative. In comparative methods a material with known thermal conductivity is used. The effective thermal conductivity of the unknown material is calculated from the ratio of thermal conductivities (unknown to know material).

With the development of numerical computational fluid dynamics (CFD) software another class of experimental methods was introduced (Arthur, et al. 2015). The exact geometry of the measurement system is provided into CFD software as input along with the properties of all

materials used in the system. All the significant physical processes should be introduced into the model (heat conduction through materials, heat convection of fluids, heat radiation if applicable, cooling of the system by natural convection of air, thermal resistance layers in-between the contacts of materials, etc.). The introduced physics require some parameters that are not known and should be estimated. For this purpose known materials are used in order to calibrate the system and determine any unknown parameters. After the system is calibrated the unknown material sample is placed in the test section and the temperature distribution profiles are recorded. The final step is to match the obtained temperature profiles by solving the optimization problem with the tested material thermal conductivity as the unknown parameter.

Several experimental data sources will be used for the purposes of this thesis. These data sources are the most commonly applied in the verification of the validity of the effective thermal conductivity mixing rules.

The first data is from Prasad *et al.* (Prasad, et al. 1989) and is presented in Table 2-1. The experimental approach used is of the steady-state type with axial heat flux and direct method of calculating the effective thermal conductivity of the porous material. The porous medium is represented by solid beads of spherical shape filled with fluid. Different combinations of fluid (water and glycol) and solid (glass, steel, and acrylic) were used. Table 2-1 contains the following columns: Liquid – type of fluid used, Solid – type of solid particles used, D_p – mean diameter of solid beads (mm), ϕ – porosity of the fluid-solid system, k_s – thermal conductivity of solid beads, $\frac{k_s}{k_f}$ – solid to fluid thermal conductivity ratio, k_e – effective thermal conductivity of the fluid-solid system.

Liquid	Solid	D_p	ϕ	k_s	$\dfrac{k_f}{k_s}$	k_e
-	-	mm	$\dfrac{m^3}{m^3}$	$\dfrac{W}{m \cdot K}$	$\dfrac{W}{m \cdot K}\Big/\dfrac{W}{m \cdot K}$	$\dfrac{W}{m \cdot K}$
Water	Glass	3.00	0.396	1.10	0.560	0.837
Water	Glass	25.4	0.425	1.10	0.562	0.842
Glycol	Glass	6.00	0.349	1.10	0.235	0.559
Glycol	Glass	25.4	0.427	1.10	0.235	0.597
Glycol	Steel	15.88	0.416	37.39	0.007	2.584
Glycol	Acrylic	12.77	0.402	0.16	1.630	0.221
Water	Acrylic	25.4	0.427	0.16	3.937	0.479

Table 2-1 – Experimental data from Prasad *et al.* (Prasad, et al. 1989)

The second data is from Nozad *et al.* (Nozad, Carbonell and Whitaker 1985) and is presented in Table 2-2. The experimental approach used is of transient type with axial heat flux and direct method of calculating the effective thermal conductivity of the porous material. Solid particles of spherical shape filled with fluid were used in the experiment. The higher fluid to solid thermal conductivity ratio was achieved by using urea, steel, bronze and aluminum as solid and water, glycerol and air as fluid. Table 2-2 contains the following columns: Liquid – type of fluid used, Solid – type of solid particles used, D_p – mean diameter of solid particles (mm), k_f – thermal conductivity of fluid ($\frac{W}{m \cdot K}$), k_s – thermal conductivity of solid ($\frac{W}{m \cdot K}$), $\frac{k_f}{k_s}$ – fluid to solid thermal conductivity ratio, ϕ – porosity of the fluid-solid system, $\frac{k_e}{k_f}$ – effective thermal conductivity of the fluid-solid system normalized by thermal conductivity of fluid.

Liquid	Solid	D_p	k_f	k_s	$\dfrac{k_s}{k_f}$	ϕ	$\dfrac{k_e}{k_f}$
-	-	mm	$\dfrac{W}{m \cdot K}$	$\dfrac{W}{m \cdot K}$	$\dfrac{W}{m \cdot K}\Big/\dfrac{W}{m \cdot K}$	$\dfrac{m^3}{m^3}$	$\dfrac{W}{m \cdot K}\Big/\dfrac{W}{m \cdot K}$
Water	Urea	2.5	0.623	0.744	1.23	0.41	1.2
Water	Steel	3.95	0.623	21.6	35.7	0.39	5.5
Water	Bronze	3.95	0.623	117	193	0.4	7.4
Glycerol	Bronze	3.95	0.294	117	397	0.39	10.4
Glycerol	Aluminum	3.95	0.294	218	740	0.4	12.4
Air	Bronze	3.95	0.0268	117	4336	0.39	45.7
Air	Aluminum	3.95	0.0268	218	8077	0.41	145
Air	Aluminum	3.95	0.0268	218	8077	0.4	136
Air	Aluminum	3.95	0.0268	218	8077	0.4	129

Table 2-2 – Experimental data from Nozad *et al.* (Nozad, Carbonell and Whitaker 1985)

Chapter 3: **Pore scale modeling**

A typical modeling project consists of several stages:

- Generation of geometry
- Application of physics and boundary conditions
- Solving the problem
- Calculating the properties of interest

For the purposes of heat transfer modeling at the pore scale level in this thesis, two phases are considered: a single fluid phase and a single solid phase. The solid phase is represented by touching spheres of different radii. The fluid phase fills the void space in-between the solid particles. The fluid is assumed to be stagnant (not moving). Thermal expansion of both phases is neglected. The contact between the solid grains is assumed to be ideal (no thermal resistive layer exists between the grains). Continuity of temperature and heat flux are assumed at the interface. Each phase is assumed to be isotropic in terms of heat transfer. Constant (but different) temperatures are specified as boundary conditions at the opposite sides of the porous media sample. The rest of the boundaries of the sample are assumed to be insulated (zero heat flux).

The software used for the pore scale modeling is as follows:

- Simpleware ScanIP Software
- COMSOL Multiphysics
- Matlab

Simpleware ScanIP is a software package which allows to reconstruct a three-dimensional geometry from a given stack of computer tomography (CT) images (slices). The main feature of the Simpleware ScanIP is that it is able to create a mesh for a reconstructed geometry and export it in a COMSOL compatible format. COMSOL was used to apply physics, material properties and boundary conditions, to solve the numerical problem and calculate the final results. COMSOL solves equations by means of finite elements method. This method requires appropriate meshing of geometry. Matlab was used to automate the entire process: from creating the geometry and meshing it with Simpleware ScanIP to creating COMSOL file, solving the problem and extracting the final results.

The following sections describe the process of virtual porous media generation, equations and boundary conditions used, along with the numerical experiments and results.

3.1 Virtual porous media generation

There are many different way to generate virtual porous media. For the purposes of this thesis two of them are used: pattern generation and CT image reconstruction.

Pattern generation

In the pattern generation approach, a box of a given size is filled with spheres of radii from a specific particle size distribution. The spheres are assumed to be rigid. There are two different modifications of this approach: recursively add spheres one by one or generate them simultaneously. The second modification is used in this thesis. The term particle swelling is used for this approach.

Particle size distribution data acts as input into the particle swelling algorithm. Examples of real particle size distributions of oil sands samples are presented in Figure 3-1. Particle size usually means the diameter of a particle and is measured in millimetres or phi units. Conversion from phi units to millimeters happens according to the following formula:

$$phi = -\log_2 d \qquad\qquad\qquad\textbf{3.1}$$
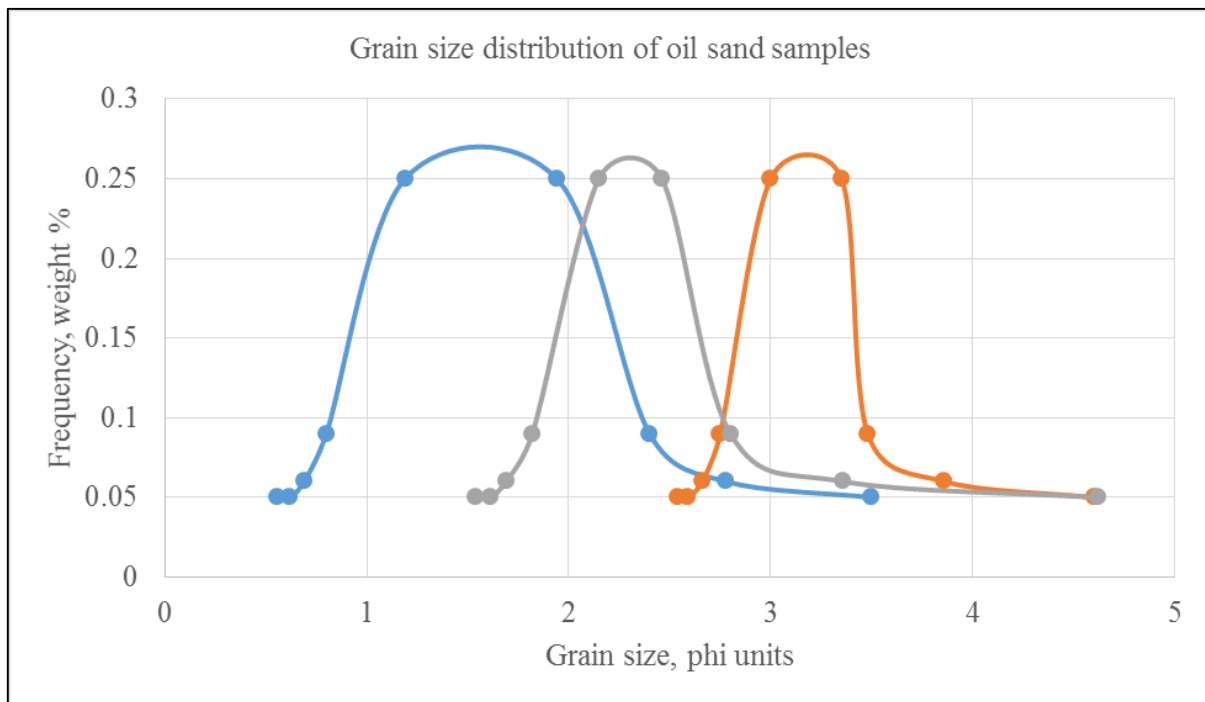
Figure 3-1 – Example of particle size distribution of oil sands samples (courtesy of PERM Inc.)

The particle swelling algorithm consists of the following steps:

1. Specify number of grains and target porosity of the media.

2. Estimate the size of the box.

3. Generate radii of the spheres from a given particle size distribution.

4. Randomly distribute starting points inside the box and assign growth (swelling) rate to each point according to its final radius.

5. Iteratively increase the radius of the spheres from point to final radius according to specified growth rate. With each iteration any overlapping conflicts are resolved by a slight change in position of the center of the overlapping spheres.

6. The algorithm continues until the target porosity is reached or no conflicts can be resolved.

A porous medium pattern is the output of the algorithm. The pattern is a set of spheres packed in a box. A two-dimensional pattern example is presented in Figure 3-2 and a three-dimensional pattern example is presented in Figure 3-3.
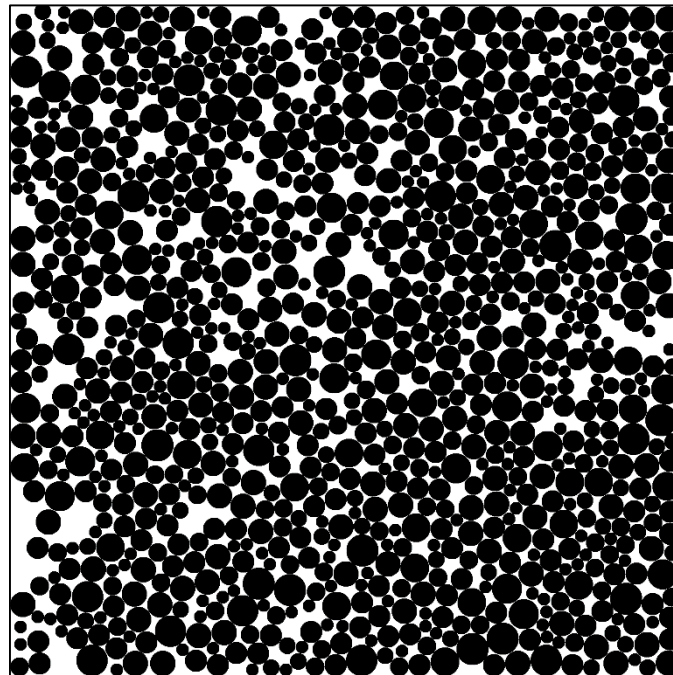
Figure 3-2 – Two dimensional pattern
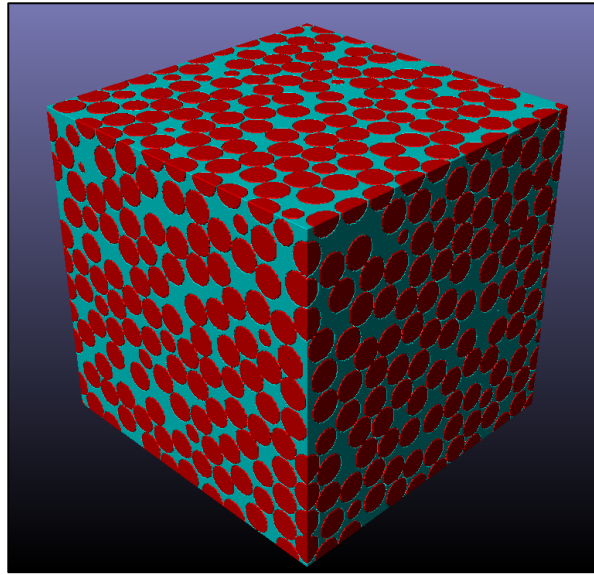
Figure 3-3 – Three dimensional pattern

The generated pattern is a list of geometrical objects with known coordinates of centres and sizes. It is not a final geometry that can be used for modeling. In order to get the final geometry it needs to be meshed. There are two available methods to mesh the generated pattern within the team: COMSOL and Simpleware.

The COMSOL approach requires creation of CAD geometry native to COMSOL. A typical pattern has around 2500 spheres. Taking this into consideration, the process of creating the native COMSOL geometry was automated by means of Matlab. The created COMSOL geometry is then meshed by COMSOL algorithms. The created mesh is of a good quality and is optimized for heat transfer physics. The workflow for this approach is presented in Figure 3-4.
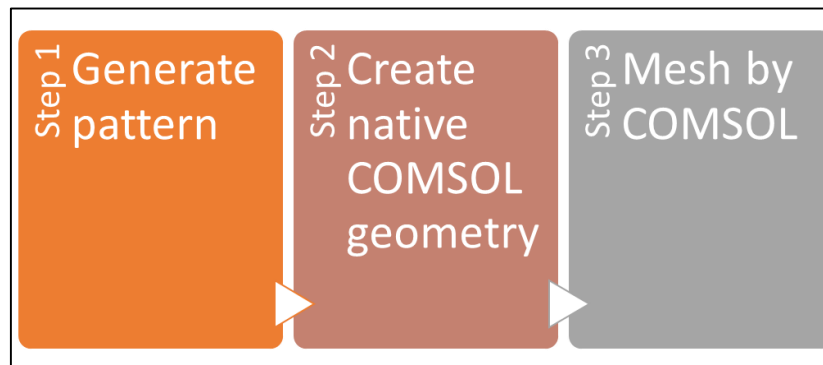
Figure 3-4 – Geometry based meshing workflow

The Simpleware approach requires that geometry is pixelized and converted into a stack of computer tomography images. The stack of images is then fed as input into Simpleware ScanIP software and a three-dimensional voxel-based geometry is reconstructed. A voxel is a three dimensional pixel. The reconstructed geometry is then meshed by Simpleware algorithms and exported in COMSOL-compatible format. The workflow for this approach is presented in Figure 3-5.
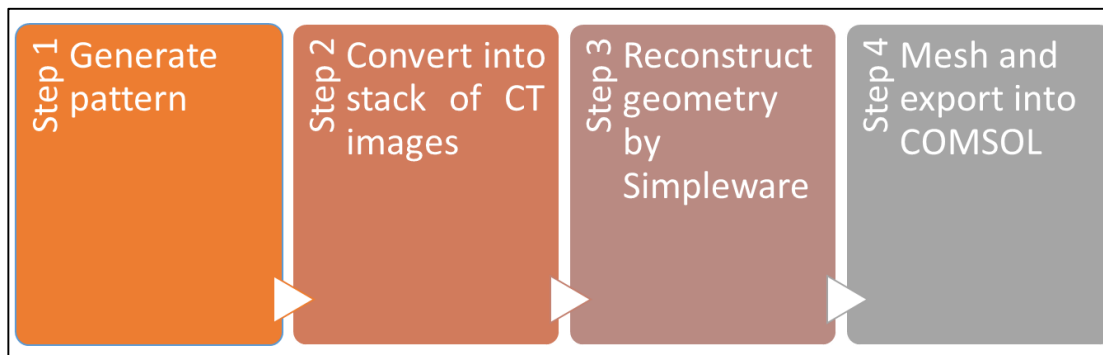
Figure 3-5 – Voxel based meshing workflow

The main difference between two approaches is that in the first case the exact geometry is used for mesh creation, while in the second case the pixelized geometry is used. The terms geometry-based mesh and voxel-based mesh will also be used to distinguish the two approaches throughout the text. Both meshing approaches were used and compared in this thesis.

Computer Tomography Image Reconstruction

In computer tomography (CT) image reconstruction method the sequence (stack) of CT images is used as input. A stack of CT images represents subsequent slices of the real object. A computer tomography scanner is used to obtain the stack of CT images, but it can be created artificially by pixelizing a known geometry. Each image consists of pixels with different greyscale values. The greyscale value of a pixel depends on the density of the underlying material. An example of a single CT image along with the stack is presented in Figure 3-6.
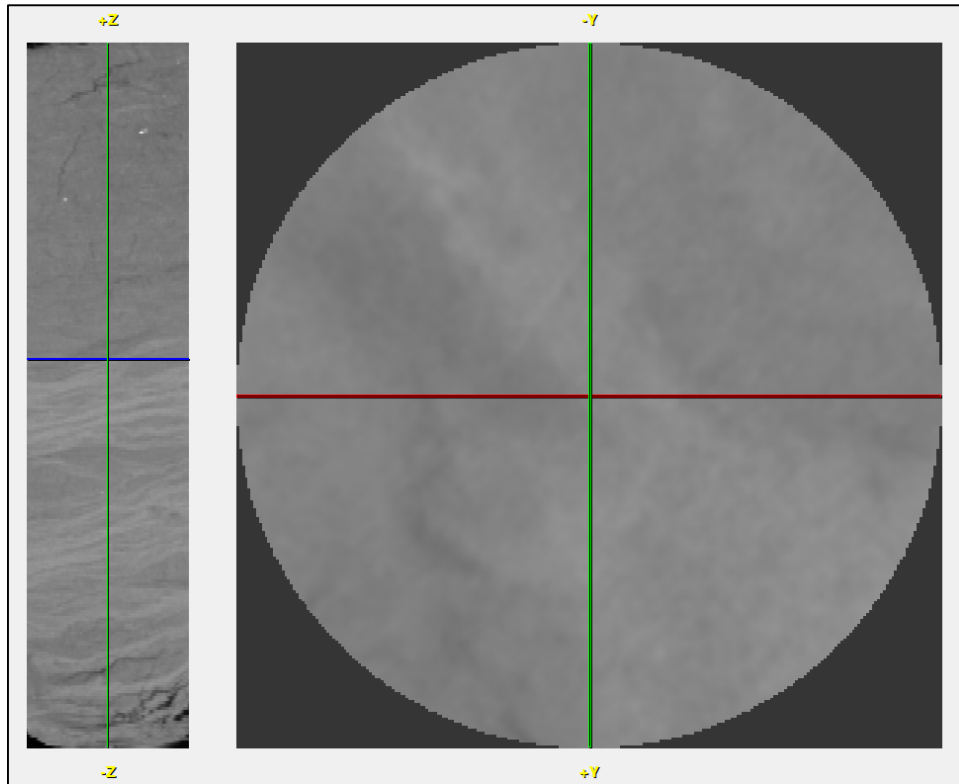
Figure 3-6 – Example of a CT image

A special image reconstruction software is used to create a three dimensional representation of geometry from a stack of CT images. Simpleware ScanIP software was used for the purposes of this thesis. The sequence of steps required to reconstruct the three dimensional geometry is as follows:

1. Create or obtain a stack of CT images.

2. Feed the stack into Simpleware.

3. Apply smoothing filters to reduce noise.

4. Create masks by thresholding different greyscale levels. Each mask represents a different material (i.e. solid or fluid).

5. Reconstruct geometry by applying meshing algorithms.

The CT image reconstruction algorithm can create two scales of geometries: the pore scale level and the core scale level. The pore scale level geometry means that one phase can be clearly separated from the other (i.e. solid from fluid). In the core level scale there is no way to distinguish different phases, only macro scale materials with effective properties. But it is

38

possible to separate different domains (effective materials with different properties) based on density.

In order to generate a pore scale level geometry one can use a cylindrical cell of glass beads saturated with water. This cell can be scanned using CT scanner and a stack of CT images can be obtained. Example of such a CT image is shown on Figure 3-7. The three dimensional geometry is then reconstructed with the workflow described above. Simpleware allows to rescale the geometry, so even if the size of glass beads is in order of centimeters, the scaled geometry can have the size in order of millimeters, micrometers or even nanometers. An example of pore scale level geometry generated by CT image reconstruction approach is presented in Figure 3-8.
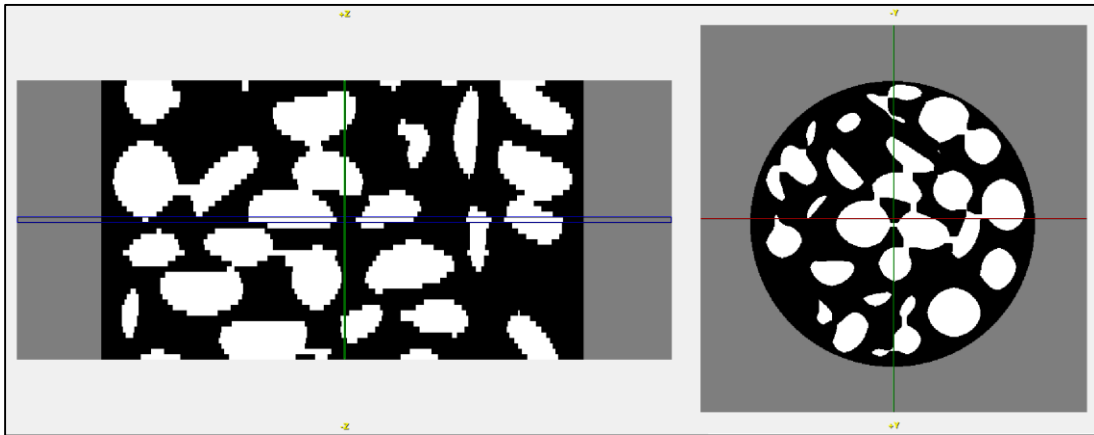
Figure 3-7 – Pore scale level CT image
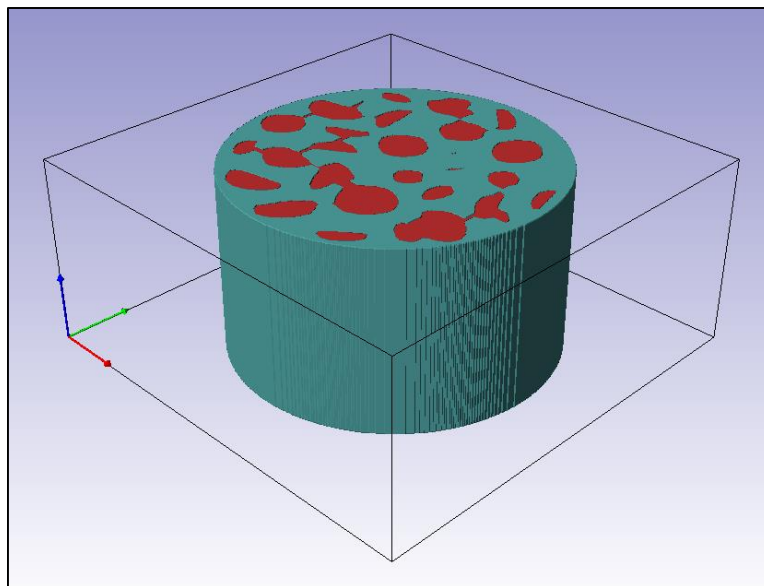
Figure 3-8 – Pore scale level reconstructed geometry

In order to generate a core scale level geometry one can scan a real core sample of cylindrical shape. The obtained stack of CT images contains information about different domains (as opposed to phases). An example of such an image is shown in Figure 3-6. The above described approach is applied in this case as well. The only difference is that domains are masked instead of phases. An example of core scale level geometry is presented in Figure 3-9.
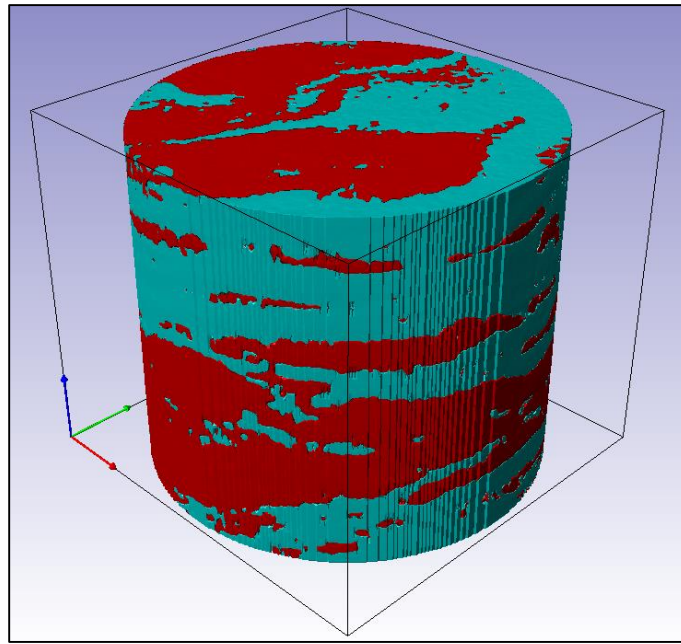
Figure 3-9 – Core scale level reconstructed geometry

3.2 Pore scale level physical model

To calculate effective thermal conductivity of virtual porous media the following governing equations are to be solved. The assumptions for the model are presented at the beginning of this chapter. The schematic of the model is presented on Figure 3-10.
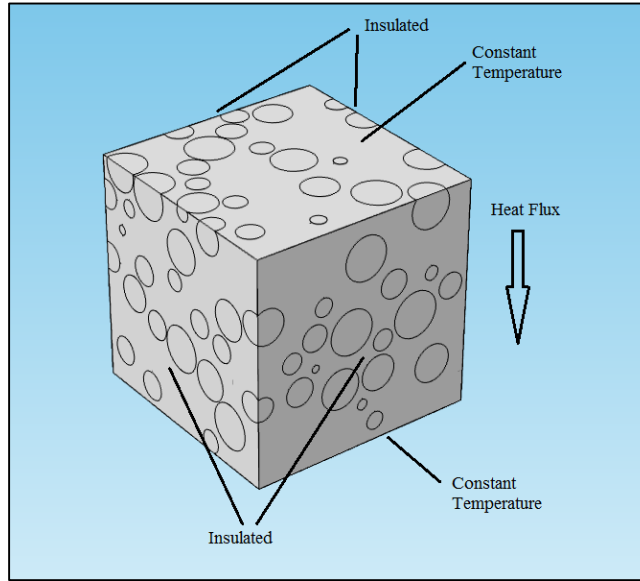
Figure 3-10 – Pore scale level model

Taking the model assumptions into consideration, the following set of equations along with boundary conditions defines the pore scale level heat transfer model:

$$\nabla \cdot (k\nabla T) = 0 \qquad \textbf{3.2}$$

$$\nabla T = 0, at\ x = x_1, x = x_2, y = y_1, y = y_2 \qquad \textbf{3.3}$$
$$T = T_1, at\ z = z_1$$
$$T = T_2, at\ z = z_2$$

Boundary conditions means that two sides of the cube are held at constant but different temperatures while all other sides are insulated. One should note that thermal conductivity k is not constant and depends on the position in the geometry (fluid or solid phase). Thermal conductivity map for the above geometry is presented in Figure 3-11. In this particular example grains have the thermal conductivity of sandstone ($6W/(m \cdot K)$) and fluid has the thermal conductivity of water ($0.6W/(m \cdot K)$).

41
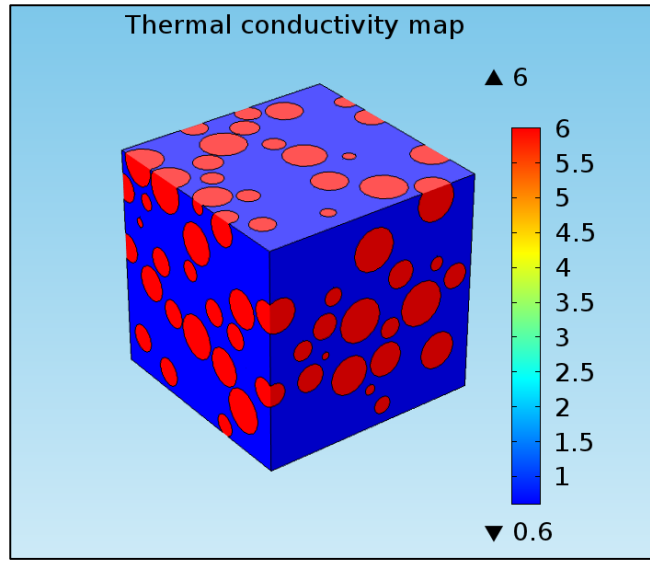
Figure 3-11 – Thermal conductivity map

A finite element method was used to solve Equation 3.2 using boundary conditions of Equation 3.3. The original geometry has to be meshed and the governing equation has to be linearized over the meshed geometry. The meshed geometry is presented in Figure 3-12.
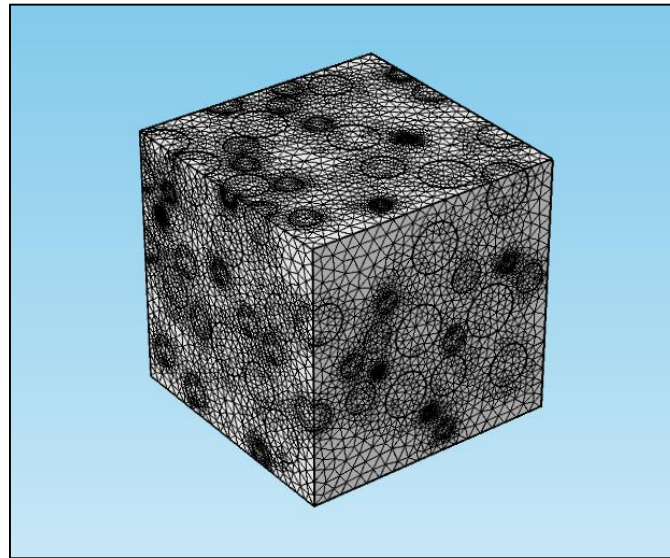
Figure 3-12 – Meshed geometry

The unknown variable of Equation 3.2 is temperature, which means that temperature distribution profile is the solution to this equation. The pore scale level temperature distribution profile for the above geometry is presented in Figure 3-13.
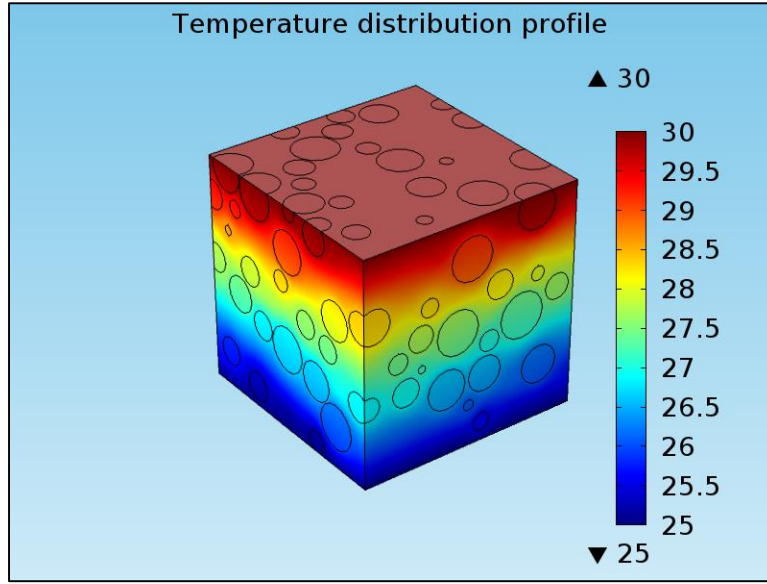
Figure 3-13 – Temperature distribution profile

Given the steady-state temperature distribution profile one can calculate the heat flux using the Fourier's Law:

$$q = -k\nabla T \qquad\qquad \textbf{3.4}$$

The average heat flux over the constant temperature boundary can be calculated as the average value of the function in Equation 3.4 over the surface:

$$q_{ave} = \frac{\int_S q\,ds}{\int_S ds} \qquad\qquad \textbf{3.5}$$

Porosity of the system can be calculated as:

$$\phi = \frac{\int_{V_L} dv}{\int_V dv} \qquad\qquad \textbf{3.6}$$

The effective thermal conductivity of the porous medium can be calculated using the following equation:

$$k_e = \frac{q_{ave}}{|z_2 - z_1||T_2 - T_1|} \qquad\qquad \textbf{3.7}$$

3.3 Numerical experiments

A set of numerical experiments was conducted in order to validate the appropriateness of the model described above. Four numerical experiments were conducted in order to analyze the model described above. The numerical experiments are described separately in corresponding subsections where results are also presented. A composite discussion of all numerical experiment results is presented in the next section for consistency.

Numerical experiment #01 – Validation by real experimental data

Experimental data from two sources were used for validation of the pore level heat transfer model. Experiments from Nozad, *et al.* (Nozad, Carbonell and Whitaker 1985) were numbered as N01 to N09 and from Prasad, *et al.* (Prasad, *et al.* 1989) as P01 to P07 as they appear in Table 2-2 and Table 2-1. Both experimental sources contain all the required information to set up the numerical models. Namely, they contain the mean size of beads used in the experiments, the solid bead material of the saturating fluid used, along with the thermal conductivity for constituents. Porosity was also measured in the experiments and it was used in the numerical experiments as a target porosity for the generated virtual porous patterns. The results of the numerical experiment are presented in Table 3-1.

Test ID	Liquid TC $\dfrac{W}{m \cdot K}$	Solid TC $\dfrac{W}{m \cdot K}$	Measured porosity	Numerical porosity	Measured ETC $\dfrac{W}{m \cdot K}$	Numerical ETC $\dfrac{W}{m \cdot K}$
P01	0.616	1.1	0.40	0.39	0.84	0.88
P02	0.618	1.1	0.43	0.40	0.84	0.88
P03	0.259	1.1	0.35	0.40	0.56	0.63
P04	0.259	1.1	0.43	0.40	0.60	0.63
P05	0.262	37.4	0.42	0.40	2.58	2.09
P06	0.261	0.2	0.40	0.40	0.22	0.22
P07	0.630	0.2	0.43	0.39	0.48	0.34
N01	0.623	0.7	0.41	0.39	0.75	0.67
N02	0.623	21.6	0.39	0.40	3.43	3.91
N03	0.623	117.0	0.40	0.40	4.61	5.07
N04	0.294	117.0	0.39	0.40	3.06	2.52
N05	0.294	218.0	0.40	0.40	3.65	2.55
N06	0.027	117.0	0.39	0.40	1.22	0.24
N07	0.027	218.0	0.41	0.40	3.89	0.24
N08	0.027	218.0	0.40	0.40	3.64	0.24
N09	0.027	218.0	0.40	0.39	3.46	0.24

Table 3-1 – Results of numerical experiment #01

Numerical experiment #02 – Effect of size of contact area

It is known that the size of contact area between the grains is very important for modeling of heat transfer through porous media (Kaviany 1999). In order to estimate the influence of contact area on the effective thermal conductivity a simple model was set up. The model consists of two spheres with 1 mm radius (r_s) located at a distance of d mm and placed inside a cylinder (see Figure 3-14). The model is axial symmetric. Constant temperature boundary conditions are kept at the top and the bottom of the model. The outer surface of the cylinder is insulated. Thermal conductivity of fluid is kept constant at $1 \frac{W}{m \cdot K}$, while the thermal conductivity of solid was 10, 100, 1000, 10000 $\frac{W}{m \cdot K}$. The parametric numerical problem was solved with distance between the spheres as a parameter with range from -1 mm to 0.5 mm. Minus sign means that spheres are located apart while plus sign means that spheres are overlapped.
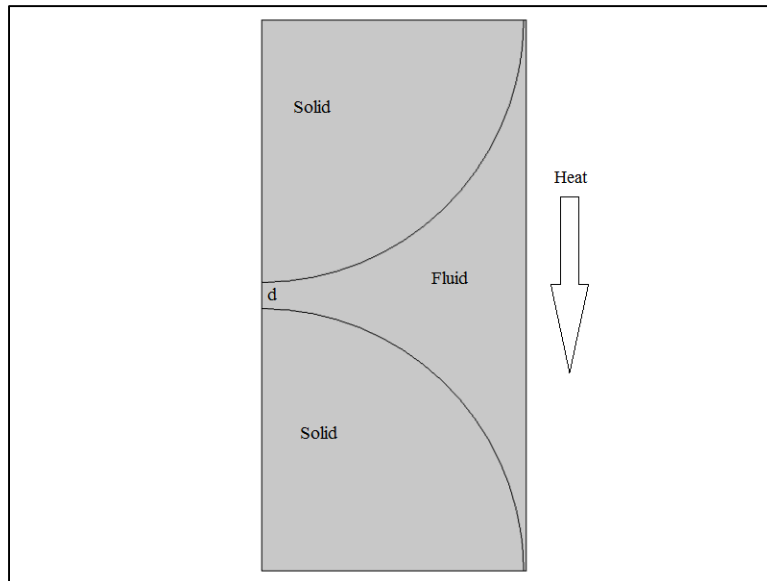
Figure 3-14 – Numerical experiment #02 geometry

The results of the numerical experiment are presented in Table A-1 in Appendices A. The smaller range for the distance between the spheres was further investigated (-0.1 mm to 0.1 mm) in order to better see the near contact region. Results are presented in Table A-2 in Appendices A.

Numerical experiment #03 – Effect of mesh size

Numerical simulations with finite element method are sensitive to mesh element size on which equations are to be solved. In order to investigate the effect of mesh size on pore scale level heat transfer model the following numerical experiment was set up. The model consists of two spheres placed inside the cube (see Figure 3-15). Spheres are solid and the rest is fluid. Thermal conductivity of fluid was $1\frac{W}{m \cdot K}$, while thermal conductivity of solid was varying in range from $10^{-4}\frac{W}{m \cdot K}$ to $10^{4}\frac{W}{m \cdot K}$. Two boundaries were kept at a constant temperature while the others were insulated. Two cases were investigated: touching spheres and non-touching spheres. For each case the parametric numerical model was solved with mesh size being a varying parameter. Five different meshes were used and its parameters are summarized in Table 3-2. The meshes are presented in Figure 3-16.
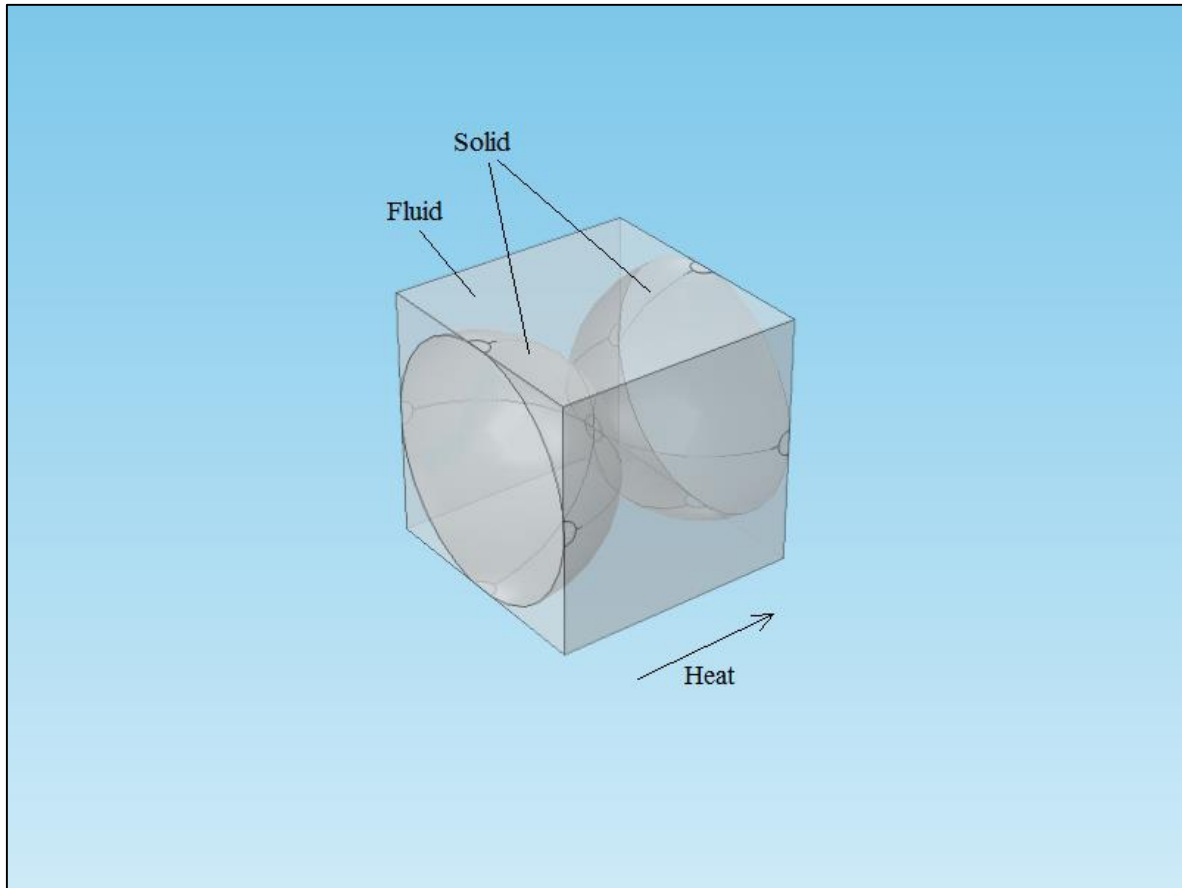
Figure 3-15 – Numerical experiment #03 geometry

Parameter	Mesh1	Mesh2	Mesh3	Mesh4	Mesh5
Maximum element size, mm	0.201	0.161	0.111	0.0704	0.0402
Minimum element size, mm	0.0362	0.0201	0.00804	0.00302	0.000402
Maximum element growth rate	1.5	1.45	1.4	1.35	1.3
Curvature factor	0.6	0.5	0.4	0.3	0.2
Resolution of narrow regions	0.5	0.6	0.7	0.85	1

Table 3-2 – Summary of mesh parameters

Mesh1   Mesh2   Mesh3   Mesh4   Mesh5
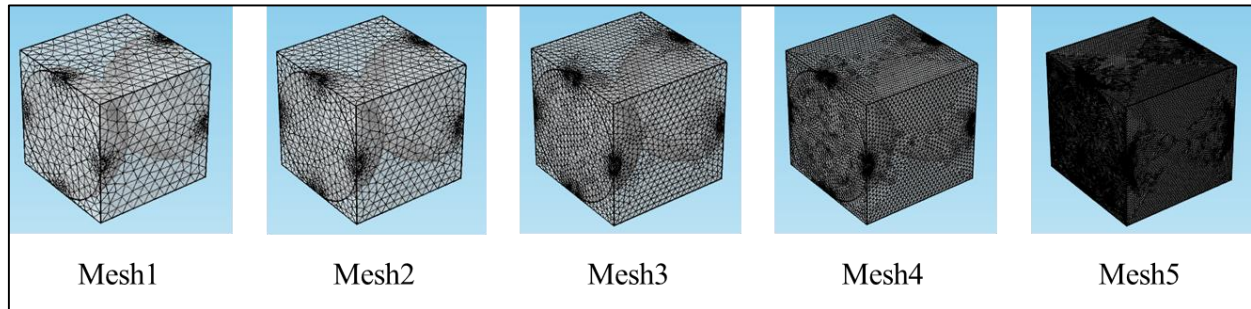
Figure 3-16 – Different mesh size

The cases of touching spheres and non-touching spheres numerical experiment results are presented in Table 3-3 and Table 3-4 respectively.

k_s, $\frac{W}{m \cdot K}$	Effective thermal conductivity, $\frac{W}{m \cdot K}$				
	Mesh1	Mesh2	Mesh3	Mesh4	Mesh5
0.0001	0.33	0.33	0.33	0.33	0.33
0.0003	0.33	0.33	0.33	0.33	0.33
0.0007	0.33	0.33	0.33	0.33	0.33
0.0018	0.34	0.34	0.34	0.34	0.34
0.0048	0.34	0.34	0.34	0.34	0.34
0.0127	0.35	0.35	0.35	0.35	0.35
0.0336	0.36	0.36	0.36	0.36	0.36
0.089	0.41	0.41	0.41	0.41	0.41
0.23	0.53	0.53	0.53	0.53	0.53
0.62	0.78	0.78	0.78	0.78	0.78
1.6	1.30	1.30	1.30	1.30	1.30
4.3	2.26	2.26	2.26	2.26	2.26
11.3	3.85	3.85	3.85	3.85	3.85
30	6.53	6.53	6.52	6.52	6.51
79	11.88	11.87	11.83	11.79	11.78
207	24.70	24.65	24.51	24.37	24.29
546	57.81	57.67	57.22	56.78	56.55
1438	144.81	144.41	143.17	141.93	141.25
3793	374.08	373.01	369.65	366.28	364.45
10000	978.52	975.68	966.76	957.78	952.90

Table 3-3 – Effect of mesh size (touching spheres)

k_s, $\frac{W}{m \cdot K}$	Effective thermal conductivity, $\frac{W}{m \cdot K}$				
	Mesh1	Mesh2	Mesh3	Mesh4	Mesh5
0.000	0.36	0.35	0.35	0.35	0.35
0.000	0.36	0.35	0.35	0.35	0.35
0.001	0.36	0.35	0.35	0.35	0.35
0.002	0.36	0.36	0.36	0.36	0.36
0.005	0.36	0.36	0.36	0.36	0.36
0.013	0.37	0.37	0.37	0.37	0.37
0.034	0.38	0.38	0.38	0.38	0.38
0.089	0.43	0.43	0.43	0.43	0.43
0.23	0.54	0.54	0.54	0.54	0.54
0.62	0.79	0.79	0.79	0.79	0.79
1.6	1.29	1.29	1.29	1.29	1.29
4.3	2.19	2.19	2.19	2.19	2.19
11.3	3.51	3.52	3.54	3.54	3.54
30	4.99	5.03	5.08	5.08	5.08
79	6.15	6.22	6.34	6.34	6.34
207	6.79	6.90	7.08	7.08	7.08
546	7.09	7.21	7.42	7.41	7.42
1438	7.21	7.34	7.56	7.55	7.54
3793	7.25	7.39	7.62	7.60	7.48
10000	7.2725	7.4049	7.6403	7.5844	7.7031

Table 3-4 – Effect of mesh size (non-touching spheres)

Numerical experiment #04 – Effect of meshing approach

In order to compare the two different meshing approaches described in the previous section, the same virtual porous media pattern was meshed using the geometry-based meshing and voxel-based meshing. Data from Prasad *et al.* (Prasad, *et al.* 1989) were used as a basis for the porous pattern generation. Patterns created for numerical experiment #1 (P01-P07) were also pixelized and converted into voxel-based geometry. For each porous pattern a voxel-based mesh was created and an effective thermal conductivity was calculated. Results are presented in Table 3-5.

Test ID	Liquid TC	Solid TC	Experiment		Geometry-based mesh		Voxel-based mesh	
			Porosity	ETC	Porosity	ETC	Porosity	ETC
P01	0.616	1.1	0.40	0.837	0.39	0.880	0.41	0.667
P02	0.6182	1.1	0.43	0.842	0.40	0.884	0.47	0.841
P03	0.2585	1.1	0.35	0.559	0.40	0.635	0.41	0.629
P04	0.2585	1.1	0.43	0.597	0.40	0.634	0.41	0.630
P05	0.26173	37.4	0.42	2.584	0.40	2.095	0.41	6.06
P06	0.2608	0.2	0.40	0.221	0.40	0.223	0.224	0.413
P07	0.62992	0.2	0.43	0.479	0.39	0.341	0.347	0.413

Table 3-5 – Numerical experiment #04 results

Numerical experiment #05 – Thermal conductivity of sandstone

Three different approaches to create porous space were used in this numerical study. The first approach was based on CT images of glass beads packed in a cylindrical tube. Seven different porous patterns were generated (USN1 to USN7). The second approach was based on the pattern generation algorithm. Seven different porous patterns were generated (USD1 to USD7). The third approach was based on CT images of real core samples. Seven different porous patterns were generated (CLE1 to CLE7). A summary of the patterns is presented in Table 3-6.

Patterns USD1, USN1 and CLE1 were "saturated" with either air, water or oil at different temperatures. Thermal conductivities of sandstone (Birch and Clark 1940), air (McQuillan, Culham and Yovanovich 1984), water (Farouq Ali 1974) and oil (Bland and Davidson 1967) at different temperatures were taken from literature and are presented in Table 3-7.The results of this numerical experiment are presented in Table 3-8.

Patterns USD1-USD7, USN1-USN7, CLE1-CLE7 were saturated with either air, water or oil at constant temperature. The results of this numerical experiment are presented in Table 3-9.

Pattern #	USD		USN		CLE	
	Length, mm	Porosity	Length, mm	Porosity	Length, mm	Porosity
1	5	0.46	0.5	0.55	34	0.3
2	5	0.43	0.5	0.69	19	0.43
3	5	0.45	0.5	0.69	26	0.38
4	5	0.44	0.5	0.18	19	0.36
5	5	0.43	0.5	0.29	17	0.34
6	5	0.44	0.5	0.2	21	0.4
7	5	0.47	0.5	0.4	21	0.35

Table 3-6 – Summary of patterns for numerical experiment #05

Temperature	Air TC	Water TC	Oil TC	Sand TC
$°C$	$\dfrac{W}{m \cdot K}$	$\dfrac{W}{m \cdot K}$	$\dfrac{W}{m \cdot K}$	$\dfrac{W}{m \cdot K}$
20	0.0256	0.601	0.114	6.32
40	0.0271	0.628	0.113	5.91
60	0.0285	0.650	0.112	5.55
80	0.0299	0.667	0.110	5.23
100	0.0313	0.679	0.109	4.95
120	0.0326	0.686	0.108	4.70
140	0.0339	0.689	0.107	4.49
160	0.0352	0.687	0.105	4.31
180	0.0364	0.679	0.104	4.15
200	0.0377	0.668	0.103	4.01

Table 3-7 – Thermal conductivity of air, water, oil and sand

	USD1 ETC, $\frac{W}{m \cdot K}$			USN1 ETC, $\frac{W}{m \cdot K}$			CLE1 ETC, $\frac{W}{m \cdot K}$		
Temperature	Air	Water	Oil	Air	Water	Oil	Air	Water	Oil
20	1.34	2.49	1.59	0.95	2.04	1.17	2.28	3.24	2.48
60	1.19	2.36	1.42	0.85	1.95	1.05	2.01	2.99	2.20
100	1.08	2.23	1.29	0.77	1.87	0.96	1.81	2.77	1.98
140	1.00	2.10	1.19	0.71	1.78	0.89	1.66	2.59	1.81
180	0.94	1.99	1.11	0.67	1.70	0.83	1.54	2.43	1.69
220	0.89	1.89	1.05	0.64	1.61	0.79	1.46	2.29	1.59

Table 3-8 – Numerical experiment #05 effective thermal conductivity vs. temperature

#	USD ETC, $\frac{W}{m \cdot K}$			USN ETC, $\frac{W}{m \cdot K}$			CLE ETC, $\frac{W}{m \cdot K}$		
	Air	Water	Oil	Air	Water	Oil	Air	Water	Oil
1	1.34	2.49	1.59	0.95	2.04	1.17	2.28	3.24	2.48
2	1.52	2.66	1.77	0.30	1.44	0.55	1.10	2.27	1.36
3	1.41	2.55	1.65	0.30	1.44	0.55	0.78	2.18	1.10
4	1.45	2.58	1.69	4.09	4.60	4.19	1.34	2.65	1.62
5	1.53	2.67	1.78	2.91	3.69	3.07	1.76	2.87	2.01
6	1.43	2.58	1.68	3.82	4.39	3.93	1.40	2.53	1.65
7	1.22	2.40	1.48	1.88	2.86	2.08	1.60	2.75	1.85

Table 3-9 – Numerical experiment #05 effective thermal conductivity vs. porosity

3.4 Discussion of results

Five different numerical experiments were conducted in order to analyze the pore scale level heat transfer model. Numerical experiment #01 was conducted in order to validate the model with real experimental data. Information about experimental setup, diameter of particles and materials used in the experiments of Prasad *et al.* (Prasad, *et al.* 1989) and Nozad *et al.* (Nozad, Carbonell and Whitaker 1985) allowed to reproduce the porous media used in these experiments. First of all one should mention that porosity of the system was on average within 1.5% (absolute value) with the maximum of 5% (absolute value) for experiment P03. The value of porosity for this experiment looks suspicious because for all of the other experiments it was more than 39%, while for this particular experiment it was 35%. Comparison of measured porosity vs. numerical porosity is presented in Figure 3-17.
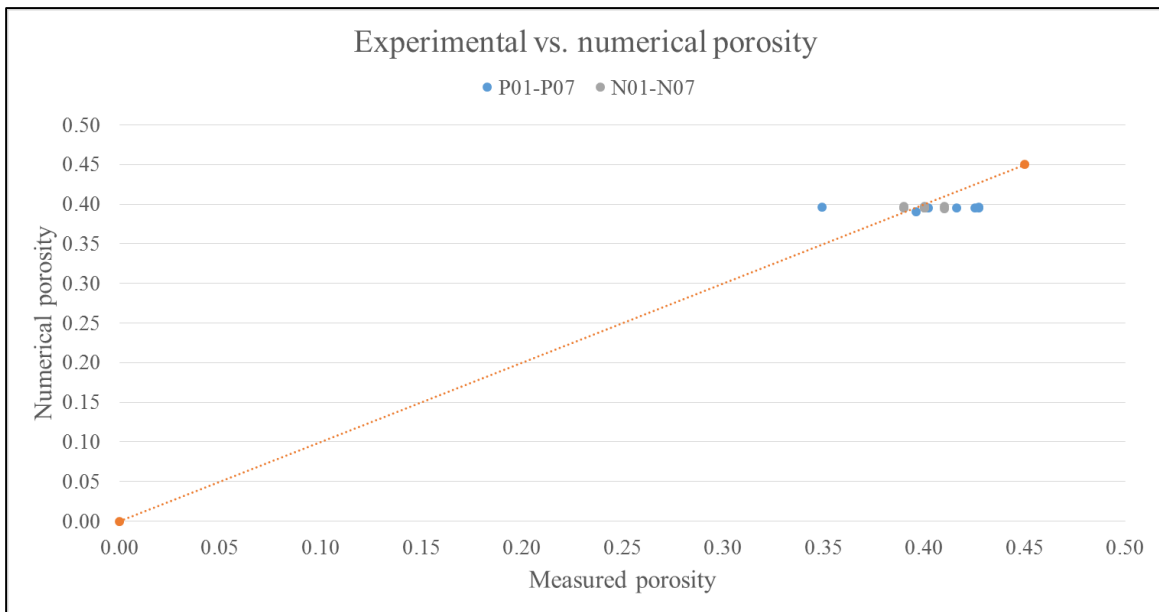
Figure 3-17 – Experimental vs. numerical porosity (numerical experiment #01)

As it comes to the effective thermal conductivity comparisons the picture becomes more interesting. Comparison of measured vs. numerical effective thermal conductivity is presented in Figure 3-18. For the set of experiments from P01-P07 the agreement is on average within 10%, while for the set of experiments N01-N09 the difference between measured and modelled effective thermal conductivities deteriorates, especially for experiments N06 to N09 where it becomes unacceptable. In order to investigate the cause for such a deviation the results should be

presented in normalized form. In Figure 3-19 the effective thermal conductivity is normalized by fluid thermal conductivity in ordinate axis and solid thermal conductivity is normalized by fluid thermal conductivity in abscissa axis. From this figure one can see that the higher the solid to fluid thermal conductivity ratio the higher the difference between modeled and measured effective thermal conductivity. In this context the experimental data P01-P07 covers mostly the lower part of the solid to fluid thermal conductivity ratio range (below 150), while the data N01-N09 covers the higher part of the solid to fluid thermal conductivity range (above 34). According to Figure 3-19 the deviation of more than 20% (of measured ETC) starts to appear mostly after the solid to fluid thermal conductivity ratio of 741, which corresponds to the experiments N05 to N09.

Two reasons are suggested to cause this problem: the effect of contact area between the grains and the effect of mesh size (numerical problem). Each of the reasons resulted in a separate numerical experiment. Numerical experiment #02 was conducted to investigate the effect of contact area between the grains and its influence on the effective thermal conductivity. Numerical experiment #03 was conducted to see how the size of finite elements affects the results of the numerical problem or in other words how sensitive the outcome to the size of the mesh.
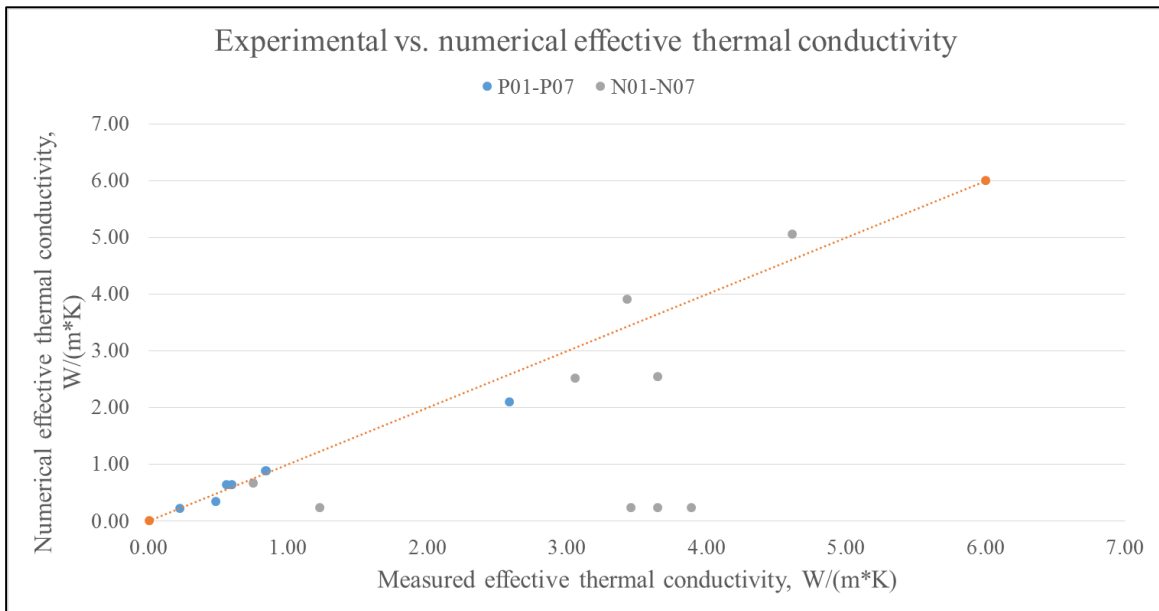
Figure 3-18 – Experimental vs numerical ETC (numerical experiment #01)
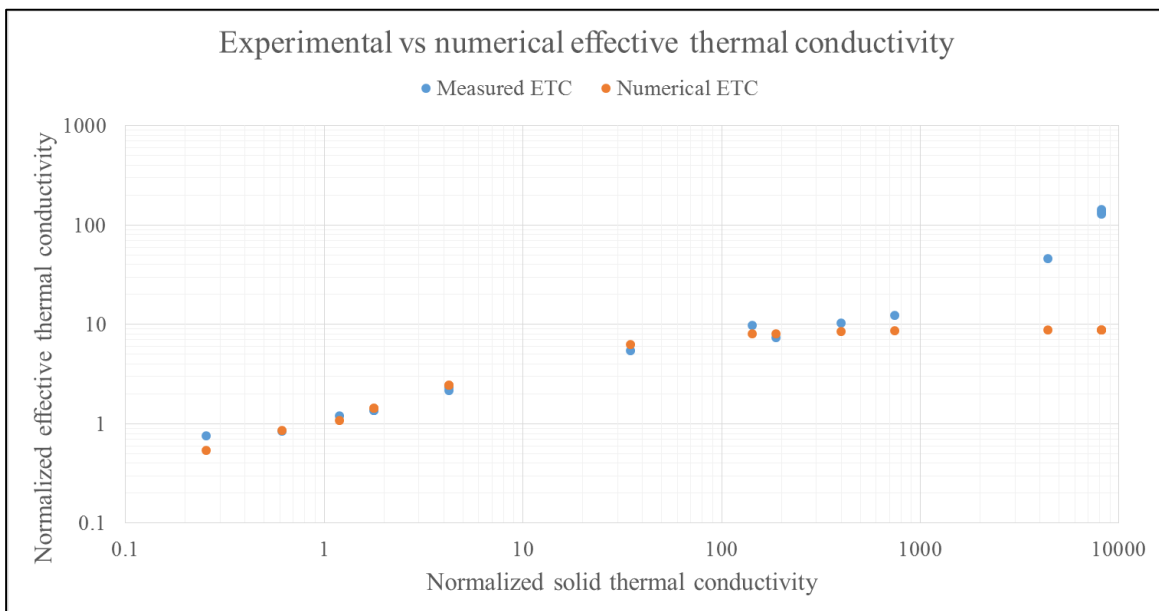
Figure 3-19 – Normalized measured vs numerical ETC (numerical experiment #01)

The main purpose of numerical experiment #02 was to see the rate of effective thermal conductivity change with changing distance between two spheres (from some distance apart to the moment of touching and to some distance overlapping).

The results of numerical experiment #02 are presented in Figure 3-20 for a wide range of distances between the spheres and in Figure 3-21 for a narrow range of distances near the

57

contact. On each of the graphs y-axis represents the normalized effective thermal conductivity of the system and x-axis represents the distance between the spheres in fraction of sphere radius. Minus sign means that spheres are located apart, zero means that there is a point contact between the spheres and plus sign means that spheres overlap. When the overlapping of spheres increases the contact area also increases accordingly. Each of these two graphs can be logically divided into three parts: before spheres touched each other, moment of touching and after the spheres touched each other. Figure 3-21 is a refinement of Figure 3-20 near the moment of touching of spheres to better capture the changes in effective thermal conductivity of the system.
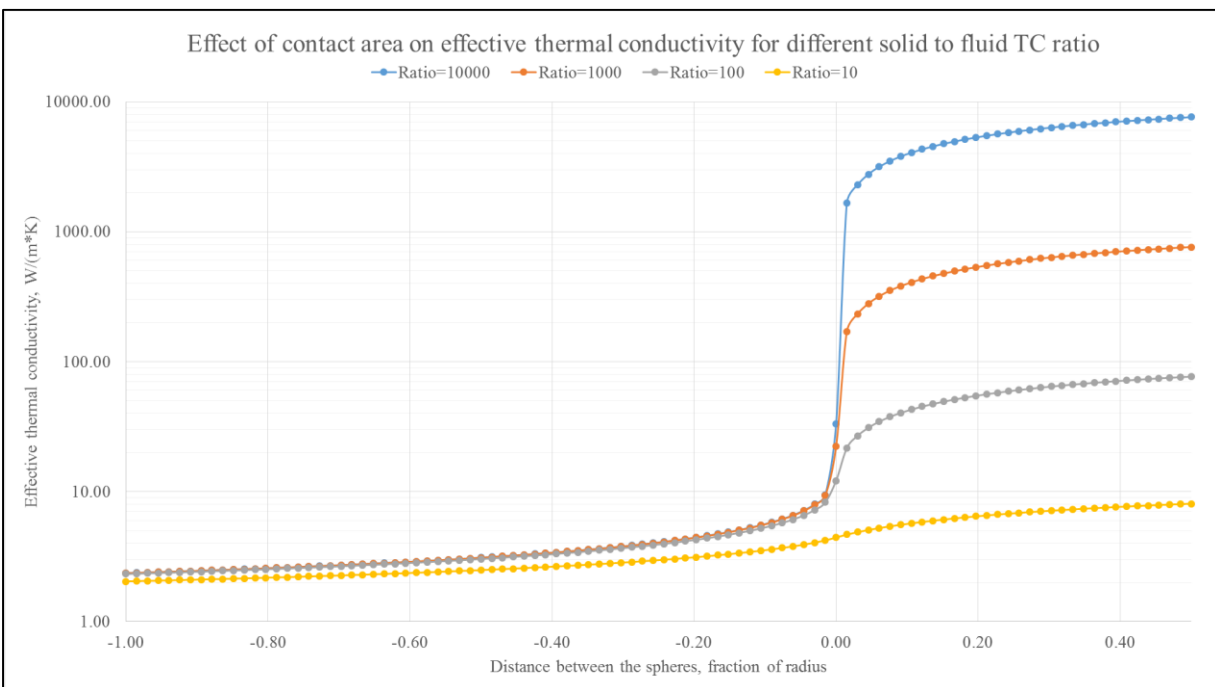
Figure 3-20 – Effect of contact area (wide range)
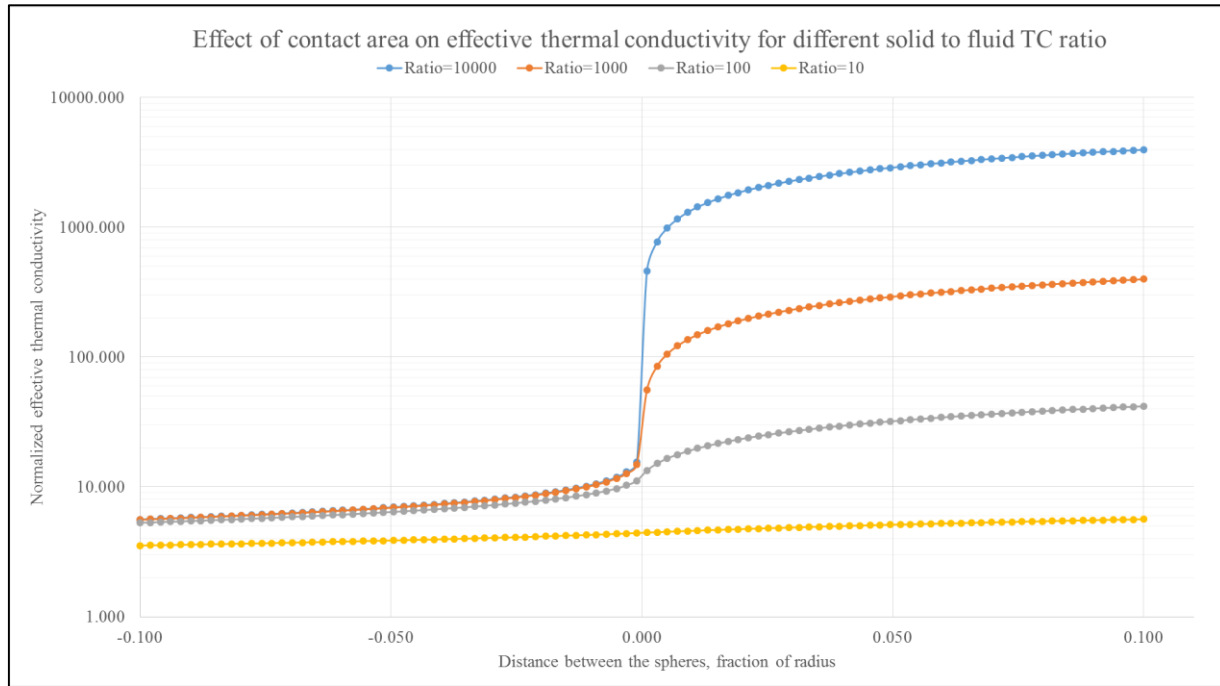
Figure 3-21 – Effect of contact area (near the contact)

The rate of ETC change is measured in $\frac{W}{m \cdot K}$ per unit change in distance between the spheres. For convenience the units of rate of change are omitted. Before the moment of touching the rate of ETC change varies in the range from 1 to 1577 with average of 31 for K_S of 10000, in the range from 1 to 854 with average of 20 for K_S of 1000, in the range from 1 to 255 with average of 10 for K_S of 100 and in the range from 1 to 15 with the average of 2.4 for K_S of 10.

The rate of ETC change at the moment of touching is 107433 for K_S of 10000, which is almost 3500 times faster than the average rate of ETC change before the moment of touching. The rate of ETC change at the moment of touching is 9800 for K_S of 1000, which is almost 500 times faster than the average rate of ETC change before the moment of touching. The rate of ETC change at the moment of touching is 625 for K_S of 100, which is almost 60 times faster than the average rate of ETC change before the moment of touching. The rate of ETC change at the moment of touching is 16 for K_S of 10, which is almost 7 times faster than the average rate of ETC change before the moment of touching.

The average rate of ETC change after the moment of touching is 12300 for K_S of 10000, 1200 for K_S of 1000, 110 for K_S of 100 and 7 for K_S of 10. The rate of ETC change at the moment of

touching is approximately 9, 8, 6 and 2 times higher than the rate of ETC change after the moment of touching for K_s of 10000, 1000, 100 and 10 respectively.

The summary of the rate of ETC change is presented in Table 3-10. There are several conclusions that can be drawn from the numerical experiment #02:

- The effective thermal conductivity of porous media with touching grains is in the order of magnitudes higher than for the one without touching grains.
- The effect of contact area is larger for larger solid to fluid thermal conductivity ratios.
- The average rate of ETC change is dramatically smaller for the case of non-touching spheres in comparison to the case of touching spheres.
- There is a huge jump in effective thermal conductivity when the spheres switch from non-touching position to touching.

Porous patterns from tests with ID N07-N09 from numerical experiment #01 exhibit a small distance between the spheres. This was done in order to be able to mesh the geometry using COMSOL build-in tools. If the spheres have a single point contact this creates a problematic place for geometry meshing. The average distance between the spheres that should touch each other for N07-N09 is around 0.0033 of the mean radius of the spheres, solid to fluid thermal conductivity ratio is around 8077. Using Table A-1 in Appendices A and applying double interpolation in between the rows and columns of the table one can calculate that the ETC growth rate is around 12.8. If we apply this correction factor to the effective thermal conductivity of numerical results N07-N09 we get effective thermal conductivity of approximately 3 $\frac{W}{m \cdot K}$, which is close to experimental result of 3.46 $\frac{W}{m \cdot K}$. This rough correction shows that the physical model used can be applied to the wide range of solid to fluid thermal conductivity ratios.

Fluid to solid TC ratio	Touching	Rate of change		
		Min	Max	Average
10000	Before	0.93	1577	31
	At the moment	107433		
	After	5234	41925	12301
1000	Before	0.95	9799	277
	At the moment	2558		
	After	522	2222	1012
100	Before	1.03	625	38
	At the moment	164		
	After	51	152	86
10	Before	1.09	625	45
	At the moment	132		
	After	51	124	79

Table 3-10 – Summary of rate of ETC change for different fluid to solid TC ratio

As it was shown above, the contact area between the grains significantly affects effective thermal conductivity predictions. But how the size of the mesh elements affects the results of numerical modeling? Numerical experiment #03 was designed to answer this question. The data from Table 3-3 and Table 3-4 are plotted in Figure 3-22 and Figure 3-23 respectively.
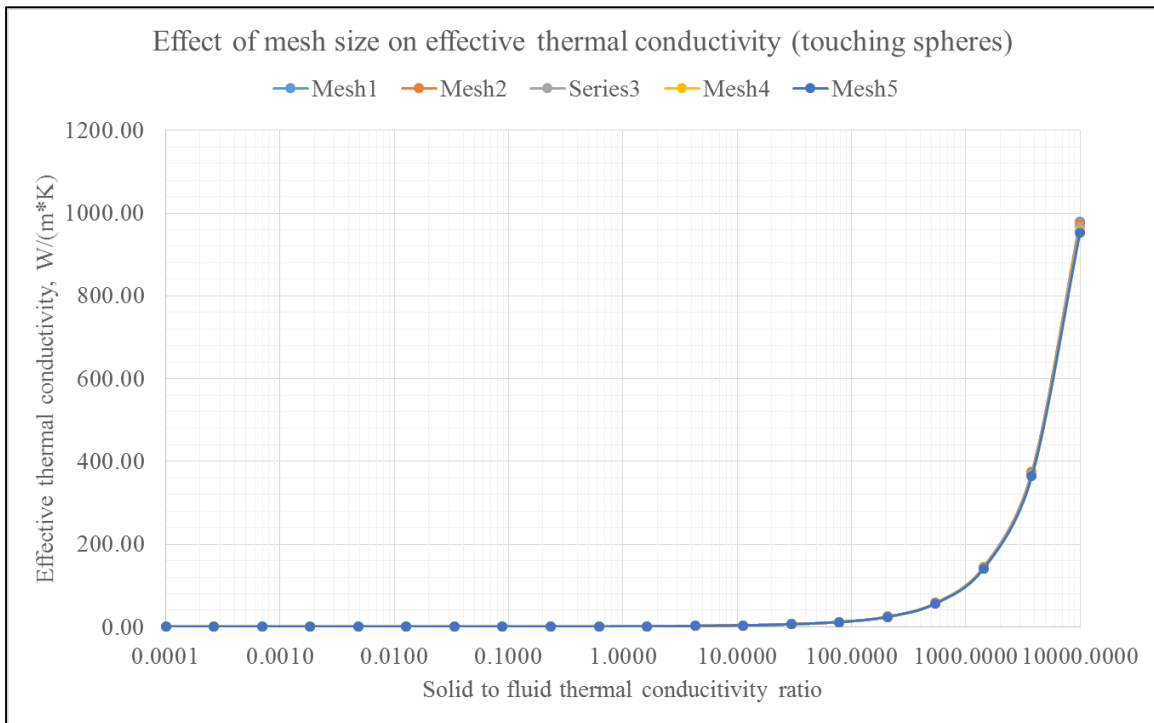
Figure 3-22 – Effect of mesh size on ETC (touching spheres)
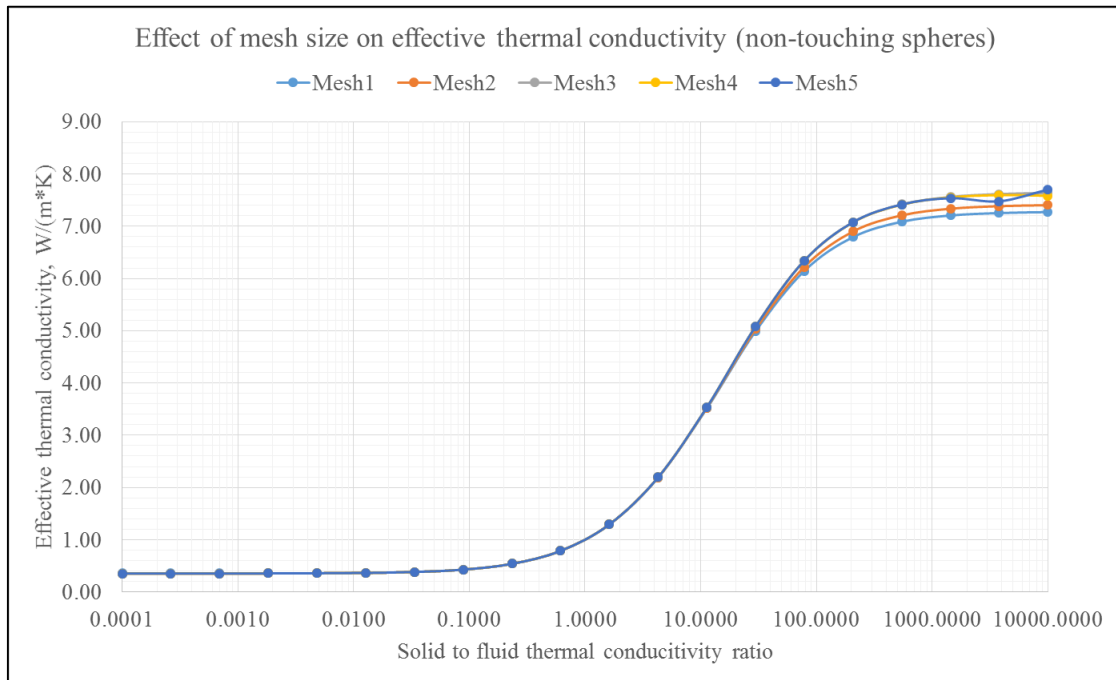
Figure 3-23 – Effect of mesh size on ETC (non-touching spheres)

From the graphs one can see that the effective thermal conductivity is not sensitive to mesh size for the solid to fluid thermal conductivity ratio less than 30 in case of non-touching spheres and less than 200 in case of touching spheres. For solid to fluid thermal conductivity ratios higher than the above mentioned values in both cases the effect of mesh size is not very significant. In the worst case for touching spheres the difference in ETC between the finest and the coarsest mesh is around 6%, while for non-touching spheres it is around 3%. The overall conclusion that numerical dependence on the mesh size for the heat transfer at a pore scale level is not significant for low solid to fluid thermal conductivity ratios. But when we move to a higher values of solid to fluid thermal conductivity ratios the preference should be given to finest mesh possible. Of course the finer the mesh, the more elements it contains and the more time required to solve the numerical problem. Thus there should be a balance between the number of mesh elements and computational time so that the error in calculating effective thermal conductivity of porous pattern stays within acceptable range.

Numerical experiment #04 was conducted to see the difference between two meshing approaches: voxel-based and geometry based. For that purpose exactly the same geometries P01-P07 were meshed using these two approaches and results of numerical modelling are plotted in Figure 3-24 and Figure 3-25. From the first figure one can notice that in general there is a good match in porosity between the different meshing approaches. Only one pattern P02 has abnormally high porosity for voxel-based meshing approach. As for the effective thermal conductivity voxel-based meshing has good agreement for all the cases but P05. In case of P05 solid to fluid thermal conductivity ratio is much higher than in other cases. A possible explanation to this is the effect of contact area between the grains. Voxel-based meshing assumes certain resolution for images. In our case 250x250x250 pixels resolution was used to pixelize the original geometry. There are 2000 grains in a pattern, which means that approximately $\sqrt[3]{2000} \approx$ 12 grains are located along each axis direction, which in turn means approximately 21 pixel per grain. This leads to very rough representation of original geometry. This resolution was chosen due to the limitation of Simpleware ScanIP software. At 250x250x250 resolution meshing time is about 2 hours per porous pattern, while at 500x500x500 the program stuck and does not produce any result. In comparison the meshing time of geometry-based approach is 10-30 minutes per porous pattern depending on mesh size. Also the number of elements in voxel-based

mesh is much higher than in geometry-based and as a result the computational time increases from 30 minutes for geometry-based mesh to 3 hours for voxel-based mesh.

As a result of these three disadvantages of voxel-based meshing the preference is given to the geometry-based meshing, which was used for all other numerical experiments.
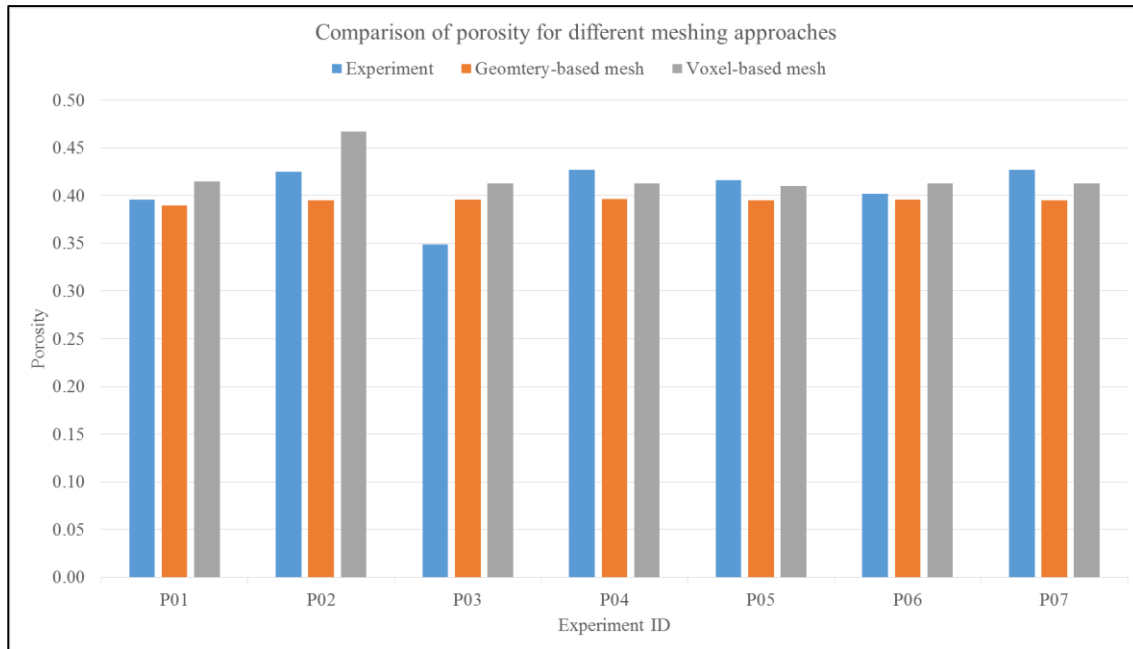
Figure 3-24 – Effect of meshing approach on porosity
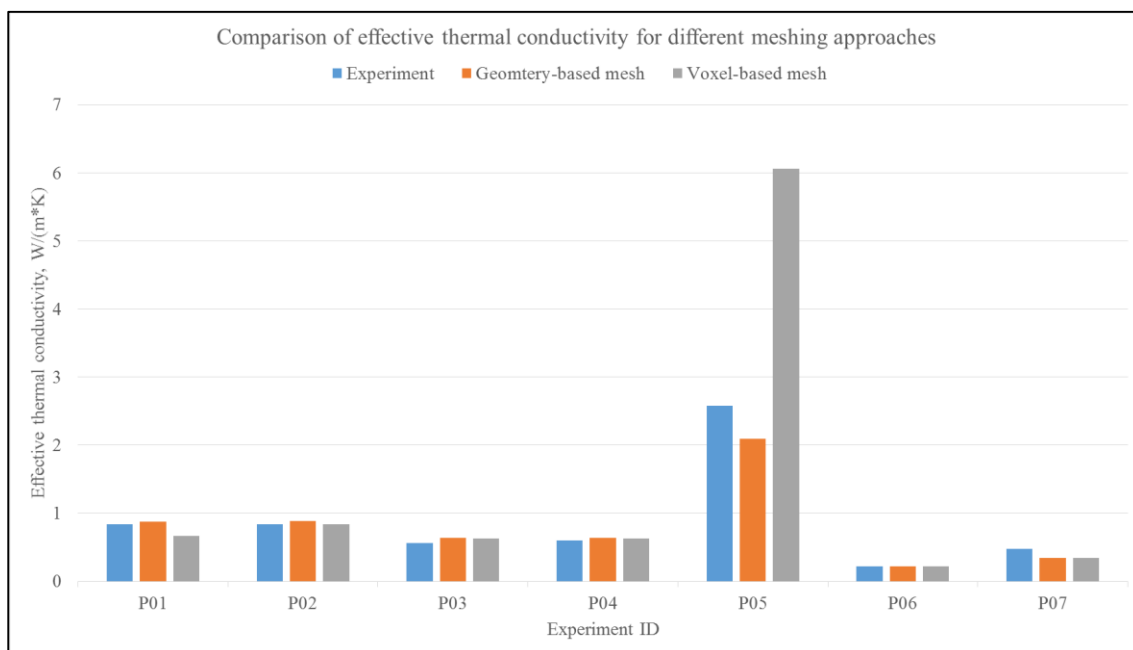
Figure 3-25 – Effect of meshing approach on effective thermal conductivity

Numerical experiment #05 was conducted to compute the effective thermal conductivity of sandstones with different porosities, saturated with different fluids and at different temperatures. USD samples were generated using pattern generation algorithm and have a small range of porosity variation (0.42 – 0.48), due to the fact that the patterns were produced as tight as possible. Certain contact area between the grains was considered because of its importance. USN samples were generated from CT scans of the glass beads placed inside the cylinder. Variation of porosity was then created by artificially fusing grains and thus reducing the pore space (0.18 – 0.69). CLE samples were created using CT scans of real core samples. Using a certain threshold level of grayscale values the porous space was created. Different samples represent different parts of real core. Variation of porosity is in the range of 0.3 to 0.43.

The first part of numerical experiment #05 was related to analyzing the effect of temperature variation on the effective thermal conductivity of porous samples. For this purpose temperature dependent properties of constituents were used. The results of this part of the experiment are presented in Figure 3-26, Figure 3-27 and Figure 3-28. From the graphs one can conclude that effective thermal conductivity is a linear function of temperature with R^2 values close to one. When temperature increases the effective thermal conductivity of sample decreases. Most likely this behaviour is due to the fact that sand grains have the highest thermal conductivity among other constituents and its value significantly drops with temperature. In other words sand material dictates the overall thermal conductivity behaviour in the sandstone samples.

The second part of numerical experiment #05 was related to analyzing the effect of porosity variation on the effective thermal conductivity of porous samples. The results of this part of the experiment are presented in Figure 3-29, Figure 3-30 and Figure 3-31. From the graphs one can notice that the effective thermal conductivity of porous samples decreases with increasing porosity. This fact is reasonable as it agrees with the limiting relations 1 and 2 described in Chapter 2. When porosity decreases the solid phase increases in volume and thus the effective thermal conductivity approaches that of solid phase (sand in this case), so it increases; and otherwise when porosity increases. Also one can notice that there is a jump in effective thermal conductivity of CLE samples vs. porosity. This might be due to the fact that CT images can only be meshed using voxel-based approach and as it was demonstrated from other numerical experiment that can sometimes give suspicious results.
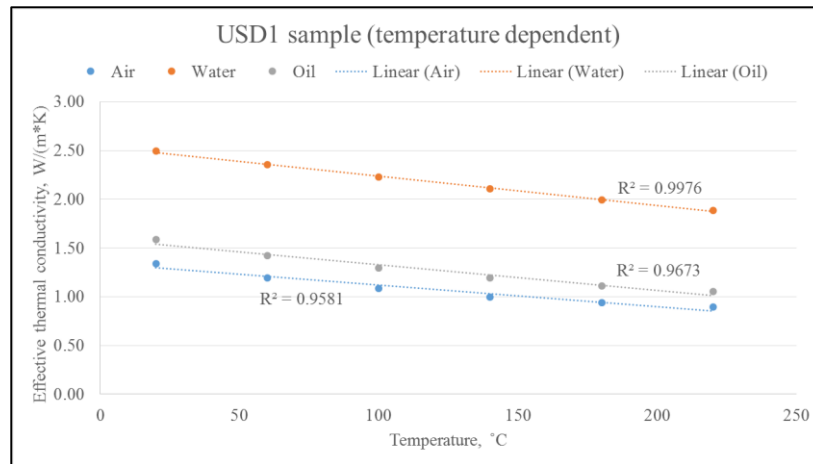
Figure 3-26 – Temperature dependent ETC of USD1 sample
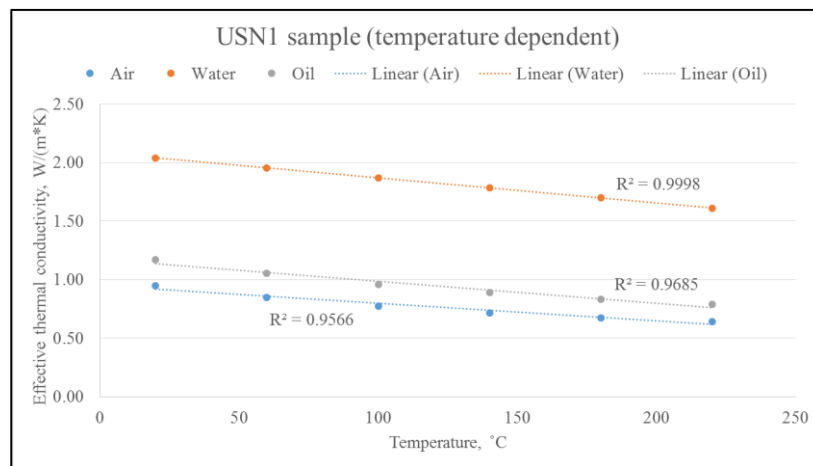
Figure 3-27 – Temperature dependent ETC of USN1 sample
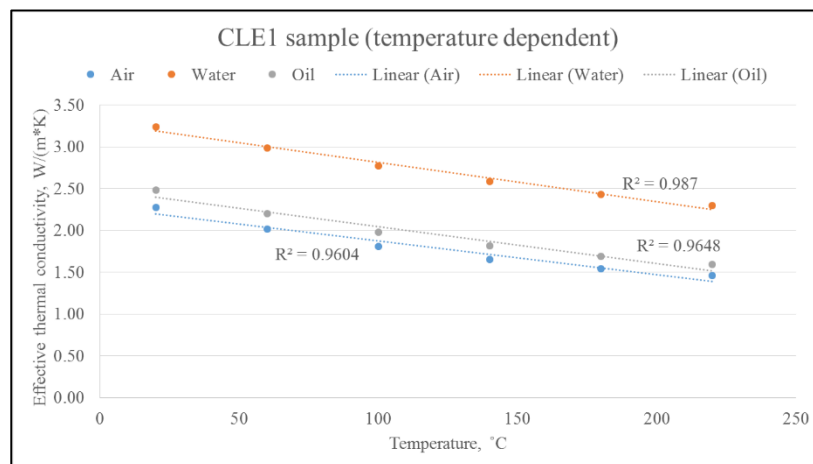
Figure 3-28 – Temperature dependent ETC of CLE1 sample

66
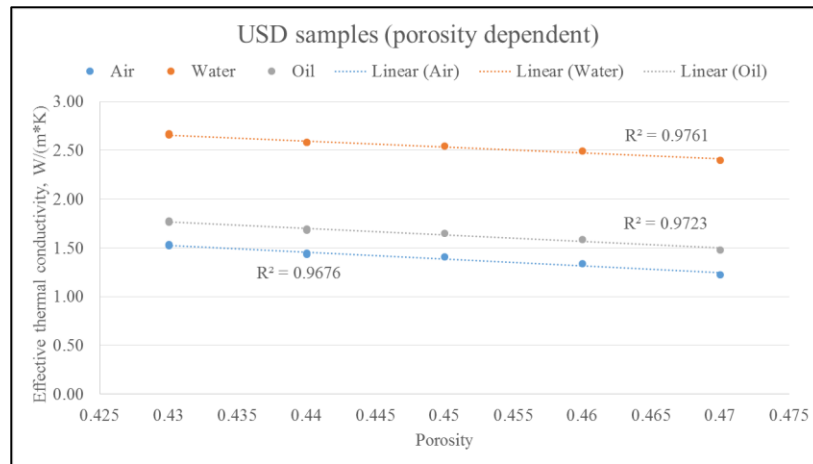
Figure 3-29 – Porosity dependent ETC of USD samples
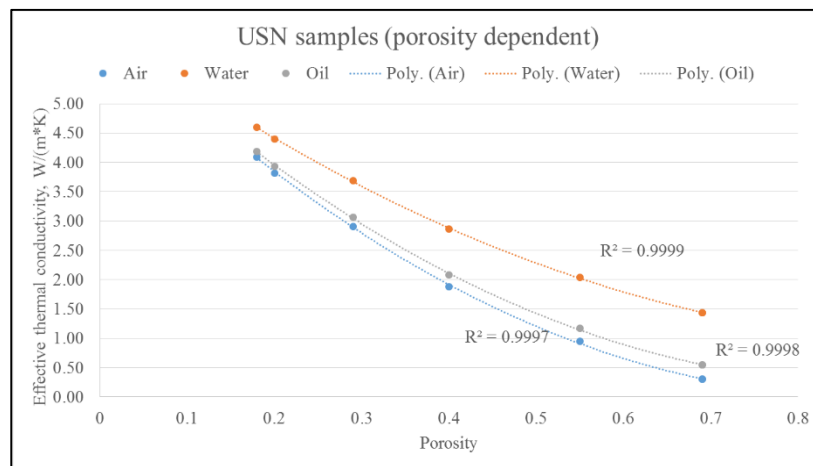
Figure 3-30 – Porosity dependent ETC of USN samples
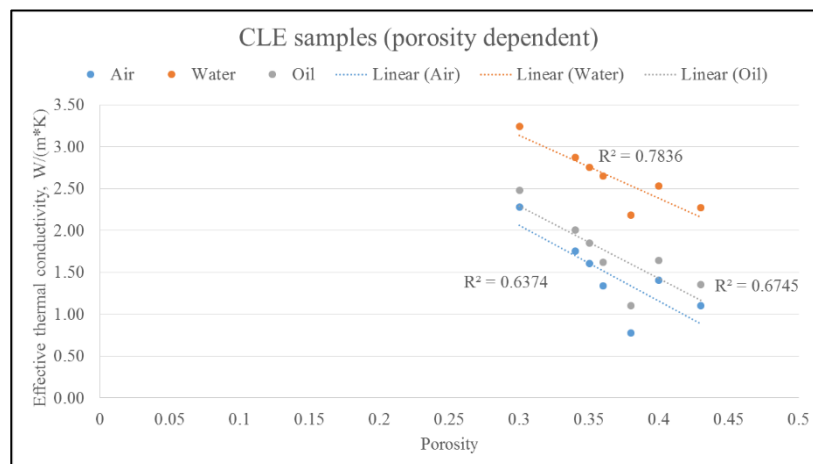
Figure 3-31 – Porosity dependent ETC of CLE samples

67

Chapter 4: **A novel mixing rule for effective thermal conductivity predictions**

In Chapter 2 different mixing rules for predicting effective thermal conductivity of porous media were presented. All of them include thermal conductivity of constituents and porosity as input parameters, as well as all of them are very simple to use. Also it was mentioned that particle (gran) size distribution is one of the parameters that affects the effective thermal conductivity of porous media (especially unconsolidated sands). But none of the presented mixing rules can use particle size distribution as input parameter.

In Chapter 3 it was shown that a porous pattern generation algorithm along with geometry-based meshing and heat transfer physics is able to predict the effective thermal conductivity of porous media. Sensitivity analysis showed the importance of the contact area between the grains.

In this chapter a novel mixing rule is developed to include the particle size distribution of porous media as input parameter. The mixing rule is expected to apply in unconsolidated media such as oil sands.

4.1 Generation of mixing rule based on particle size distribution

In order to generate custom mixing rule for a specific porous media, the only parameter required as input is the particle (grain) size distribution of that media. An example of the particle size distribution of a real oil sand sample is presented in Figure 4-1. This sand can be classified as fine and very fine sand with coarse silt. Using this particle size distribution one can generate a porous pattern with the procedures described in Chapter 3. The resulting oil sand sample porous pattern is presented in Figure 4-2. The next step is to mesh the porous patter using geometry-based meshing approach. The result of this step is presented in Figure 4-3. Subsequently the heat conduction parametric problem is solved with solid to fluid thermal conductivity ratio being a variable parameter. The result of this step is a dependency curve of the effective thermal conductivity against the solid fluid thermal conductivity ratio. For this particular oil sand the result is presented in Figure 4-4. The final step is to fit the curve with a simple to use equation. The perfect fit is achieved by using sigmoid function:

$$K_e = \frac{a}{b + e^{-c \ln K_s}} + d \qquad \textbf{4.1}$$

Where all the coefficients a, b, c and d are positive. The coefficient of determination R^2 for this particular example is 0.9997. The above described workflow for the custom mixing rule generation is presented in Figure 4-5.

An additional set of numerical experiments was conducted in order to analyze the ability of new mixing rule approach to predict the effective thermal conductivity of porous media with known particle size distribution. The main question to be answered is how many grains is enough for the generated virtual porous media to be representative of the bulk porous media.
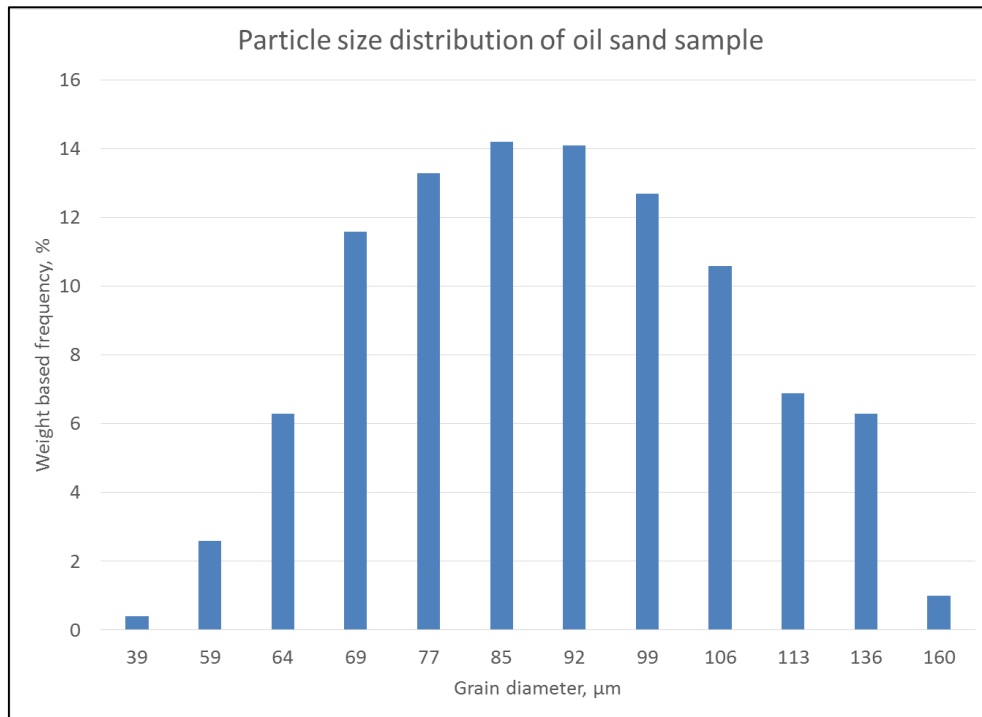
Figure 4-1 – Particle size distribution of oil sand sample
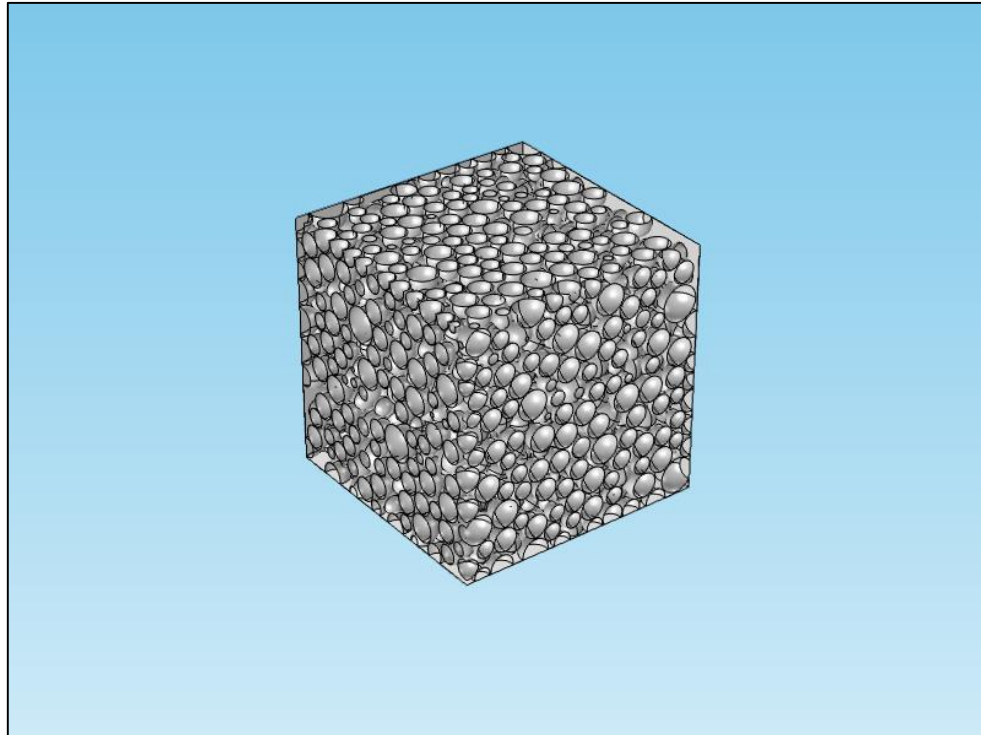
Figure 4-2 – Porous pattern of oil sand sample
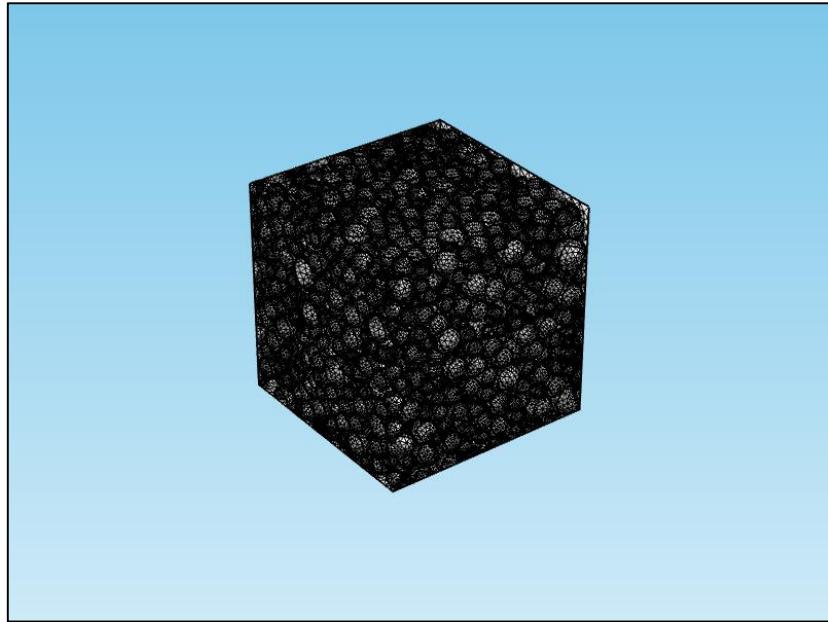
Figure 4-3 – Meshed porous pattern of oil sand sample
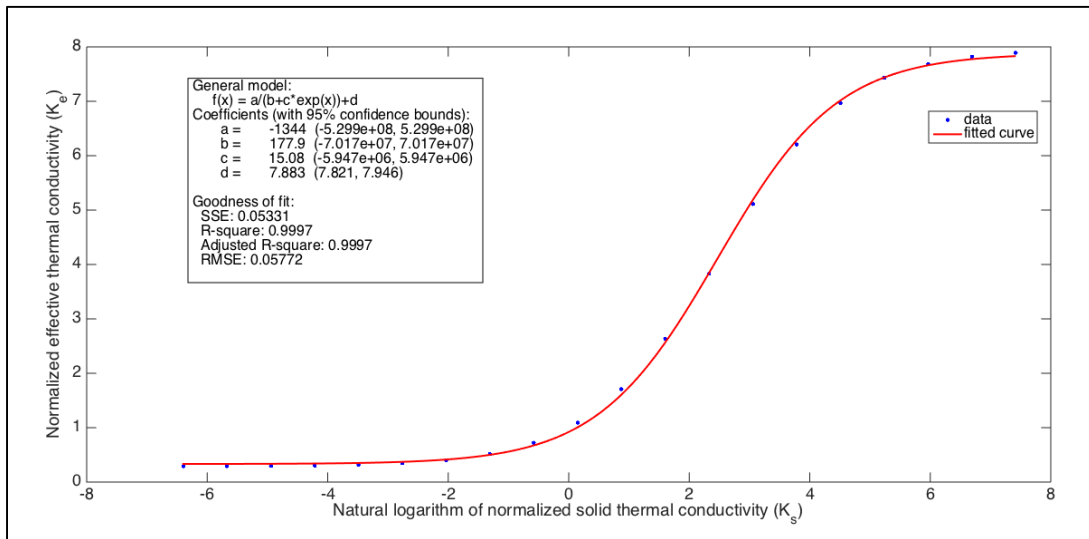
Figure 4-4 – Custom mixing rule for oil sand sample
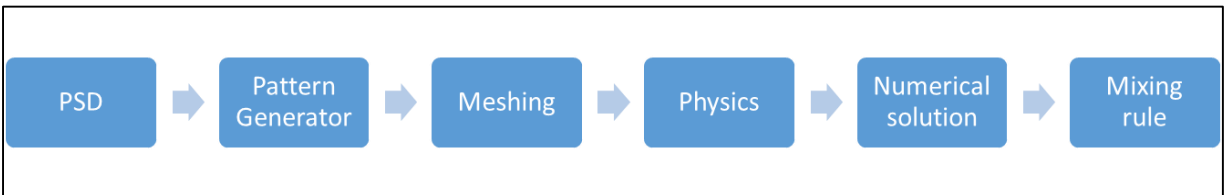
Figure 4-5 – Custom mixing rule generation workflow

4.2 Numerical experiments

In order to be representative of the bulk each generated porous pattern should have two important properties:

- Isotropy of thermal conductivity
- Different implementations of the same particle size distribution should have the same effective thermal conductivity

Both of the properties are dependent on a single parameter – the number of grains in the generated pattern. Numerical experiment #06 was conducted in order to estimate the optimal number of grains required for a generated porous pattern to fulfill the isotropy and homogeneity criteria. Numerical experiment #07 shows the experimental verification of applicability of the new mixing rule. Numerical experiment #08 was conducted to evaluate the effect of different particle size distributions on the mixing rule coefficients.

Numerical experiment #06 – Optimal number of grains estimation

In this numerical experiment a single particle size distribution was used and is presented in Table 4-1and Figure 4-6. The diameter of particles ranges from 39 μm to 160 μm with the highest frequency of particles at 69 μm. It should be mentioned that frequency that corresponds to diameter is based on number of grains as opposed to the scenario when the frequency is based on the weight of particles. The latter is usually an output from particle size distribution analysis (experiment). To convert from mass based frequency to number based frequency the following approach should be applied. An arbitrary mass of sample is assumed and it should be large enough. The mass of particles with a certain diameter is calculated from total mass using mass based frequency. Then that mass is divided by density of grains and the volume of a single grain with that diameter is calculated. The result is the number of grains that corresponds to that diameter. Finally the number based frequency can be calculated as the ratio of number of grains corresponding to that diameter to the total number of grains. Number based particle size distribution is used as input into porous patter generation algorithm.

Diameter, μm	Frequency, %
39	3.547
59	7.094
64	13.481
69	19.8683
77	16.41
85	12.951
92	10.14
99	7.33
106	4.992
113	2.653
136	1.395
160	0.138

Table 4-1 – Particle size distribution for experiment #06
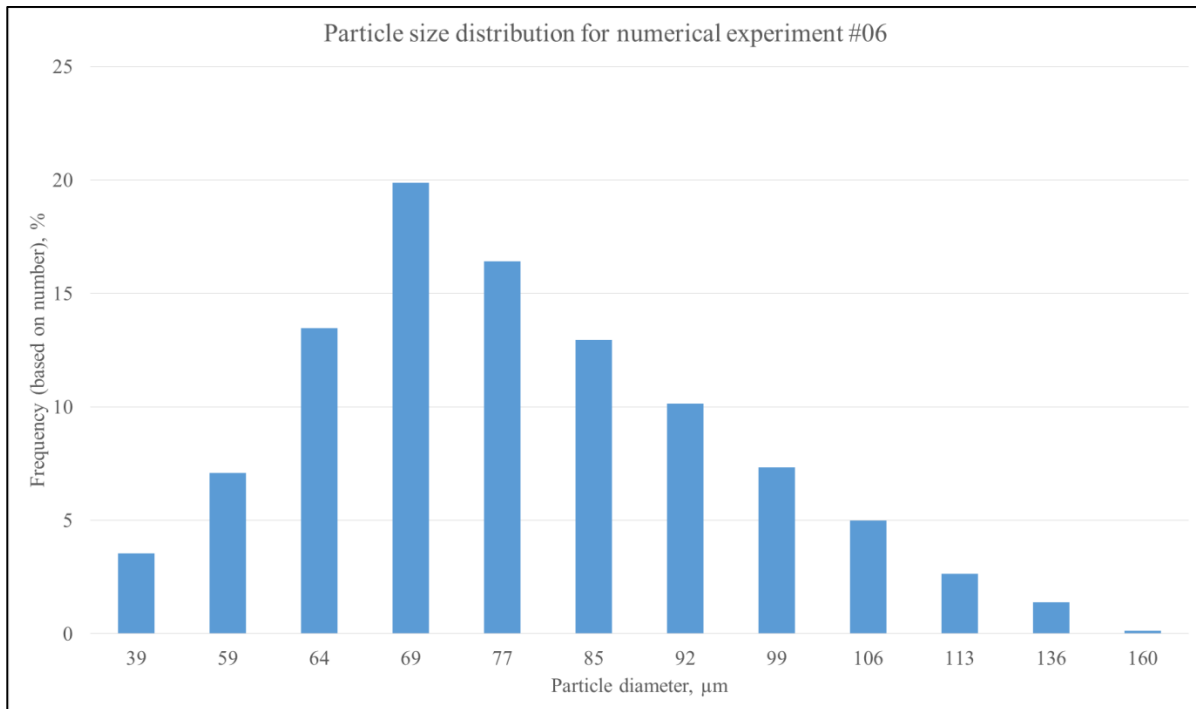
Figure 4-6 – Particle size distribution for numerical experiment #06

For the particle sized distribution in Table 4-1 a set of porous patterns was generated. The set consists of six groups. In each group all patterns has the same number of grains. Patterns form group 1 contain 300 grains each, from group 2 – 700 grains, from group 3 – 1100 grains, from group 4 – 1500 grains, from group 5 – 2000 grains and from group 6 – 2500 grains. Each group has 5 subgroups. In each subgroup the target porosity used to generate patterns is the same. Patterns from subgroup 1 has target porosity of 0.4, from subgroup 2 – 0.35, from subgroup 3 – 0.3, from subgroup 4 – 0.25 and from subgroup 5 – 0.2. The actual generated porosity value is higher than the target porosity, but it decreases from subgroup 1 to subgroup 5. Each subgroup contains 5 different random implementations of porous patterns with the number of grains corresponding to the group and target porosity corresponding to the subgroup. The total number of generated porous patterns is 150. For each pattern the thermal conductivity of solid was considered 6 $W/(m \cdot K)$, which corresponds to the thermal conductivity of sand; and the thermal conductivity of fluid was considered 0.6 $W/(m \cdot K)$, which corresponds to the thermal conductivity of water.

For each pattern two pore scale heat transfer models were set up. One model is in the X direction and the other one is in the Z direction. This was done in order to calculate the coefficient of anisotropy of the generated patterns and see the effect of the number of grains on the coefficient of anisotropy. For each model the effective thermal conductivity was calculated twice using the values of heat flux at opposite boundaries. These two values were expected to be very close and were used as an indication of numerical stability of results.

The results of numerical experiment #06 are presented in Table A-3 in Appendices A. In some cases it was not possible to mesh the pattern, so the results for that patterns are omitted.

First of all there is a need to analyze how porosity changes with different levels of target porosity and different number of grains. In Figure 4-7 porosity vs. pattern number is presented for different number of grains. Patterns with number 1-5 have the highest target porosity of 0.4, while patterns with numbers 21-25 have the lowest target porosity of 0.2. From graph we can see that the lower target porosity, the lower the pattern porosity. This trend applies to any number of grains. Also it should be mentioned that for the smallest target porosity of 0.2 (patterns 21-25 on figure) the variation in porosity is the smallest: from 0.383 to 0.402; while for the largest target porosity of 0.4 (patterns 1-5 on figure) the variation in porosity is the largest: from 0.459 to

0.523. Porosity of larger than 0.45 seems to be unrealistic for real unconsolidated porous media, while values of 0.4 and lower are acceptable. It means that in order to make the pattern as tight as possible the number of grains should be more than 2000 and the target porosity should be at least 0.2 or smaller. Pattern generation time increases with decreasing the target porosity. For 2500 grains and 0.2 target porosity the average pattern generation time was around 2 hours.

There should be specifically mentioned that the value of the target porosity to calculate the suggested final size of the box (final dimensions of the porous media) based on the mean diameter of the grains and the number of grains. But the actual final dimensions of the box can be slightly larger from the proposed ones. The increase is required in order to accommodate all the required grains in the box. The graph in Figure 4-7 has plateaus, which means that for a particular target porosity and particular number of grains the generated porous patterns have very close values of porosity and very close values of thermal conductivity (from Table A-3). This in turn demonstrates the repeatability of the pattern generation algorithm. For the custom mixing rule generation it means that any generated porous pattern is homogeneous and thus representative of the bulk porous media, so we can generate and work with only one pattern for a particular particle size distribution. This conclusion is restricted to heat transfer only.
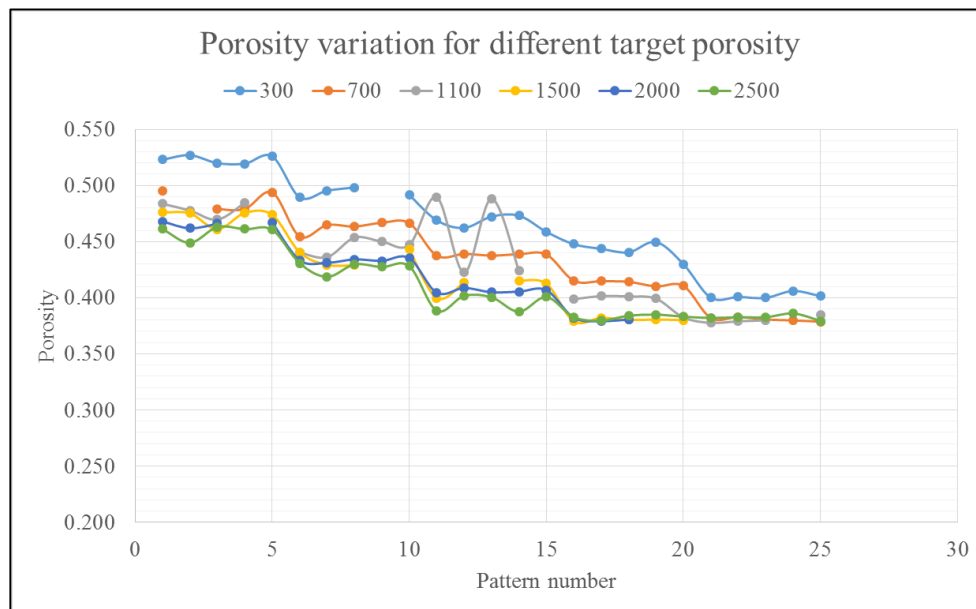
Figure 4-7 – Porosity variation for different target porosity

For each of the pattern the effective thermal conductivity was calculated for two opposite borders: for heat inlet and heat outlet. This was done in order to avoid the instability of numerical solution. With default relative tolerance of 10^{-3} the effective thermal conductivity calculated at two opposite borders was significantly different. When the relative tolerance was decreased to 10^{-5} the difference between the effective thermal conductivity on the two opposite borders became insignificant. From Table A-3 one can calculate that the average difference in effective thermal conductivity calculated at the opposite borders is 0.54%. It shows that the model is numerically stable and for the later models we can only calculate effective thermal conductivity at one of the two borders.

The next step is to analyze the heat conduction anisotropy of generated porous patterns. For this purpose the coefficient of anisotropy is calculated for each pattern as the ratio of horizontal (in X direction) thermal conductivity to vertical one (in Z direction). The graph of coefficient of anisotropy vs. number of grains is presented in Figure 4-8. The variation in coefficient of anisotropy decreases with increasing the number of grains. The coefficient of anisotropy varies from 0.99 to 1.06 for 300 grains and from 1 to 1.01 for 2500 grains. It means that for the number of grains equal to 2500 the anisotropy is around 1% and the porous pattern can be considered as isotropic, while for the 300 grains the anisotropy is around 6%.
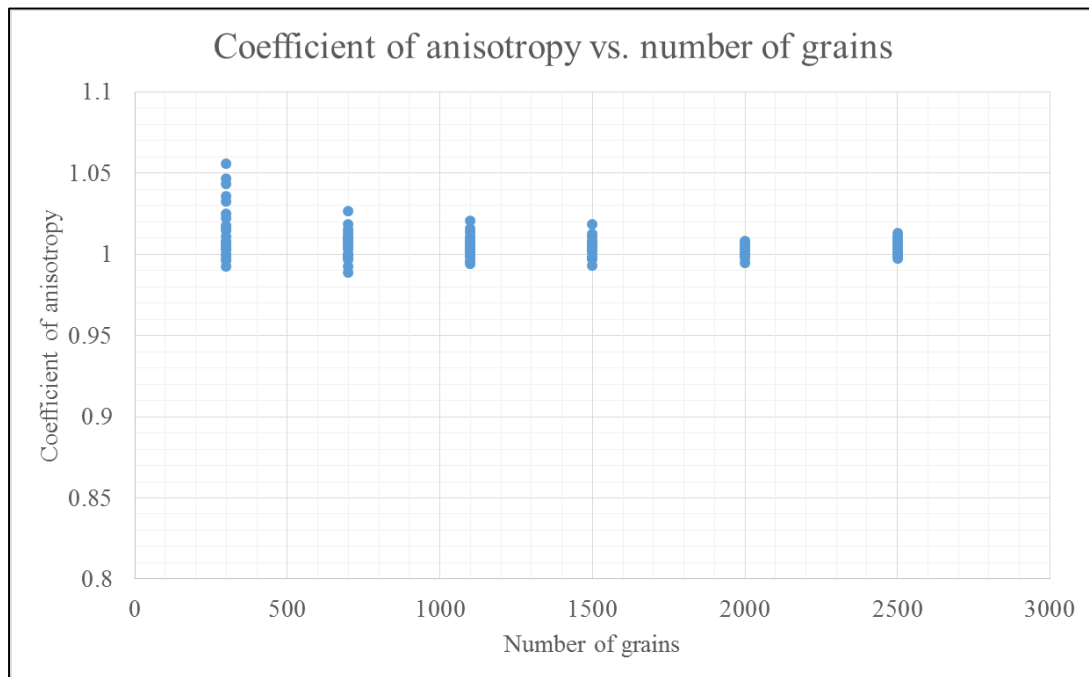
Figure 4-8 – Variation of coefficient of anisotropy with number of grains

Finally we are interested in the dependency of effective thermal conductivity on porosity. The graph in Figure 4-9 shows the dependency of effective thermal conductivity on porosity. The dependency is linear with the coefficient of determination of 0.98. It means that for a given particle size distribution the effective thermal conductivity of sand saturated with water has the linear dependency of effective thermal conductivity on porosity and using extrapolation the effective thermal conductivity can be predicted for the lower values of porosity with good accuracy.
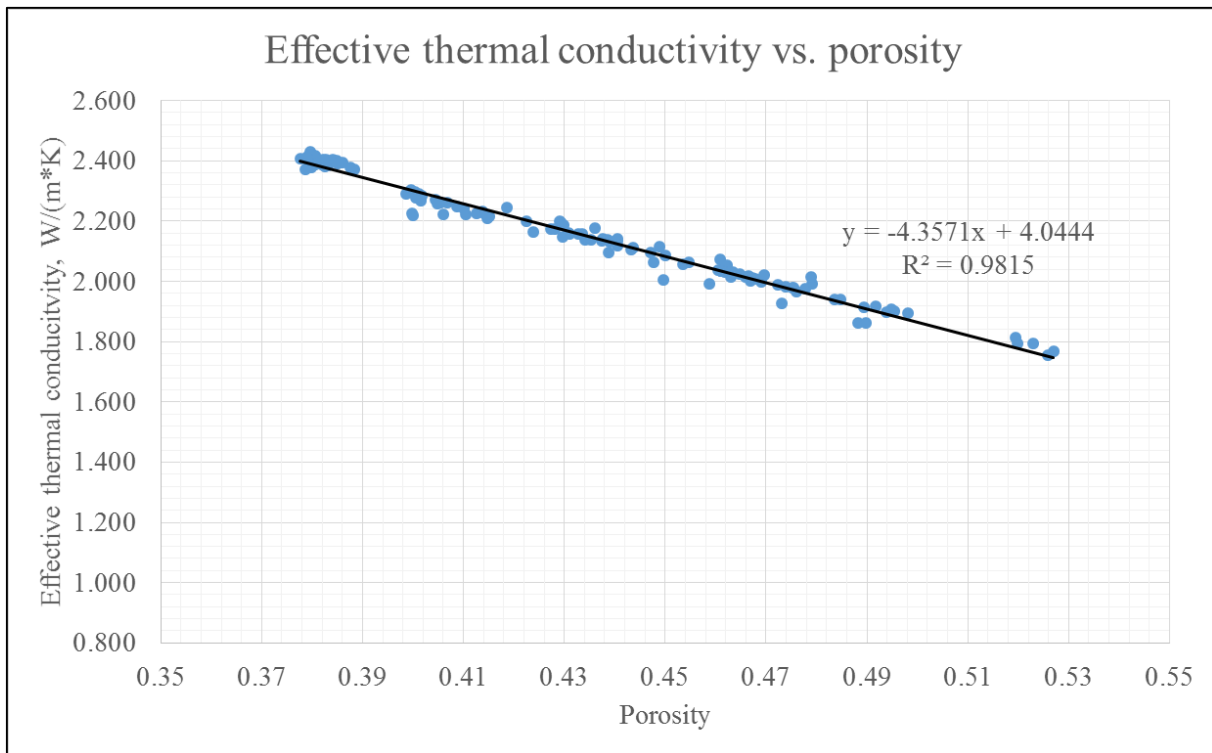
Figure 4-9 – Dependency of effective thermal conductivity on porosity

The following conclusions can be derived as a result of numerical experiment #06:

- The porous patterns produce lower values of porosity for increasing number of grains or in other words the porosity of the porous pattern with a given particle size distribution approaches its limiting value.
- The anisotropy of a porous pattern decreases with increasing number of grains
- The optimal number of grains for the porous pattern to be isotropic and have realistic value of porosity should be at least 2000 for the particle size distributions tested.

- A single pattern with the number of grains more than 2000 and target porosity 0.2 is representative of bulk porous media for the purposes of thermal conductivity prediction.
- The effective thermal conductivity of a porous pattern is a linear function of porosity for a given particle size distribution.

Numerical experiment #07 – Analysis of effect of particle size distribution

In this numerical experiment four different particle size distributions of oil sands were used for generation of the novel mixing rule. The particle size distributions are presented in Figure 4-10. PSD1 sand can be described as fine and very fine sand. PSD2 sand can be described as a combination of fine, very fine sand and coarse silt. PSD3 sand can be described as a combination of medium, fine, very fine sand and coarse silt. PSD4 sand can be described as a combination of medium, fine and very fine sand.
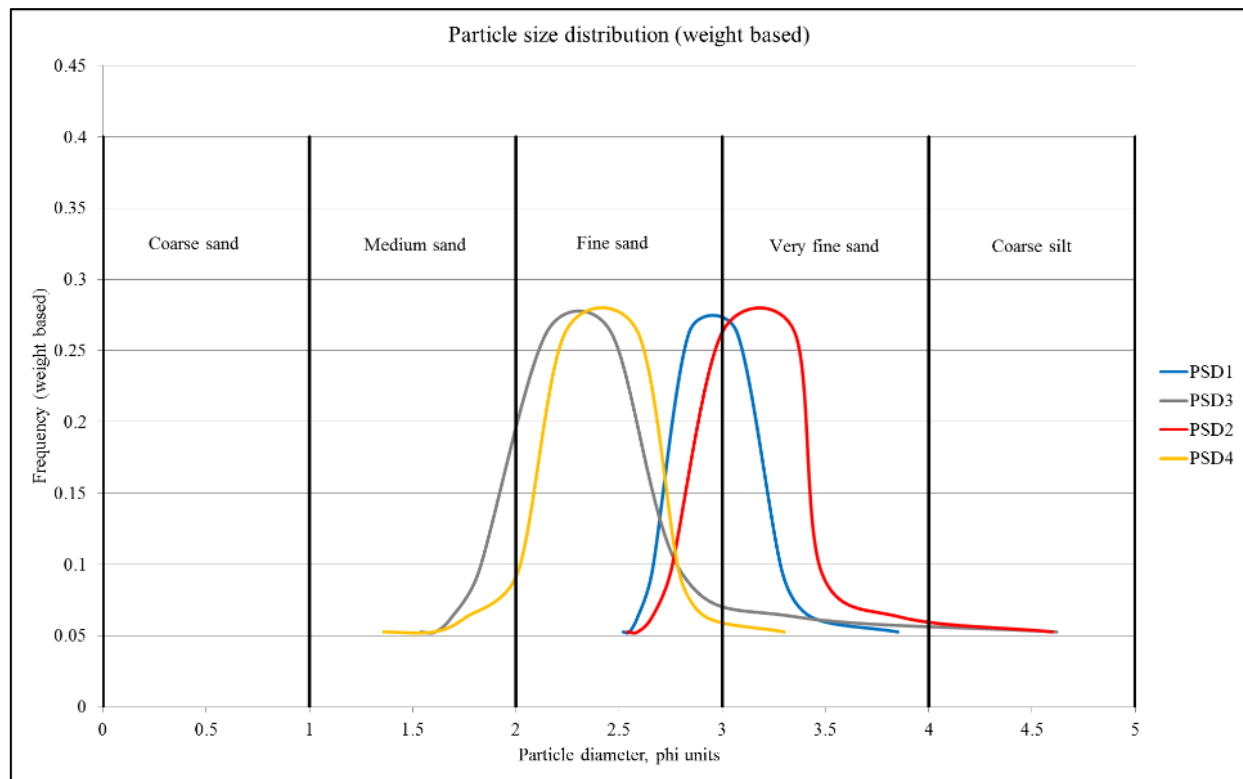
Figure 4-10 – Particle size distributions for numerical experiment #07

For each of the particle size distributions the porous pattern with 2000 grains was generated. The target porosity was 0.2. According to the results of numerical experiment #06 the porous patterns will be isotropic and have values of porosity close to realistic. The porous patterns will be

referred to as PSD1, PSD2, PSD3 and PSD4 respectively. For each of them the mixing rule equation is generated based on the procedure described at the beginning of this chapter. The numerical modelling results are presented in Table A-4 in Appendices A, the resulting coefficients of novel mixing rules are presented in Table 4-2 and the graphs are presented in Figure 4-11.

	Porosity	a	b	c	d	R^2
PSD1	0.393	0.7766	0.09719	0.9311	0.2803	1
PSD2	0.371	0.7899	0.0793	0.9082	0.2557	1
PSD3	0.380	0.7822	0.07497	0.8969	0.2578	1
PSD4	0.368	0.7951	0.07824	0.9066	0.252	1

Table 4-2 – Mixing rule coefficients for different PSD in numerical experiment #07
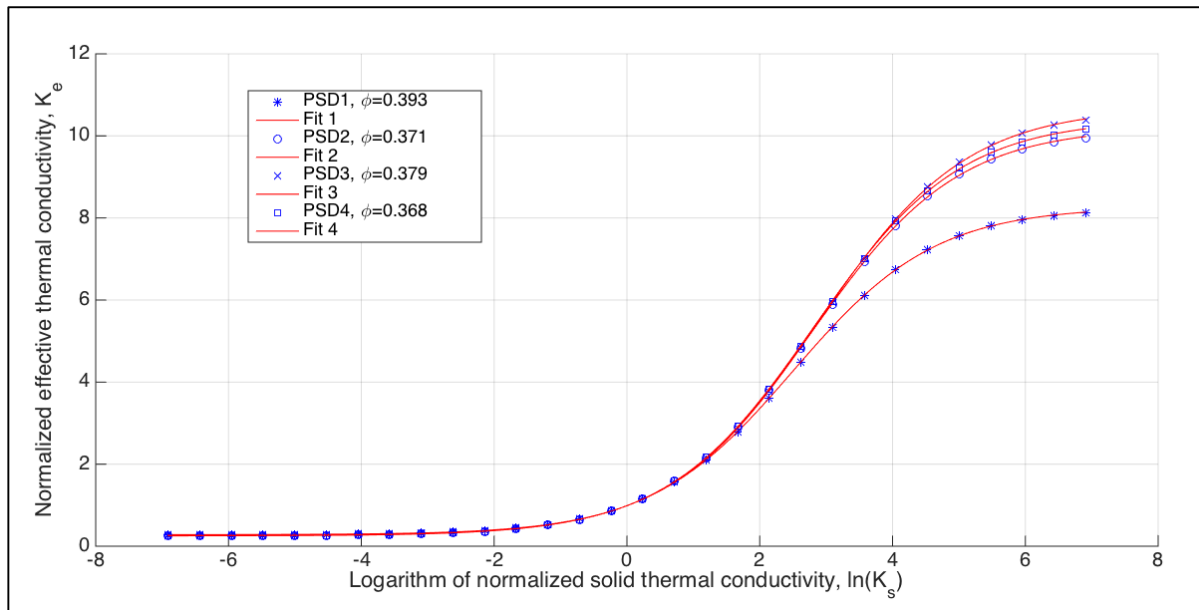
Figure 4-11 – Mixing rules for different particle size distributions

From Table 4-2 one can notice that the coefficient of determination, which shows the goodness of fit, is equal to 1 for all four different porous patterns. It means that the proposed mixing rule equation 4.1 works for porous media with different particle size distributions.

With the optimal number of grains (2000) in each porous pattern and the lowest target porosity one can conclude that the values of porosity presented in Table 4-2 are the limiting values of porosity for a media with corresponding particle size distribution.

Figure 4-11 shows that PSD1 predicts significantly different values of effective thermal conductivity, while PSD2-PSD4 predict values that are very close. In order to investigate that this result is appropriate one more model with PSD was created. This model (PSD1_1) is another random implementation of PSD1 but with 2500 grains and target porosity of 0.2. The mixing rule for the created model (PSD1_1) along with the mixing rule for PSD1 model are presented in Figure 4-12. From the graph one can see that the mixing rule is reproducible. By comparing the coefficient of mixing rules for PSD1 and PSD1_1 models (see Table 4-3) one can conclude that the mixing rules are the same. The maximum deviation between the two mixing rules is 0.8%. The fact that limiting porosity is the same for PSD1_1 pattern with 2500 grains gives more confidence in the resulting mixing rule for PSD1.
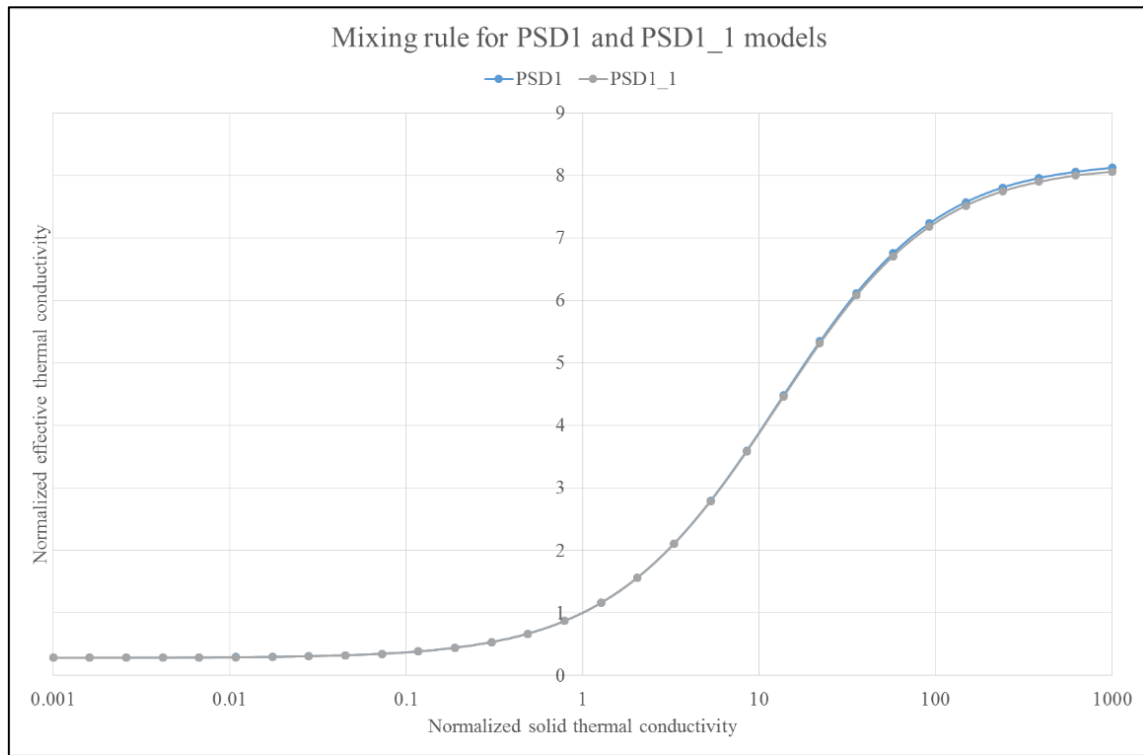
Figure 4-12 – Mixing rule for PSD1 and PSD1_1 models

	Porosity	a	b	c	d	R^2
PSD1	0.393	0.7766	0.09719	0.9311	0.2803	1
PSD1_1	0.393	0.7788	0.09823	0.9299	0.2793	1

Table 4-3 – Mixing rule coefficients for PSD1 and PSD1_1 models

One of the main conclusions of the numerical experiment #07 is that any porous media with a particle size distribution requires its own custom generated mixing rule for effective thermal conductivity prediction. PSD2 and PSD1 from the experiment are similar in terms of shapes with a small shift (see Figure 4-10), but results in different mixing rules; while PSD2 and PSD4 has similar shapes with a large shift, but results in mixing rules that are very close in terms of prediction effective thermal conductivity.

For sand saturated with water the solid to fluid thermal conductivity ratio is around 10, for sand saturated with oil it is around 40 and for sand saturated with air it is around 240. Taking natural logarithm we obtain 2.3, 3.7 and 5.5 respectively. So for real oil sands the working range of solid to fluid thermal conductivity ratio for mixing rule is from 2.3 to 5.5. From Figure 4-11 one can

see that if we incorrectly apply the mixing rule, the error in effective thermal conductivity prediction is in range from 8% to 20% (the difference between PSD1 mixing rule and PSD3 mixing rule at logarithm of normalized solid thermal conductivity from 2.3 to 5.5). This shows that the "one size fits all" approach can lead to errors up to 20% in predicting the effective thermal conductivity of oil sands using mixing rules.

One of the questions that immediately arise is: should one create a mixing rule for all particle size distributions? The answer for this question is hiding in the time for creating a custom mixing rule. The average time of creating one porous pattern is around 2 hours of computer time. The average time of creating the model is around 30 minutes of computer time. The average time for running the model is around 2 hours. To be on a safe side the total time for generating mixing rule for one particle size distribution is around 5 hours. This task can be run in parallel on computers with large number of cores and memory and it means that with enough computer power the time for mixing rule generation can be reduced by an order of magnitude.

4.3 Physical meaning of the coefficients of mixing rule

In order to understand the meaning of the coefficients of proposed mixing rule 4.1 one need to look at the limiting relations for mixing rules described in Chapter 2.

When the solid to fluid thermal conductivity ratio (K_s) approaches one the normalized effective thermal conductivity (K_e) must approach one, which means that if solid and fluid thermal conductivity are the same, then the effective thermal conductivity of porous media is equal to that of fluid or solid. For the case of mixing rule 4.1 the limit of K_e when K_s approaches 1 is:

$$\lim_{K_s \to 1} \left(\frac{a}{b + e^{-c \ln K_s}} + d \right) = \frac{a}{b + 1} + d \qquad \textbf{4.2}$$

and finally we obtain:

$$\frac{a}{b + 1} + d = 1 \qquad \textbf{4.3}$$

In Table 4-4 the limit 4.2 is calculated for the mixing rules PSD1-PSD4 and PSD1_1. One can see that for all of the mixing rules from numerical experiment #06 the limiting relation 4.3 is valid, although there is a minor deviation from 1.

Mixing rule	a/(b+1)+d
PSD1	0.988
PSD2	0.987
PSD3	0.985
PSD4	0.989
PSD1_1	0.988

Table 4-4 – Limit of mixing rules PSD1-PSD4 and PSD1_1 when K_s approaches 1

In order to improve the mixing rule equation 4.1 one can use the limiting relation 4.3 and express coefficient d in terms of a and b and substitute into equation 4.1. It results in the following equation for the mixing rule proposed in this thesis:

$$K_e = \frac{a}{b + e^{-c \ln K_s}} + 1 - \frac{a}{b + 1} \qquad \textbf{4.4}$$

In the case of model 4.4 the limiting relation 4.3 becomes exact for any mixing rule generated. Also the number of unknown parameters is reduced by one.

Another limiting relation is when the solid to fluid ratio (K_s) approaches infinity. It happens when either the fluid thermal conductivity approaches zero or the solid thermal conductivity approaches infinity. Since both thermal conductivities are positive values, the infinity has positive sign. In this case the normalized effective thermal conductivity approaches:

$$\lim_{K_s \to \infty} \frac{a}{b + e^{-c \ln K_s}} + d = \frac{a}{b} + d \qquad \textbf{4.5}$$

and by applying 4.3 we finally obtain:

$$\lim_{K_s \to \infty} \frac{a}{b + e^{-c \ln K_s}} + d = 1 + \frac{a}{b(b + 1)} \qquad \textbf{4.6}$$

In the Table 4-5 the limit 4.6 is calculated for the mixing rules from numerical experiment #07. The calculated limit agrees well with the normalized effective thermal conductivity of porous patterns at the solid to fluid thermal conductivity ratio of 1000.

Mixing rule	$a/b + d$	$K_e(K_s = 1000)$
PSD1	8.27	8.12
PSD2	10.22	9.95
PSD3	10.69	10.38
PSD4	10.41	10.16
PSD1_1	8.21	8.06

Table 4-5 – Limit of mixing rules PSD1-PSD4 and PSD1_1 when K_s approaches infinity

Finally one need to look at the case of solid to fluid ratio approaching 0. It happens when either solid thermal conductivity approaches 0 or fluid thermal conductivity approached infinity. In this case the normalized effective thermal conductivity approaches:

$$\lim_{K_s \to 0} \left(\frac{a}{b + e^{-c \ln K_s}} + d \right) = d \qquad \textbf{4.7}$$

In Table 4-6 the limit 4.7 is calculated for the mixing rules from numerical experiment #07. The calculated limit is in good agreement with the normalized effective thermal conductivity of porous patterns at the solid to fluid thermal conductivity ratio of 0.001.

Mixing rule	d	$K_e(K_s = 0.001)$
PSD1	0.2803	0.2802
PSD2	0.2557	0.2565
PSD3	0.2578	0.2580
PSD4	0.252	0.2538
PSD1_1	0.2793	0.2794

Table 4-6 - Limit of mixing rules PSD1-PSD4 and PSD1_1 when K_s approaches 0

From equation 4.7 one can see that coefficient d in the equation 4.1 is defined as the effective thermal conductivity of porous media with a given particle size distribution when the solid to fluid thermal conductivity ratio approaches 0, or in other words when the fluid phase is much more conductive than solid phase. Thus coefficient d can be obtained with good accuracy through the running heat transfer model for a porous pattern at low solid to fluid thermal conductivity ratio. The ratio $\frac{a}{b}$ can be obtained as the difference of equations 4.5 and 4.7, thus $\frac{a}{b}$ is defined as the step between the lowest possible (d) and the highest possible ($\frac{a}{b} + d$) normalized effective thermal conductivity of a porous media with a given particle size distribution. The ratio $\frac{a}{b}$ can be obtained with good accuracy by running the heat transfer model at two solid to fluid thermal conductivity ratios (highest and lowest) and taking the difference between the resulting normalized effective thermal conductivities. Since a, b and d are connected through relation 4.3 and with b and $\frac{a}{b}$ defined as mentioned above, one can calculate a and b by solving system of equations. The coefficients a and b can be found from d and $\frac{a}{b}$ as follows:

$$a = \frac{1}{\frac{1}{1-d} + \frac{1}{\frac{a}{b}}} \qquad\qquad \textbf{4.8}$$

$$b = \frac{1}{1 + \frac{a}{b} \cdot \frac{1}{1-d}} \qquad\qquad \textbf{4.9}$$

The coefficient c is the last one that should be determined. After substitution of $\ln(K_s)$ with x in equation 4.1 we get:

$$K_e = \frac{a}{b + e^{-cx}} + d \qquad\qquad \textbf{4.10}$$

The first two derivatives of 4.10 with respect to x are as follows:

$$\frac{dK_e}{dx} = \frac{ace^{-cx}}{(b + e^{-cx})^2}$$

4.11

$$\frac{d^2K_e}{dx^2} = \frac{ac^2e^{-cx}(e^{-cx} - b)}{(b + e^{-cx})^3}$$

4.12

Solving the equation $\frac{d^2K_e}{dx^2} = 0$ we obtain

$$x = -\frac{\ln b}{c}$$

4.13

For $x < -\frac{\ln b}{c}$ the value of second derivative 4.12 is more than 0 and for $x > -\frac{\ln b}{c}$ it is less than 0, which means that point 4.13 is the point of inflection of the graph of the function $K_e(x)$, where x is $\ln K_s$ (see Figure 4-13). This in turn means that coefficient c of proposed mixing defines the point of inflection of the graph in Figure 4-4. It also should be mentioned that in point 4.13 the derivative 4.11 reaches its maximum value (see Figure 4-13). The derivative 4.11 defines the rate of change of the effective thermal conductivity of porous media with respect to change in natural logarithm of solid to fluid thermal conductivity ratio. Up to the point $-\frac{\ln b}{c}$ this rate of change increases and after the point $-\frac{\ln b}{c}$ it decreases, which means that the effective thermal conductivity changes rapidly up to the point $-\frac{\ln b}{c}$ and after that point the effective thermal conductivity changes slowly until it reaches its maximum possible value of $\frac{a}{b} + d$. So the coefficient c determines the value of solid to fluid thermal conductivity ratio at which this change in growth of effective thermal conductivity happens.
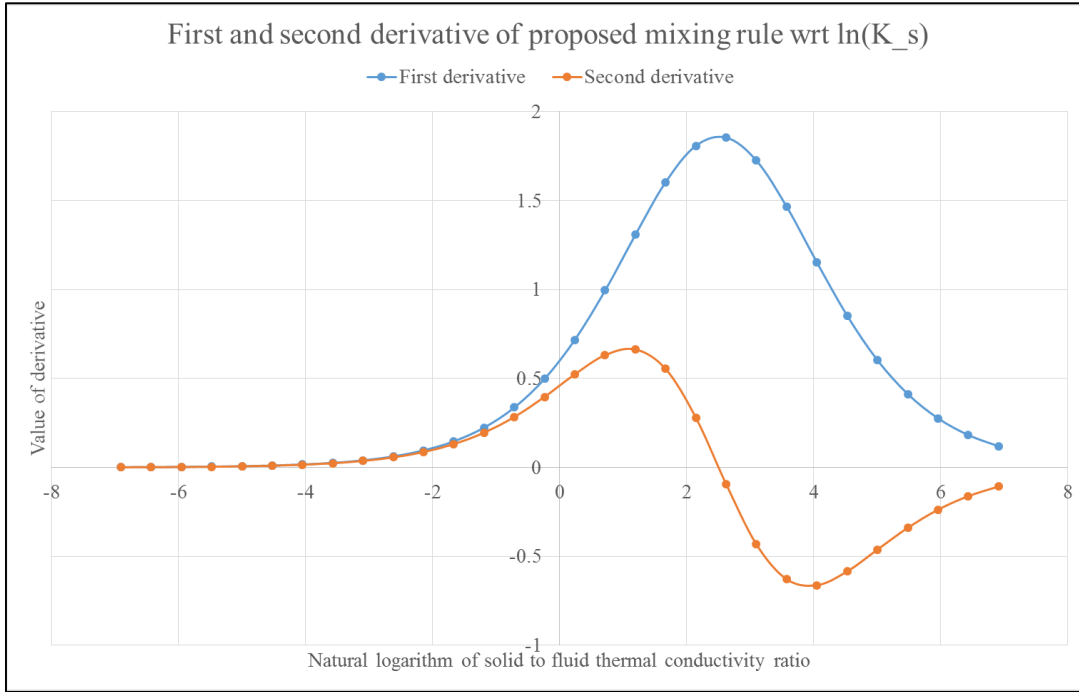
Figure 4-13 – First and second derivative of proposed mixing rule with respect to $ln(K_s)$

Since the point of inflection of the effective thermal conductivity with respect to logarithm of solid to fluid thermal conductivity ratio is defined by the structure of porous media (or the underlying particle size distribution in our case), it is not possible to predict this point without knowing the coefficient c of the mixing rule equation 4.1. But if we notice that at $x = \ln K_s = 0$ the first derivative 4.11 takes the value of $\frac{ac}{(b+1)^2}$, then we can find the c through known coefficient a and b and the value of derivative 4.11 in the point $x = 0$. At $x = 0$ the solid to fluid thermal conductivity ratio K_s is equal to 1. Coefficients a and b are calculated as described above. The only problem is to determine the value of derivative 4.11 near the point of equality of solid and fluid thermal conductivities. It can be done numerically by running two heat transfer models: one with $\ln K_s = 1 - \Delta x$ and another with $\ln K_s = 1 + \Delta x$, where Δx is a small number. Then the first derivative can be calculated as follows:

$$\left.\frac{dK_e}{dx}\right|_{x=1} \approx \frac{K_e(1 + \Delta x) - K_e(1 - \Delta x)}{2\Delta x} \qquad \textbf{4.14}$$

And finally the coefficient c can be calculated as:

$$c = \left.\frac{dK_e}{dx}\right|_{x=1} \cdot \frac{(b + 1)^2}{a} \qquad \textbf{4.15}$$

The above equation provides another meaning for the coefficient c. It affects the rate of change of the effective thermal conductivity near the point of equal thermal conductivities of solid and fluid phases. The larger the c the larger the rate of change and vice versa. In Table 4-7 the coefficient c is calculated in two ways: using the approach described above and by fitting numerical data as described at the beginning of this chapter. The agreement is good. The reason for the difference in the values of c calculated with two different methods is due to the value of Δx which in this case was 0.238.

Mixing rule	Inflection point	Numerically calculated derivative at x=0	c estimated from derivative at x=0	c calculated by fitting numerical data
PSD1	2.50	0.609	0.9444	0.9311
PSD2	2.79	0.631	0.9309	0.9082
PSD3	2.89	0.623	0.9201	0.8969
PSD4	2.81	0.635	0.9283	0.9066
PSD1_1	2.50	0.609	0.9433	0.9299

Table 4-7 – Coefficient c for mixing rules PSD1 to PSD4 and PSD1_1

Finally it should be mentioned that since there is a single point of contact between the touching grains in the generated porous patterns and the grains are of spherical shape, fluid phase is continuous and solid phase is considered dispersed for heat transfer purposes. According to the limiting relations of Chapter 2 the proposed mixing rule fulfills the limiting relations 3, 4a, 5b, 6a and 7b. The values of corresponding limits are presented in Table 4-8.

Limit	$k_s \to k_f$	$k_f \to \infty$	$k_s \to \infty$	$k_f \to 0$	$k_s \to 0$
$k_e = k_f \left(\dfrac{a}{b + e^{-c \ln \frac{k_s}{k_f}}} + d \right)$	k_f	∞	$k_f \left(d + \dfrac{a}{b} \right)$	0	$k_f d$

Table 4-8 – Limiting relations for the proposed mixing rules

As a conclusion for this subsection the following statements should be highlighted once again:

- The coefficient d of the proposed mixing rule has the meaning of the effective thermal conductivity of the porous pattern with non-conductive solid phase.

- The ratio $\frac{a}{b}$ of the proposed mixing rule has the meaning of the step in change of the effective thermal conductivity when solid phase changes from non-conductive to highly conductive.
- The coefficient c of the proposed mixing rule determines the rate of change in the effective thermal conductivity with respect to change in solid to fluid thermal conductivity ratio.
- The coefficients a, b and d are interdependent, thus only two of them need to be determined.
- "Quick look" numerical methods for estimation of all the coefficient of the proposed mixing rule were developed.

4.4 Application of the proposed mixing rule

The application of the mixing rule for a real porous medium is fairly simple. For a given particle size distribution the custom mixing rule in the form of equation 4.1 is generated by defining all the coefficient of the mixing rule from numerical modelling described at the beginning of this chapter. The following information is used as an input: water saturation (S_w), oil saturation (S_o), gas saturation (S_g), thermal conductivity of solid (k_s), thermal conductivity of water (k_w), thermal conductivity of oil (k_o) and thermal conductivity of gas (k_g). Effective thermal conductivity of porous media fully saturated with either water, oil or gas is calculated as

$$k_e^i = \frac{a}{b + e^{-c \ln k_s/k_i}}$$
4.16

where i is w for water, o for oil and g for gas. The overall effective thermal conductivity of the porous media then can be calculated using linear interpolation:

$$k_e = S_w k_e^w + S_o k_e^o + S_g k_e^g$$
4.17

Linear interpolation was used as an example. Generally speaking another mixing rule has to be applied to calculate the effective thermal conductivity of porous media saturated with oil, water and gas simultaneously.

4.5 Comparison of the novel mixing rule to other mixing rules

In this section the proposed mixing rule is compared to the mixing rules available in literature. For this purposes mixing rule developed above for PSD1 is compared to the mixing rules described in the Chapter 2: Parallel model, Series model, Geometric Mean model, Maxwell models, Kunii-Smith model, Krupiczka model, Zehner-Schlunder model, Woodside-Messmer model and the EMT model. The porosity of the porous pattern PSD1 is 0.393. This value is used for the literature value models. The solid to fluid thermal conductivity ratio changes from 10^{-3} to 10^3. For convenience the term sigmoid mixing rule or Sigmoid model will be used later in the text to indicate the novel mixing rules developed in this thesis. The term Sigmoid is due to the name of the class of functions defined by the equation 4.1.

It also should be highlighted that comparison of the prediction by other mixing rules to the Sigmoid mixing rule prediction are based on results of numerical experimental data. Since the Sigmoid mixing rule approximates numerical experimental data with $R^2 = 1$ the values predicted by the Sigmoid model will be used as the basis for comparison. The main region of interest for comparison of mixing rules is $K_s \in [10,100]$. This region of interest contains solid to fluid thermal conductivity ratios corresponding for sand and water, oil and gas.

In Figure 4-14 the effective thermal conductivity predictions by the Sigmoid rule are compared to that of Parallel model, Series model and Geometric Mean model. The limits when K_s approaches 1, infinity and zero corresponds to the cases of equal solid and fluid phases thermal conductivities, solid is highly conductive in comparison with fluid phase and solid is highly non-conductive in comparison with fluid phase respectively. The value of limits for Sigmoid, Parallel, Series and Geometric Mean models are presented in Table 4-9. From Figure 4-14 and Table 4-9 one can find that all of the mixing rules go through the point (1,1) which means that if the thermal conductivities of phases are equal, the resulting effective thermal conductivity is the same as thermal conductivity of phases. When solid phase becomes highly conductive predictions by Parallel and Geometric Mean models approach infinity and show overestimation of the effective thermal conductivity in the region of interest; Series model prediction approaches a finite value and show underestimation. When solid phase becomes highly non-conductive predictions by Series and Geometric Mean models approach zero and show underestimation of

the effective thermal conductivity; Parallel model prediction approaches finite value, but shows overestimation.

Model	$K_s \to 1$	$K_s \to \infty$	$K_s \to 0$
Sigmoid	1	d	$\left(d + \dfrac{a}{b}\right)$
Parallel	1	∞	ϕ
Series	1	$\dfrac{1}{\phi}$	0
Geometric Mean	1	∞	0

Table 4-9 – Limits for Sigmoid, Parallel, Series and Geometric Mean models

In Figure 4-15 the effective thermal conductivity predictions by the Sigmoid rule are compared to that of the Maxwell models. The limit values for the Sigmoid, Maxwell-1 and Maxwell-2 models are presented in Table 4-10. From Figure 4-15 and Table 4-10 one can find that all of the mixing rules go through the point (1, 1), which again means that if the thermal conductivities of phases are equal, the resulting effective thermal conductivity is the same as thermal conductivity of phases. When solid phase becomes highly conductive predictions by the Maxwell-2 model approaches infinity and shows overestimation of the effective thermal conductivity in the region of interest; the Maxwell-1 model prediction approaches a finite value and shows underestimation in the region of interest. When solid phase becomes highly non-conductive prediction by the Maxwell-2 model approaches zero and shows underestimation of the effective thermal conductivity; the Maxwell-1 model prediction approaches finite value and shows very close values to that of Sigmoid model.

Model	$K_s \to 1$	$K_s \to \infty$	$K_s \to 0$
Sigmoid	1	d	$\left(d + \dfrac{a}{b}\right)$
Maxwell-1	1	$\dfrac{3 - 2\phi}{\phi}$	$\dfrac{2\phi}{3 - \phi}$
Maxwell-2	1	∞	0

Table 4-10 – Limits for Sigmoid and Maxwell models

In Figure 4-16 the effective thermal conductivity predictions by the Sigmoid rule are compared to that of Kunii-Smith and Krupiczka models. The value of limits for Sigmoid, Kunii-Smith and Krupiczka models are presented in Table 4-11. From Figure 4-16 and Table 4-11 one can find that all of the mixing rules go through the point (1, 1). When solid phase becomes highly conductive predictions by the Kunii-Smith and Krupiczka models track each other in the region of interest. Both of them intersect Sigmoid model at around $K_s = 35$; before this value both models slightly underestimate, while after both models slightly overestimate the effective thermal conductivity of porous pattern in the region of interest. The Krupiczka model was developed as a correlation to analytical solution in order to become easy applicable. Because of this artificial nature this model approaches 0 when $K_s \to \infty$, but in the region of interest its value increases (see Figure 4-16). When the solid phase becomes highly non-conductive prediction by the Krupiczka model approaches zero and shows underestimation of the effective thermal conductivity; the Kunii-Smith model prediction approaches finite value and shows overestimation.

Model	$K_s \to 1$	$K_s \to \infty$	$K_s \to 0$
Sigmoid	1	d	$\left(d + \dfrac{a}{b}\right)$
Kunii-Smith	1	$sign(\phi - 0.2) \cdot \infty$	ϕ
Krupiczka	1	0	0

Table 4-11 – Limits for Sigmoid, Kunii-Smith and Krupiczka models

In Figure 4-17 the effective thermal conductivity predictions by the Sigmoid rule are compared to that of Zehner-Schlunder, Woodside-Messmer and Effective Medium Theory (EMT) models. The value of limits for Sigmoid, Zehner-Schlunder, Woodside-Messmer and EMT models are presented in Table 4-12. From Figure 4-17 and Table 4-12 one can find that all of the mixing rules go through the point (1, 1). When solid phase becomes highly conductive prediction by EMT model approaches infinity and overestimates the effective thermal conductivity in the region of interest; the Zehner-Schlunder model approaches infinity as well but in the region of interest the prediction is in good agreement with Sigmoid model with only deviation after $K_s = 50$; the Woodside-Messmer model approaches finite value and overestimates the prediction of effective thermal conductivity in the region of interest. When the solid phase becomes highly

non-conductive predictions by Zehner-Schunder, Woodside-Messmer and EMT models approach finite but different values. Zehner-Schlunder and EMT models show underestimation, while Woodside-Messmer model shows overestimation.

Model	$K_s \to 1$	$K_s \to \infty$	$K_s \to 0$
Sigmoid	1	d	$\left(d + \dfrac{a}{b}\right)$
Zehner-Schlunder	1	∞	$1 - \sqrt{1 - \phi}$
Woodside-Messmer	1	$\dfrac{100}{3}\phi^2 - \dfrac{203}{3}\phi + \dfrac{106}{3}$	$\phi - 0.03$
EMT	1	∞	$\dfrac{1}{4}|3\phi - 1| + \dfrac{3}{4}\phi - \dfrac{1}{4}$

Table 4-12 – Limits for Sigmoid, Zehner-Schlunder, Woodside-Messmer and EMT models
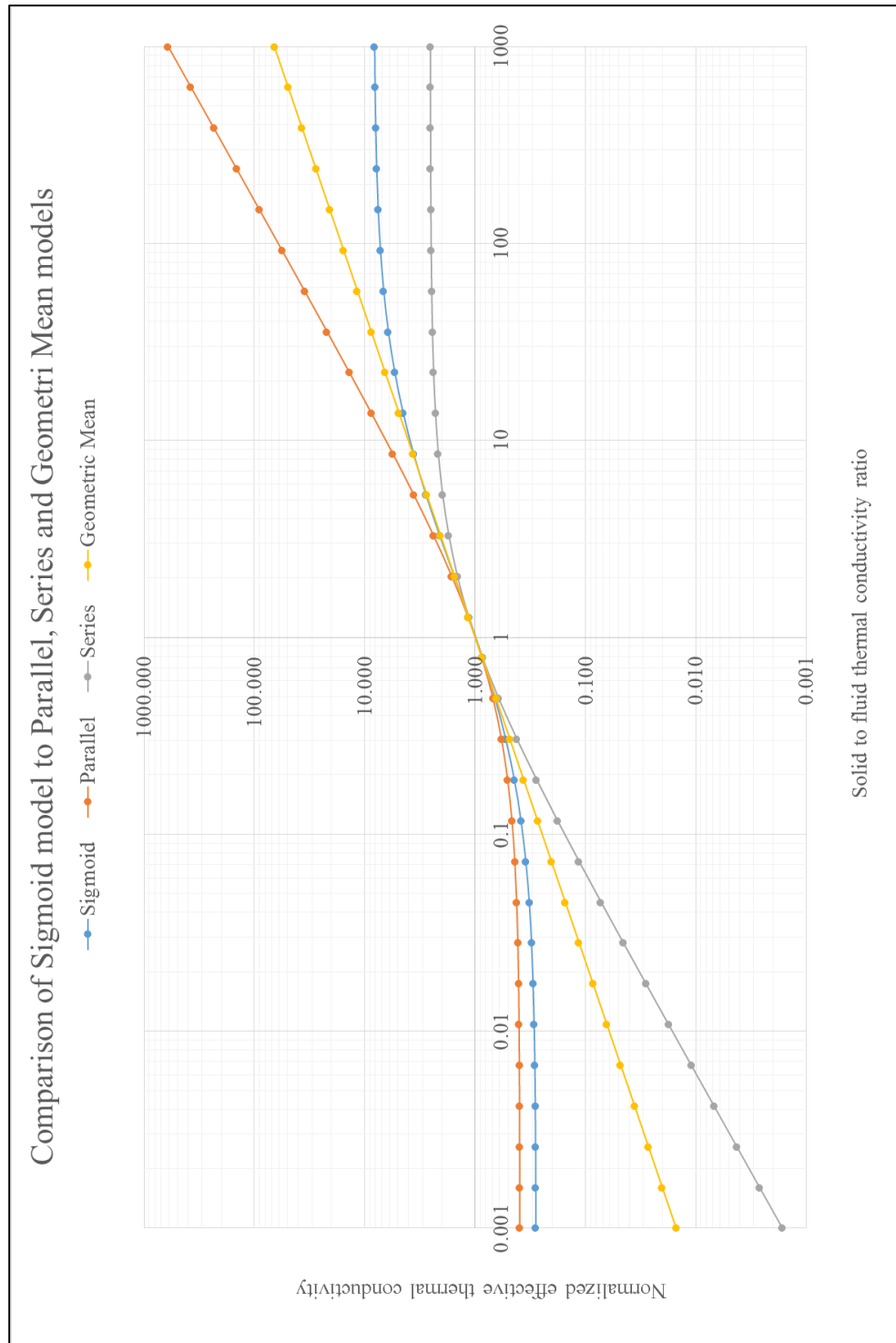
Figure 4-14 – Comparison of sigmoid model to Parallel, Series, and Geometric Mean models
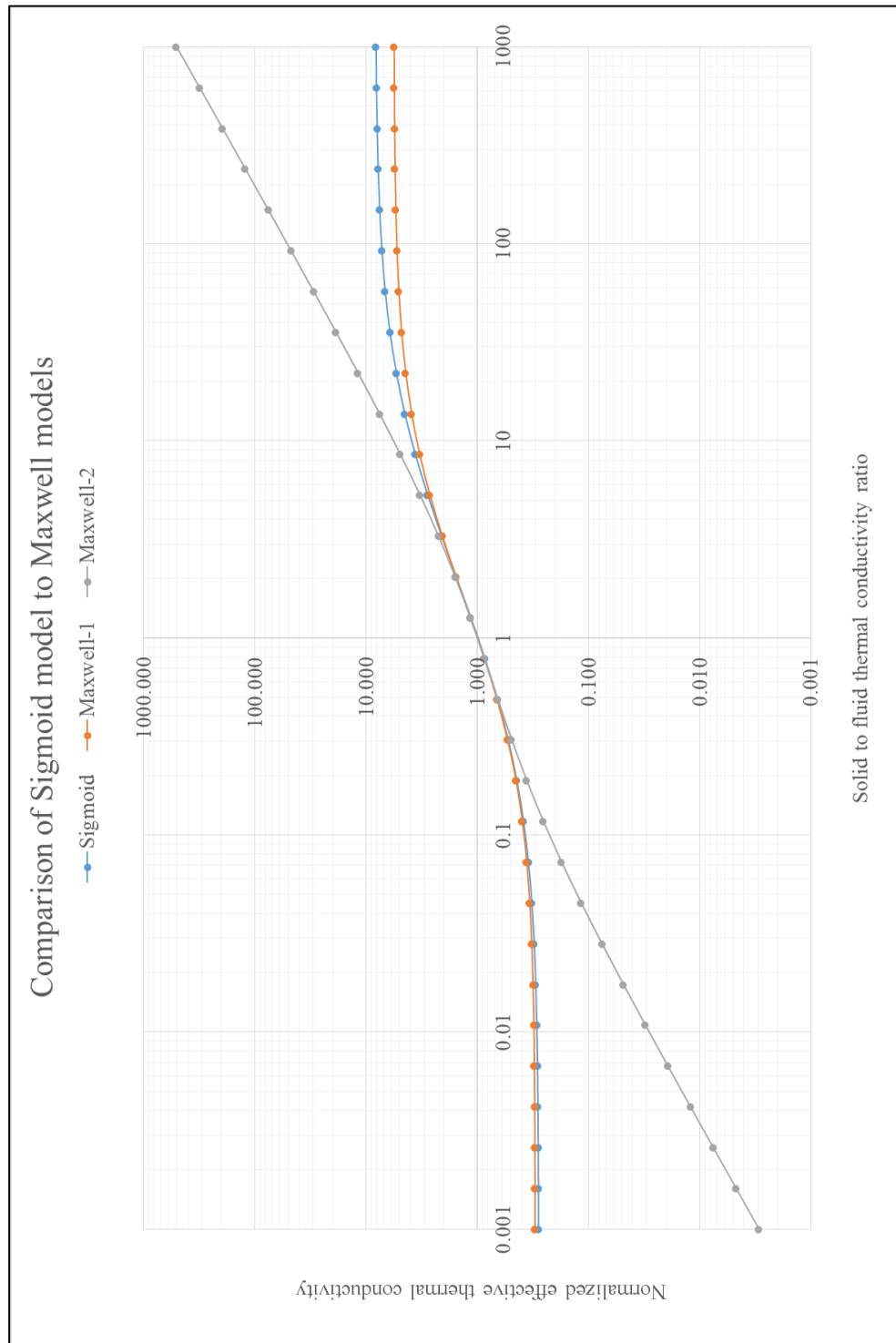
Figure 4-15 – Comparison of Sigmoid model to Maxwell-Eucken models
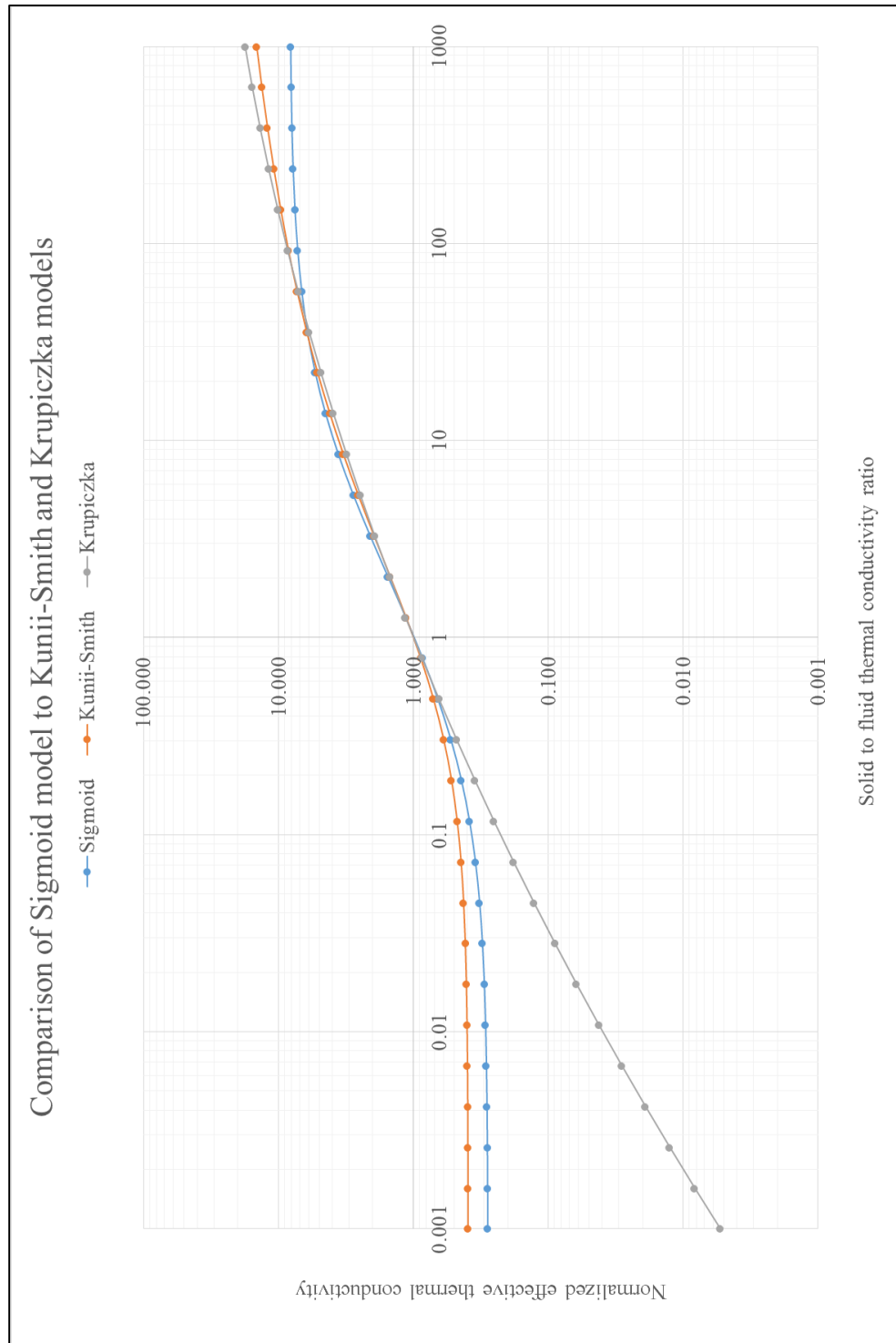
Figure 4-16 – Comparison of Sigmoid model to Kunii-Smith and Krupiczka models
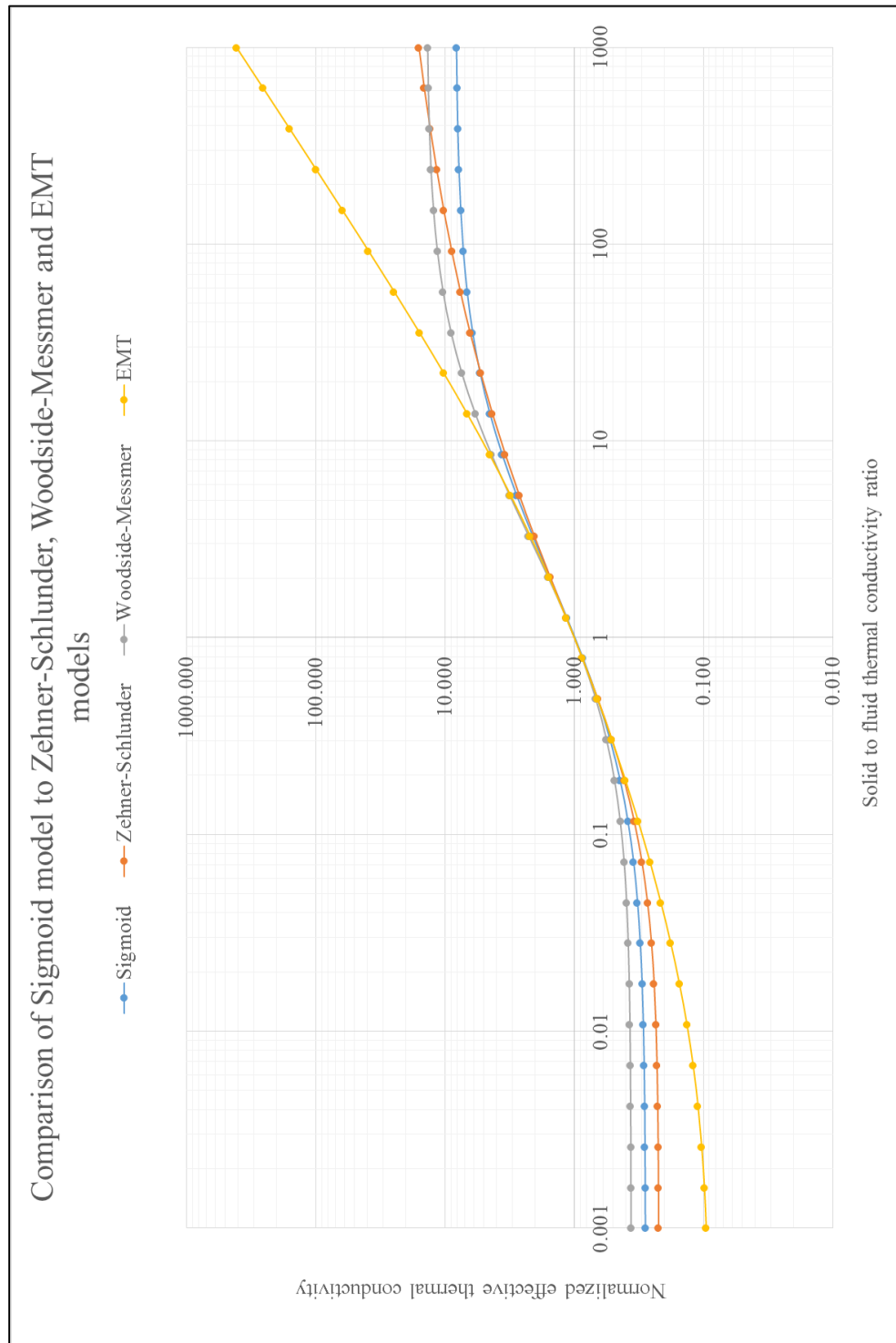
Figure 4-17 – Comparison of Sigmoid model to Zehner-Schlunder, Woodside-Messmer and EMT model

The comparison of the available in literature mixing rules to the results of numerical experiment shows that none of the available mixing rules can accurately predict the effective thermal conductivity of a porous pattern which consists of spheres from a given particle size distribution with a single point contact between the grains. The limits for mixing rules available in literature are calculated for cases of equal thermal conductivities of solid and fluid phase, for highly conductive solid and highly non-conductive solid phase. The Zehner-Schunder, Kunii-Smith and Krupiczka models are the closest in terms of prediction the effective thermal conductivity in the region of solid to fluid thermal conductivity ratios specific for unconsolidated sands saturated with water, oil and gas.

None of the mixing rules involves particle size distribution as an input parameter. However the Sigmoid mixing rule developed in this thesis does not involve porosity as an input parameter, while all of the mixing rules contains porosity as an input parameter. It considered that for a given particle size distribution the limiting porosity exists when the number of grains approaches infinity. It means that porosity is indirectly included in the Sigmoid mixing rule. Further investigation is required to include the porosity in the Sigmoid mixing rule, as the effective thermal conductivity is a strong function of porosity.

The Sigmoid mixing rule is presented by the simple formula 4.1 and is easy to use. But the determination of the coefficients of the Sigmoid mixing rule require some additional numerical modelling. The average time to calculate the coefficients of the Sigmoid mixing rule is around 4 hours if use straightforward parametric sweep modelling with respect to solid to fluid thermal conductivity ratio, but definitely the procedure can be optimized to reduce the computation time.

The Sigmoid mixing rule can be used to predict effective thermal conductivity of unconsolidated porous media saturated with either oil, water or gas. Another mixing rule should be developed to apply the Sigmoid rule to a porous media saturated with all three fluids simultaneously. The idea is to apply the heat transfer modelling at the pore scale level to a porous patterns after at a different saturations caused by modeling of three phase fluid flow in porous media. But the application of the sigmoid mixing rule is not limited to the unconsolidated sands. It potentially can be used to predict the effective thermal conductivity of packed beds and metallic foams.

Sigmoid mixing rule does not include the effect of contact area between the grains (as well as all the mentioned mixing rules from literature). This is a possible area of future research. The idea is

basically the same, but grains should have finite area of contact in-between. It will allow to generate more realistic porous patterns and as a result to generate custom mixing rules with more realistic predictions for the effective thermal conductivity of porous media.

Chapter 5: **From pore to core scale level**

In the previous chapter the question of pore scale level modelling of heat transfer was addressed. An algorithm for developing the Sigmoid mixing rule was designed. Typical size of the geometry used for the modelling (porous pattern) is of millimetre scale, while the size of grid blocks used in reservoir simulators is of metres and tens of meters scale. There are several levels of upscaling that can be distinguished in porous media (see Figure 5-1). Micro Computed-Tomography (μCT or micro CT) level range from size of micrometers to millimetres. At this scale level separate pores and grains are visible and the pore structure can be described. Core level ranges from millimetres to centimetres. At this scale level large pores and grains are visible, but mostly the porous medium is presented as homogeneous. Heterogeneity in terms of different layers can be distinguished. Well level ranges from tenth of centimetres to meters. At his level several geological layers can be distinguished within the length of the well. Grid block level ranges from metres to tenth of meters. At this level the porous media can consist of different geological formations. The main question that arises is: how one can upscale the results of pore scale modelling to core scale and up? An attempt to answer this question is described in this chapter.
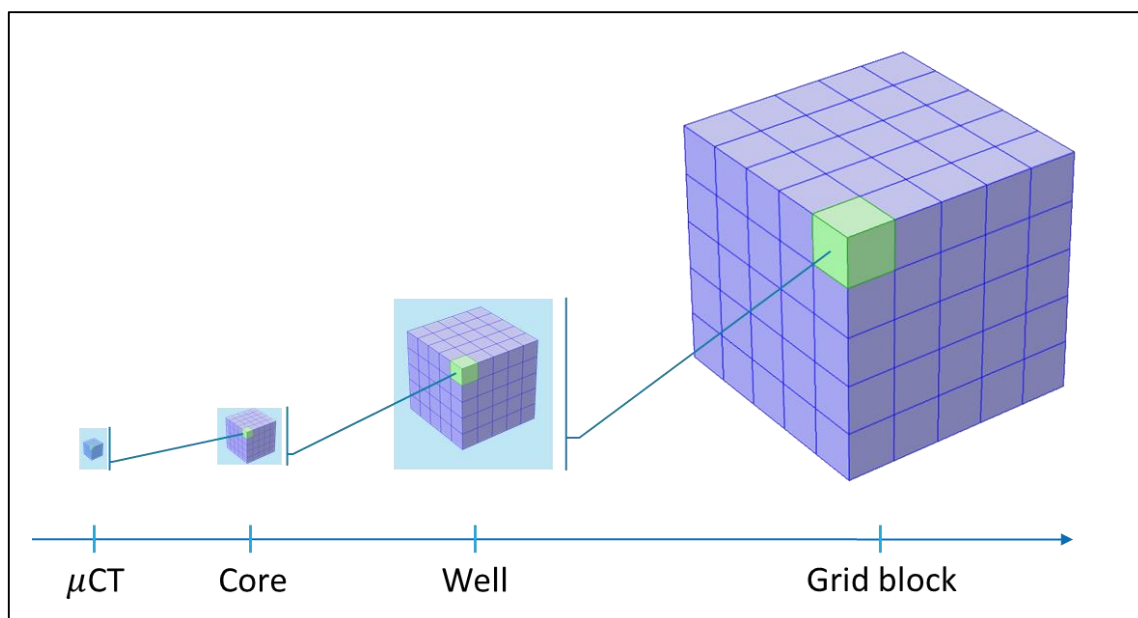
Figure 5-1 – Levels of upscaling

The first part of this chapter describes the approach of upscaling reservoir properties using a so-called network modelling, where the porous medium is substituted with an equivalent network model, which can be easily solved by applying Kirchhoff's laws. The second part of this chapter presents the model-by-model validation of the network modelling upscaling approach. In the third part of this chapter the upscaling technique which uses computed tomography images network upscaling as the basis for upscaling of reservoir properties of real cores.

5.1 Upscaling of reservoir properties: a network approach

Upscaling of reservoir properties is a problem that people are working on for decades. The equivalent electrical circuit approach described below is not new (Kantzas 1985). The upscaling approach using an equivalent network will be described for a two-dimensional case to make the explanation clearer and easier to understand, but it was implemented for three-dimensional systems. Rectangular shaped porous medium is assumed.

Firstly the porous medium is divided into blocks of rectangular shape. It is assumed that the properties of the blocks are known. In other words the larger scale porous media is constructed of smaller blocks with known properties. Looking forward it is worth mentioning that the properties of smaller blocks can be obtained through the modelling of real physics at the pore scale level.

The next step is to create an equivalent electrical circuit network that will represent the original porous media. At the centres of blocks we place nodes. Nodes that are placed in neighbouring blocks are connected with edges (bonds). So, the equivalent electrical circuit network consists of nodes and edges. Nodes are just for connection between edges, while edges has a non-zero electrical resistivity. In order for the electrical circuit network to be equivalent to the original porous media one need to calculate the equivalent electrical resistivity of the edges.

It is known that Ohm's Law of flow of electrical current through media, Darcy's Law of fluid flow through porous media and Fourier's Law of heat conduction are similar in their formulation. The flux is directly proportional to the gradient of driving forces.

Indeed, the flow of electrical current (Ohm's Law) is described by the following equation:

$$J = -\sigma \nabla \Phi \qquad \textbf{5.1}$$

where J – is the density flux of electrical current, which is directly proportional to the gradient of charge density $\nabla \Phi$ (electric field) with the coefficient of proportionality σ called electrical conductivity.

The flow of fluid (Darcy's Law) in porous media is described by the following equation:

$$u = -\lambda \nabla P \qquad \textbf{5.2}$$

where u is the velocity of the fluid (volumetric fluid flux), which directly proportional to the gradient of fluid pressure ∇P (fluid potential in general case) field with the coefficient of

proportionality λ called fluid mobility. Fluid mobility is the ratio of the porous medium permeability (to that fluid) to the fluid viscosity.

The flow of heat through media is described by the following equation:

$$q = -k\nabla T \qquad\qquad\qquad\qquad \textbf{5.3}$$

where q is the heat flux, which is directly proportional to the temperature gradient ∇T with the coefficient of proportionality k called thermal conductivity.

Thus, due to similar formulation of the underlying equations the absolute and effective permeability of the porous medium, the thermal conductivity and the electrical conductivity (electrical resistivity and formation factor) can be scaled up in a similar manner. The equivalent electrical network is chosen due to a well-developed approach of applying Kirchhoff's Law to solve the electrical circuit, i.e. to determine the equivalent resistivity of the network as if it were a single resistor.

In Figure 5-2 the approach for creating equivalent edge from blocks is presented. The idea that each block is divided into two parts and the two adjacent parts creates a new block with left side from left block and right side from right block. The equivalent property can be calculated using the series mixing rule (for the case of blocks of equal size):

$$k_{eq} = \frac{1}{\dfrac{1}{k_1} + \dfrac{1}{k_2}} \qquad\qquad\qquad\qquad \textbf{5.4}$$

where k_{eq} is the equivalent property (electrical conductivity, thermal conductivity or fluid mobility), k_1 is the property value of the left block and k_2 is the property value of the right block. By applying this approach to all the neighbouring blocks one can generate an equivalent circuit network. An example for 3x3 two-dimensional case is presented in Figure 5-3.
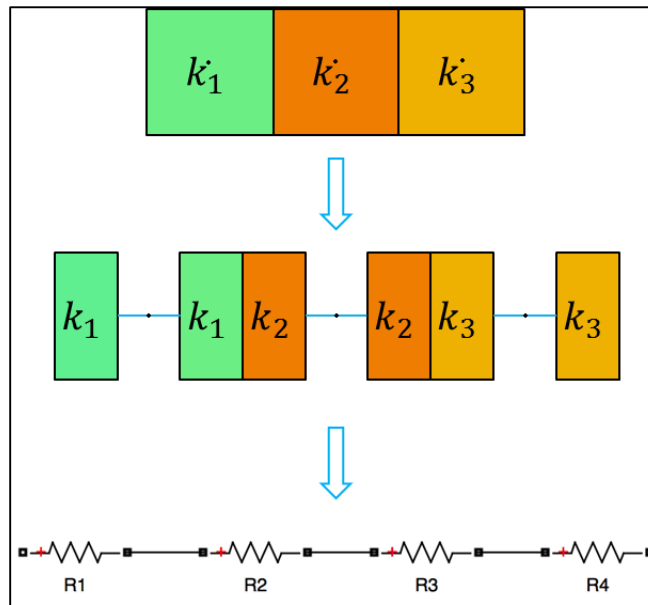
Figure 5-2 – Transformation of blocks to equivalent edges
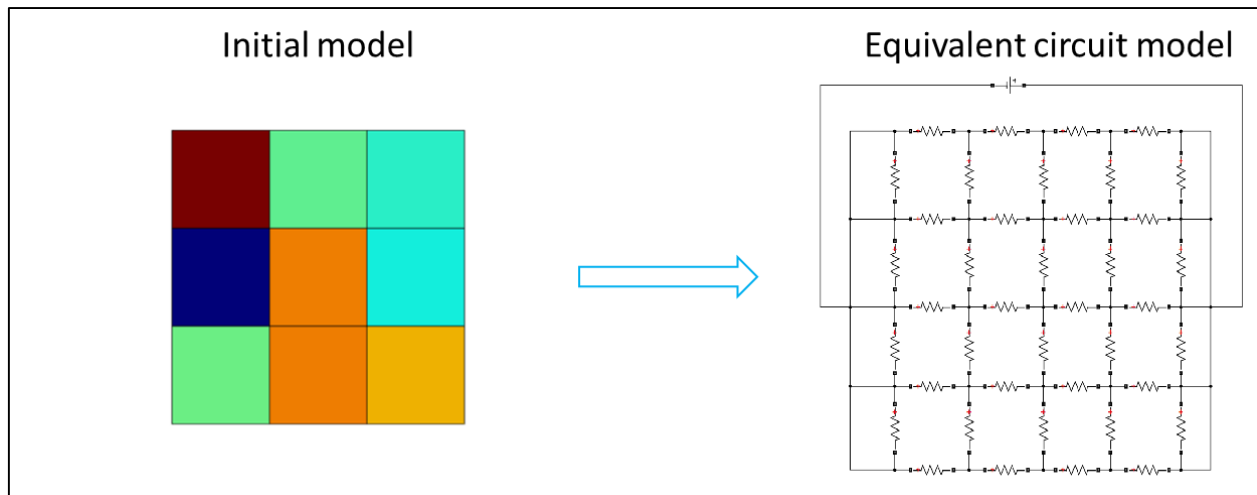
Figure 5-3 – Equivalent circuit network model

The next step is to apply Kirchhoff's Laws (Clayton 2001) to calculate the equivalent resistivity of the electrical circuit network. Kirchhoff's first law is based on the principle of conservation of electrical charge: at any node in an electrical circuit the sum of currents flowing into that node is equal to the sum of currents flowing out of that node. Kirchhoff's point rule or Kirchhoff's junction rule are the other names of the Kirchhoff's first law. Mathematically it can be described as that for any node in the electrical circuit the following equation is valid:

$$\sum_{k=1}^{n} I_k = 0 \qquad \textbf{5.5}$$

In equation 5.5 it is considered that electrical currents going into the node have positive sign and electrical currents going out of the node have negative sign.

Kirchhoff's second law is based on the principle of conservation of energy: the directed sum of the electrical potentials differences around any closed network is zero. Kirchhoff's second law is also called Kirchhoff's loop (or mesh) rule. Mathematically it can be formulated as that for any closed loop in the electrical circuit the following equation is valid:

$$\sum_{k=1}^{n} V_k = 0 \qquad \textbf{5.6}$$

In equation 5.6 it is considered that potential difference at the edge is positive if the direction of the electrical current in that edge is the same as some arbitrary (but fixed) direction chosen for the closed loop and potential difference at the edge is negative if the direction of the electrical current in that edge is the opposite to the direction chosen for the closed loop.

These two principles allow us to solve any electrical circuit, which in our case means to find the electrical resistivity of the whole electrical network as if it were a single resistor. The electric potential difference is applied to the whole circuit network as the boundary condition.

Application of the Kirchhoff's laws to the equivalent circuit network in our case leads to the following system of linear equations (in matrix form):

$$AYA^T\boldsymbol{u}_0 = -A(\boldsymbol{j} + Y\boldsymbol{e}) \qquad \textbf{5.7}$$

where A is the $(q-1) \times p$ matrix of connections, q is the number of nodes, p is the number of edges, Y is the $p \times p$ diagonal matrix of electrical conductivities of edges, $\boldsymbol{u}_0$ is the $(q-1) \times 1$ column vector of node potentials, $\boldsymbol{j}$ is the column vector of sources of electrical current in edges (if exists) and $\boldsymbol{e}$ is the $p \times 1$ column vector of sources of electromotive forces (if exists) of edges. In our case there are no sources of electrical current in edges, which means that $\boldsymbol{j}$ is zero column vector and there is only single source of electromotive forces (to create a flow of electrical current in the circuit network). An arbitrary value of one volt is assigned to this electromotive force. Which means that column vector $\boldsymbol{e}$ has only last element equal to one, while others are zero.

The matrix of connections A has the following elements a_{ij}:

$$a_{ij} = \begin{cases} 0, if\ edge\ j\ is\ not\ connected\ to\ node\ i \\ -1, if\ edge\ j\ starts\ from\ node\ i \\ 1, if\ edge\ j\ ends\ in\ node\ i \end{cases}$$ **5.8**

Finally the system of linear equations looks as follows:

$$AYA^T u_0 = -AYe$$ **5.9**

Figure 5-4 shows the structure of the matrix on the left hand side of 5.9 for the case of three dimensional network which consists of 3x3x3 nodes. The star means a non-zero matrix element, the rest of the elements are zero. This matrix is a sparse matrix. The structure of the matrix depends on the numbering system for nodes and edges of the network. The detailed description of the numbering system used in this thesis is presented in Appendices B. The solution of the system of linear equations can be calculated as follows:

$$u_0 = (AYA^T)^{-1}(-AYe)$$ **5.10**

where $(AYA^T)^{-1}$ is the inverse matrix to AYA^T.
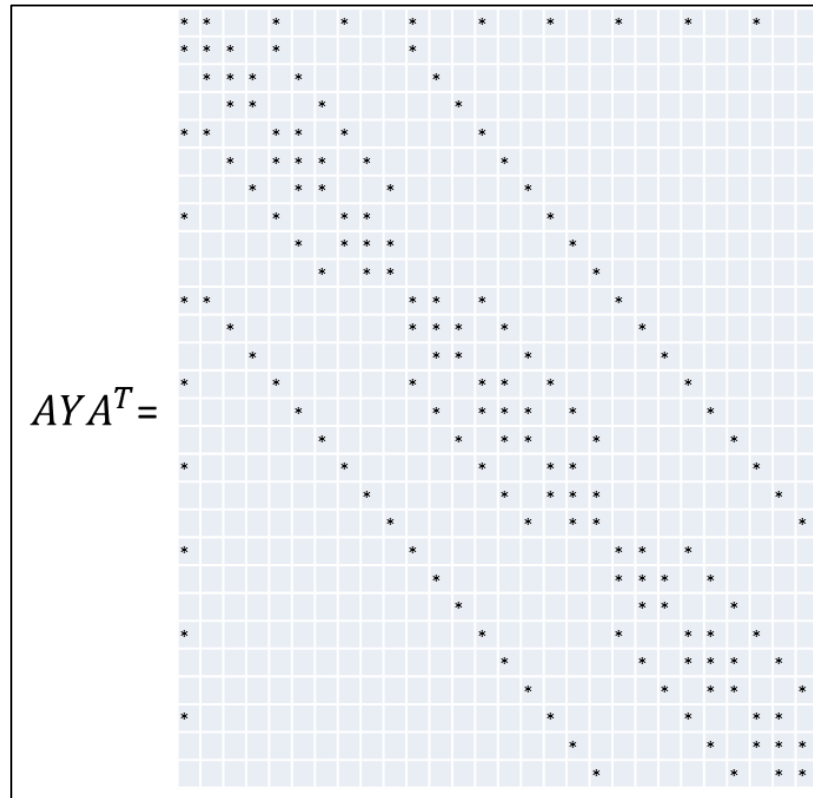
Figure 5-4 – Matrix of equivalent circuit network

The order of the matrix AYA^T significantly increases with the number of blocks in the porous media. The conjugate gradients method (Hestenes and Stiefel 1952) was developed to find the inverse matrix for the sparse matrixes of a high order. This method is one of the iterative class of methods, which does not find exact solution but rather the approximation with a specified relative tolerance. This method is considered as one of the fastest for sparse matrix inversion.

From the solution of equation 5.10 one can find the overall electrical conductivity of the whole network as the ratio of the electrical current to applied voltage (which in our case is 1V). Electrical current in the electrical circuit network can be found as a sum of the electrical currents over the edges located at the input of the network. Electrical currents for these edges can be determined from obtained solution $\boldsymbol{u}_0$ of voltage potentials and known electrical conductivities of edges. It results in the following equation:

$$Y_{eq} = \frac{I}{V} = \sum_{in} \boldsymbol{u}_{oi} Y_{ii} \qquad\qquad \textbf{5.11}$$

The resulting equivalent electrical conductivity Y_{eq} is the scaled up electrical conductivity of the porous media. Due to the similarity of the formulation of Ohm's Law, Darcy's Law and Fourier's Law the permeability and the effective thermal conductivity of porous media can be calculated using the same approach.

5.2 Numerical validation of network upscaling approach

There are two methods that can be used to validate the network upscaling approach: experimental and numerical. One of the possible experimental validations of the network upscaling approach is to conduct a set of experiments: heat transfer, fluid flow or electrical current flow. First of all the experiments should be conducted on a core sample of a cubic shape. Then the core sample need to be cut into pieces (i.e. 3x3x3) and conduct experiments on each piece separately. This will provide the input data for network upscaling approach. But 3x3x3 seems not enough for a good experimental validation. The number of experiments increase as a power of three with the number of cuts. Thus it was decided to conduct a model-by-model validation using computational software. The workflow for model-by-model validation of network upscaling approach is presented in Figure 5-5. Porous media is represented as a cube which consists of smaller cubical blocks (5x5x5). Each block is populated with the properties (permeability, formation factor and thermal conductivity) from a normal distribution with some mean and standard deviation values. The scaled up properties is then calculated using COMSOL Software with Darcy's Law, Ohm's Law and Fourier's Law with appropriate boundary conditions are used to describe physics to calculate the corresponding properties. This approach is considered more accurate than the network modeling approach, as it is direct modeling of the physics in the porous media.

The same information about properties arrangement is then feed into the network upscaling algorithm (Matlab-based program was developed for this purposes). The results of scaling up using two models are then compared.
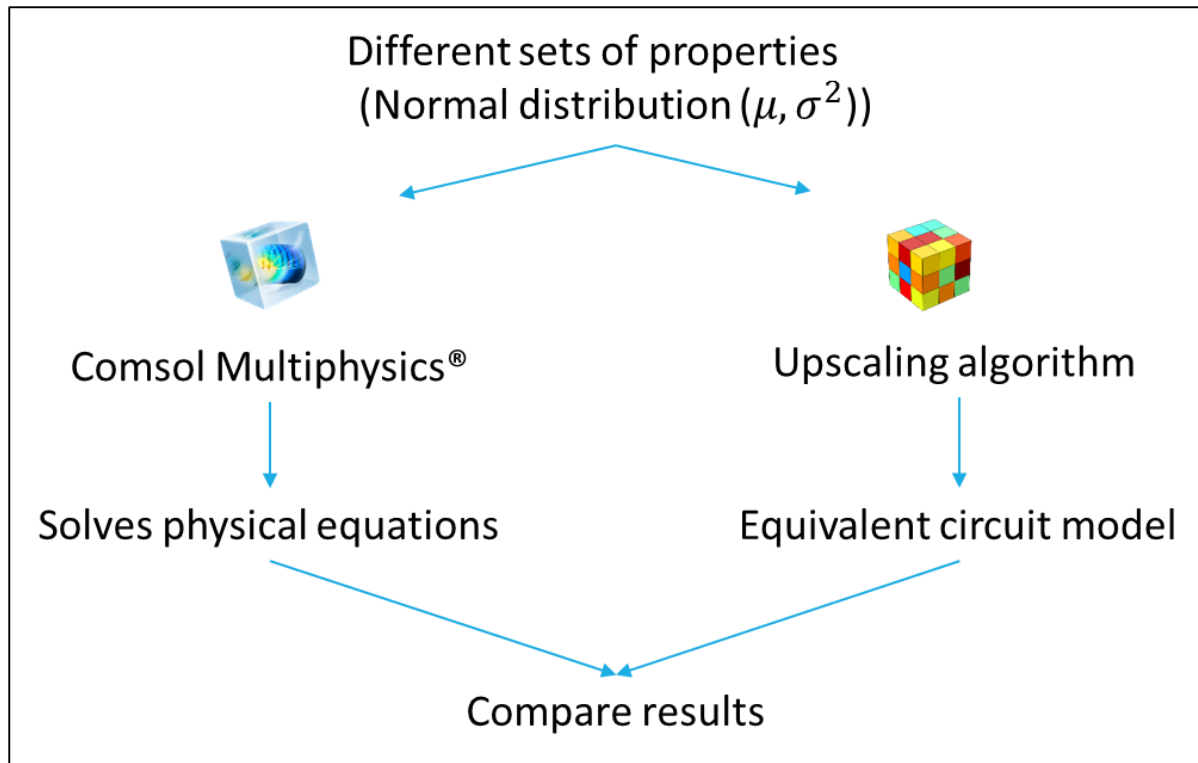
Figure 5-5 – Model-by-model validation approach

The following model-by-model validation numerical experiments were conducted for permeability upscaling with network approach:

- Mean permeability 50 mD, standard deviation of 10% of mean (5 mD)
- Mean permeability 100 mD, standard deviation of 20% of mean (20 mD)
- Mean permeability 100 mD, standard deviation of 30% of mean (30 mD)

The results of the validation are presented in Figure 5-6 (blue dots corresponds to the network upscaling approach, red dots corresponds to the direct physics modeling). Only when the model was populated with the permeability data from normal distribution with large standard deviation (30% of mean) the upscaling through direct modelling and network upscaling approach showed a difference in scaled up version of permeability. The maximum difference in the two predictions is 2.5%, which is still acceptable. For small (10% of mean) and medium (20% of mean) the scaled up permeability values are almost identical. It also should be mentioned that two graphs in Figure 5-6 track each other, which shows that two models respond in the same direction to the deviations in input data.

The sensitivity analysis to the number of blocks was also conducted. The network upscaling model was run with the same distribution of permeability data as input, but different number of block. For each number of blocks model was populated several time to see the variability. The graph in Figure 5-7 shows that variation in scaled up permeability decreases with the number of blocks increasing. With the model of 10x10x10 blocks the permeability variation can be considered negligible.
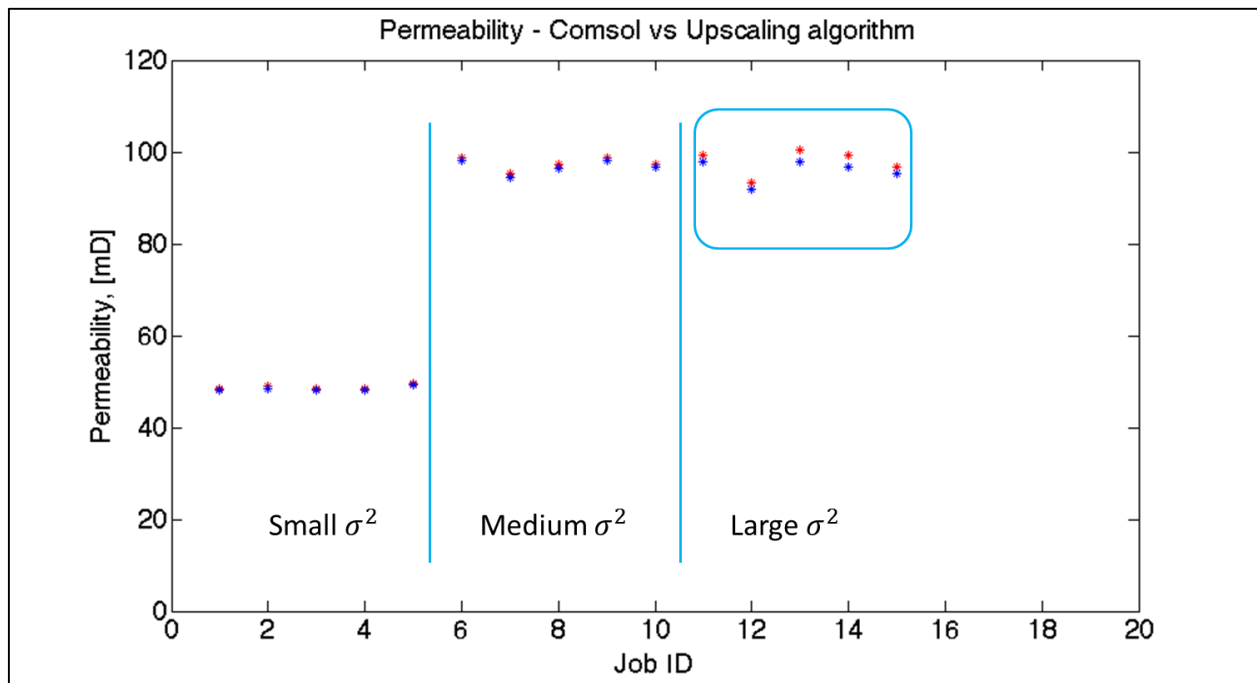
Figure 5-6 – Upscaling of permeability (model-by-model validation)
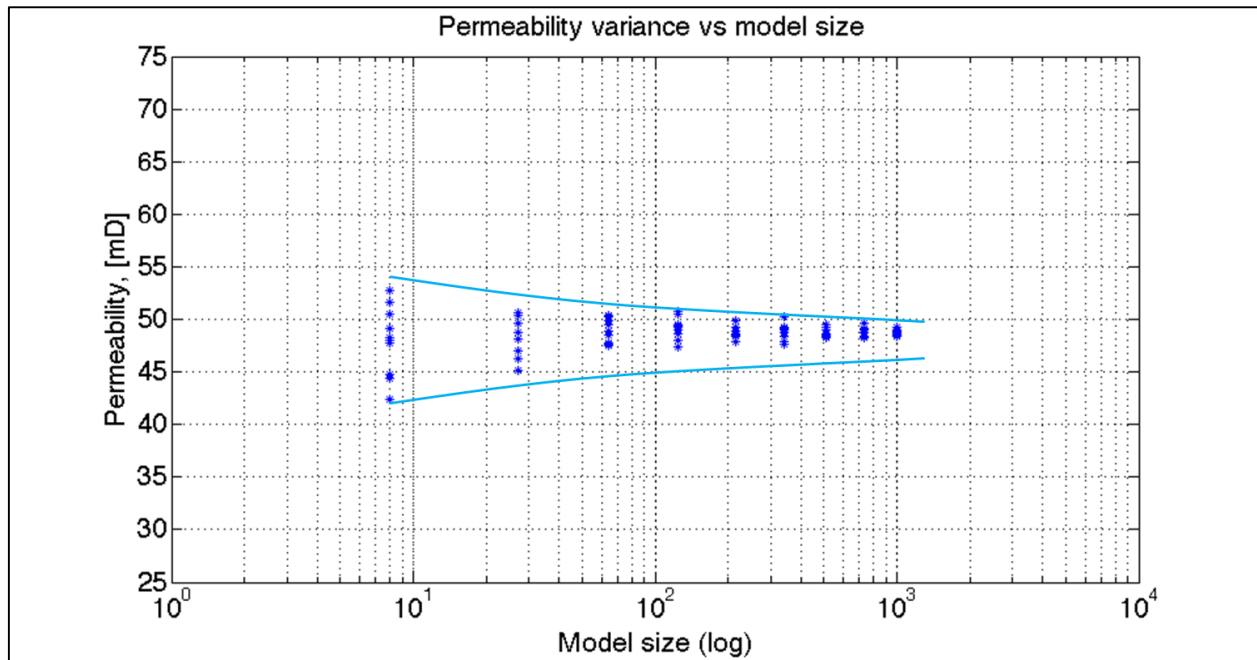
Figure 5-7 – Sensitivity of permeability to model size

The same procedure described above was conducted for the formation resistivity factor. The following parameters of normal distribution were used to populate the model:

- Mean formation factor of 75, standard deviation of 10% (7.5)

- Mean formation factor of 200, standard deviation of 20% (40)

- Mean formation factor of 175, standard deviation of 30% (52.5)

And finally the following parameters of normal distribution were used to populate the model for scaling up the thermal conductivity:

- Mean thermal conductivity of 0.15 $W/(m \cdot K)$, standard deviation of 10% (0.015)

- Mean thermal conductivity of 0.35 $W/(m \cdot K)$, standard deviation of 20% (0.07)

- Mean thermal conductivity of 0.3 $W/(m \cdot K)$, standard deviation of 30% (0.09)

The results for the scaling up of formation resistivity factor and thermal conductivity are presented in Figure 5-8 and Figure 5-9 respectively. As before blue dots correspond to the network upscaling approach and red dots corresponds to the direct physics modeling. The results are basically the same as for permeability: for standard deviation of 10-20% the scaled up version predictions by two models match each other, for standard deviation of 30% the scaled up

version predictions are off by 6.5% for thermal conductivity and are off by 5.5% for the formation resistivity factor.
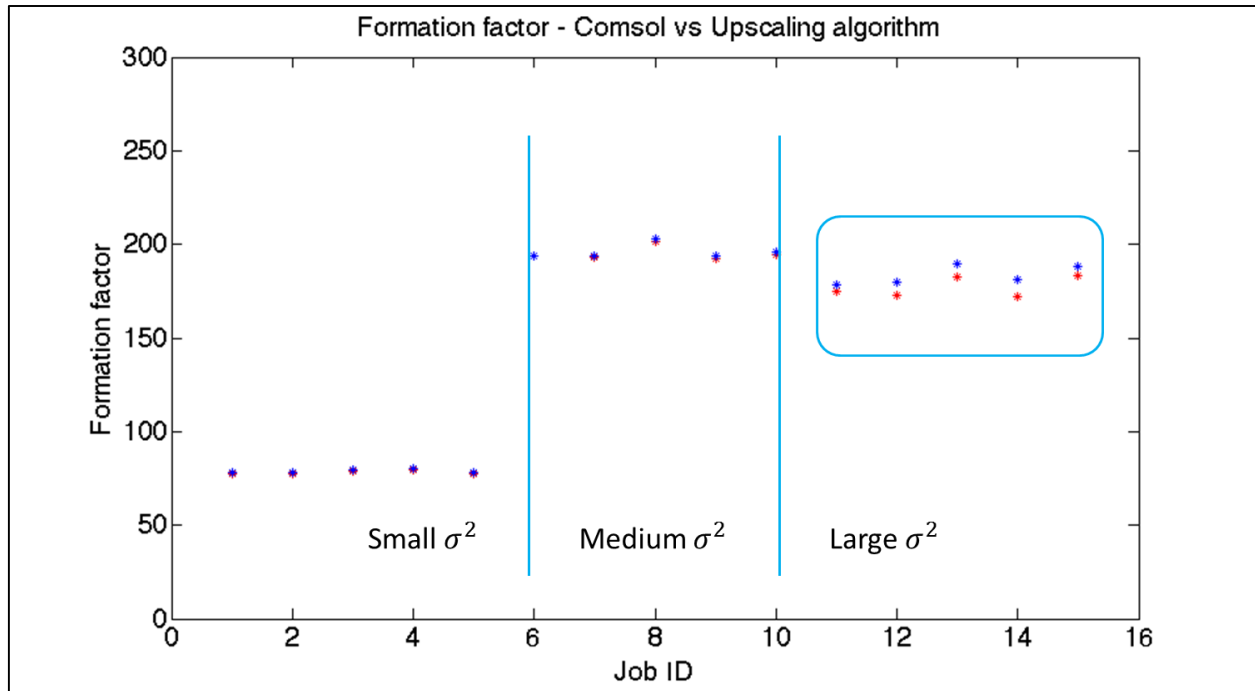
Figure 5-8 – Upscaling of formation resistivity factor (model-by-model validation)
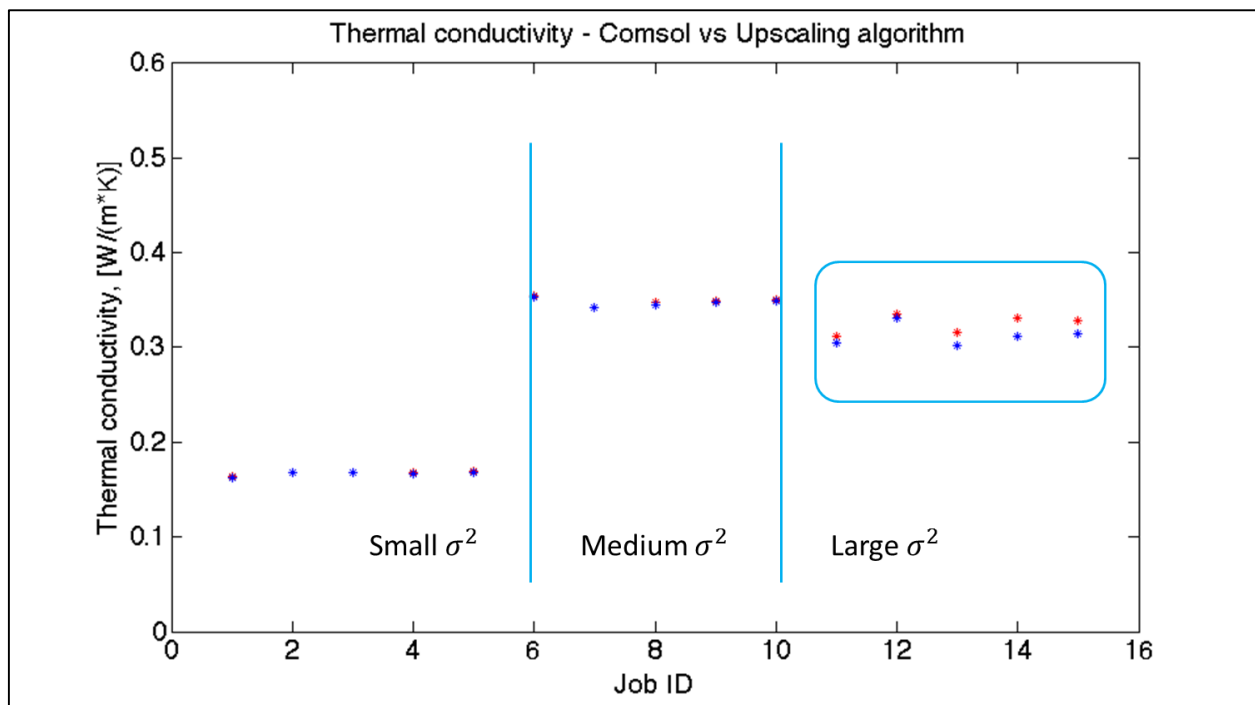
Figure 5-9 – Upscaling of thermal conductivity (model-by-model validation)

5.3 Upscaling approach using computer tomography images

The process of generating three dimensional geometry from a stack of computer tomography (CT) images was described in Chapter 3. For a quick review the main steps are presented here as well to make a complete picture of upscaling approach using a stack of CT images. Before the actual core is scanned in CT scanner, a set of samples with known density is used to obtain a so-called calibration line. This set of samples is called calibration set. For the purposes of this thesis the calibration set consisted of acetone, water, dolomite, sandstone, Berea sand and aluminum. Two CT images obtained for each calibration set and average greyscale (GS) value for each component is calculated. Greyscale value is then converted to a so-called CT number, using the following relation:

$$CT = GS - 32768 \hspace{4cm} \textbf{5.12}$$

So, the calibration line is the dependency of density of material on the CT number. This dependency can be described as linear with the coefficient of determination close to one (0.9967). The equation of calibration line is as follow:

$$\rho_b = m * CT + b \hspace{4cm} \textbf{5.13}$$

where ρ_b is the bulk density of material, m is the slope of the calibration line and b is the intercept. This calibration line allows to determine the density of material by knowing its CT number. The measured densities of the calibration set components are presented in Table 5-1and the calibration line used for the purposes of this thesis is presented in Figure 5-10.

Component	CT number	Density, kg/m^3
Acetone	-236	787
Water	-2	998
Dolomite	1477	2191
Sandstone	1350	2207
Berea Sand	1164	2025
Aluminium	1953	2696

Table 5-1 – CT calibration set properties
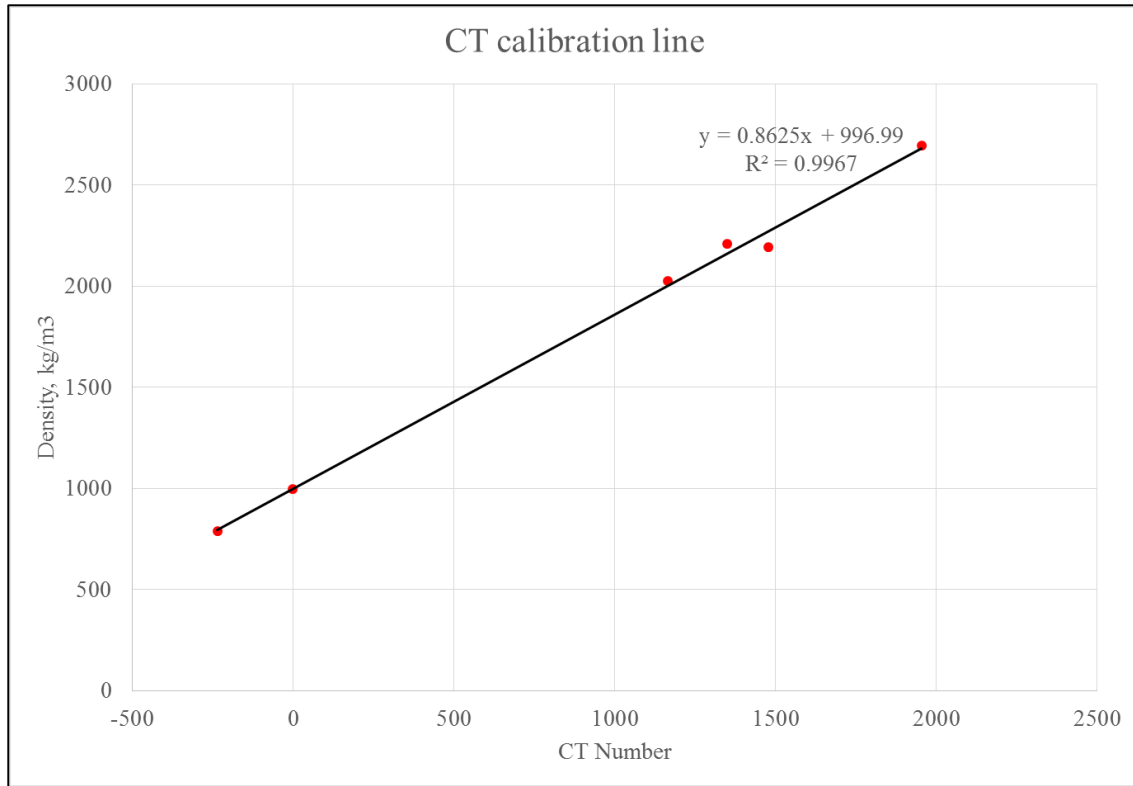
Figure 5-10 – CT calibration line

From the density of the porous material one can calculate the porosity using the following relation:

$$\phi = \frac{\rho_b - \rho_{gr}}{\rho_w S_w + \rho_o S_o + \rho_g S_g - \rho_{gr}}$$

5.14

where ϕ is the porosity of material, ρ_{gr} is the grain density of material, ρ_w, ρ_o, ρ_g are the densities of water, oil and gas respectively and S_w, S_o, S_g are the saturations of water, oil and gas respectively.

So if one knows the fluid saturations it is possible to determine the porosity of the core sample by knowing its CT number. Saturation is obtained using nuclear magnetic resonance (NMR) technology. It allows estimation of the mass of water and oil based on their amplitude index calculated from NMR spectra (Canet 1996). Since NMR cannot detect the gas phase, the gas saturation should be determined in another way. For this purposes the porosity of one piece of the core sample is measured. Knowing mass of water, mass of oil, porosity, and density of water, density of oil, density of gas, grain density, bulk density and porosity one can estimate the gas

115

saturation of the core sample. This gas saturation is then assumed for all other parts of the core, so the porosity of the other parts of the core can be estimated. It is also possible to use well log porosity data.

It was mentioned in Chapter 3 that a stack of CT images (consecutive slices of full length core) can be used to reconstruct the three dimensional geometry of the core by converting pixels (2D) into voxels (3D) and meshing them. At his stage of converting from stack of 2D images to 3D geometry it is possible to assign individual properties to each voxel based on the procedure described above. So for each voxel we have bulk density, porosity and fluid saturations.

One of the questions that may arise is which grain density to use. To answer this question one need to identify different materials that core sample contains. This identification can be done based on the density of material as this is the property that can be easily calculated from known CT numbers (or GS values). The histogram of density distribution in the core sample helps to make this decision. The density histogram is build based on voxels: for each voxel the density is calculated using the calibration line and then voxels with the same density are counted together. So the X-axis is density and Y-axis is the number of voxels. The density histogram is then split into intervals along the X-axis in such a way that the porosity variation within each interval is not very significant (up to 3 %). This procedure allows to join the materials together based on similar grain density and porosity and consider them as one material (mask). Finally the core sample is separated into regions of different materials (masks) with known properties. The effective thermal conductivity of each mask can be calculated using the geometric mean mixing rule as follows:

$$k_{mask} = k_o^{\varphi S_o} k_w^{\varphi S_w} k_g^{\varphi S_g} k_{grain}^{(1-\varphi)} \qquad\qquad \mathbf{5.15}$$

Here it should be mentioned, that the geometric mean mixing rule was used because particle size distribution data was not available for the core samples analyzed. But if the particle size distribution data is available one can use the custom generated Sigmoid mixing rule instead for each material separately.

This information about masks and their properties is then provided into Simpleware ScanIP software which reconstructs the three dimensional geometry of core sample and assigns properties to the different masks created based on density distribution histogram. The reconstructed geometry is then converted into COMSOL-compatible format and this geometry is

ready to run the macro scale heat transfer problem (based on Fourier's Law physics). For the purposes of this the scaling up of the thermal conductivity of porous media is discussed in details. But this procedure is not limited to the thermal conductivity only and can be applied to scale up other properties like electrical resistivity and permeability. The resulting value of thermal conductivity is considered a scaled up property. The overall workflow for the procedure is presented in Figure 5-11.
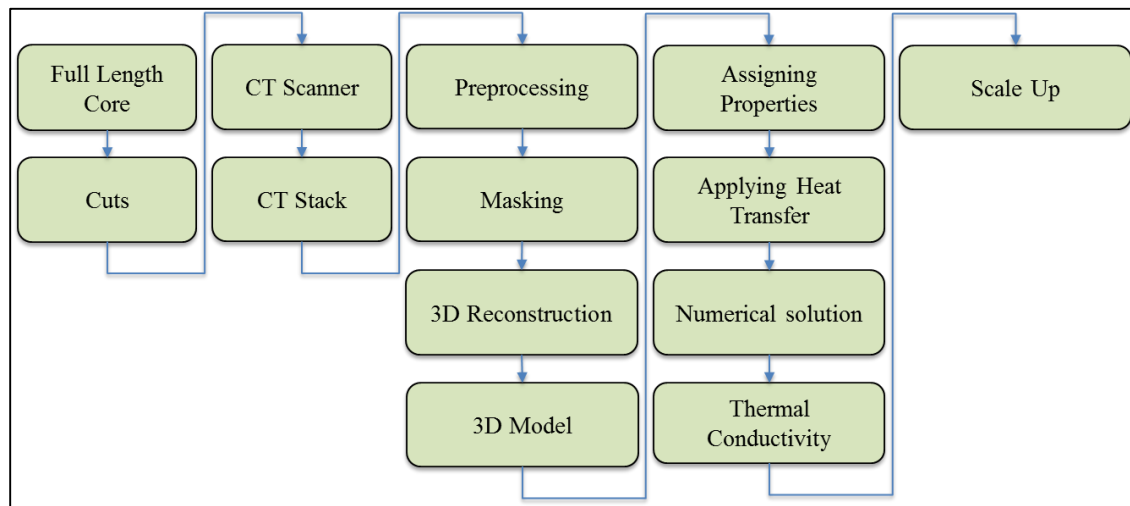
Figure 5-11 – Thermal conductivity computational workflow

Let's take a look at an example. The histogram for core sample classified as the muddy inclined heterolithic stratification (MIHS) is presented in Figure 5-12. The core sample itself is presented in Figure 5-13. From the Figure 5-13 it is possible to distinguish three different materials: two are of a grey colour and one is white. The same three materials can be distinguished on density histogram. The peak on the right side corresponds to the densest material (white) and another two peaks corresponds to two other materials. These two peaks are combined because the materials have similar density. According to the X-ray powder diffraction (XRD) analysis for this core sample: the two grey material are the two different sands and the white material is siderite.
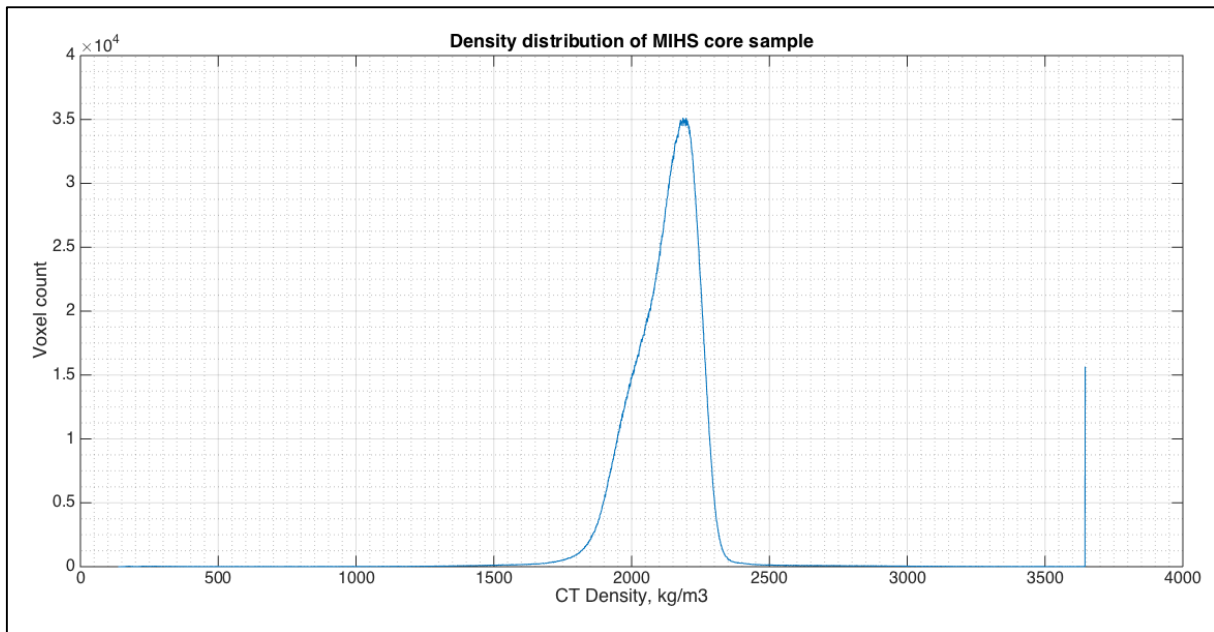
Figure 5-12 – Density distribution of MIHS core sample
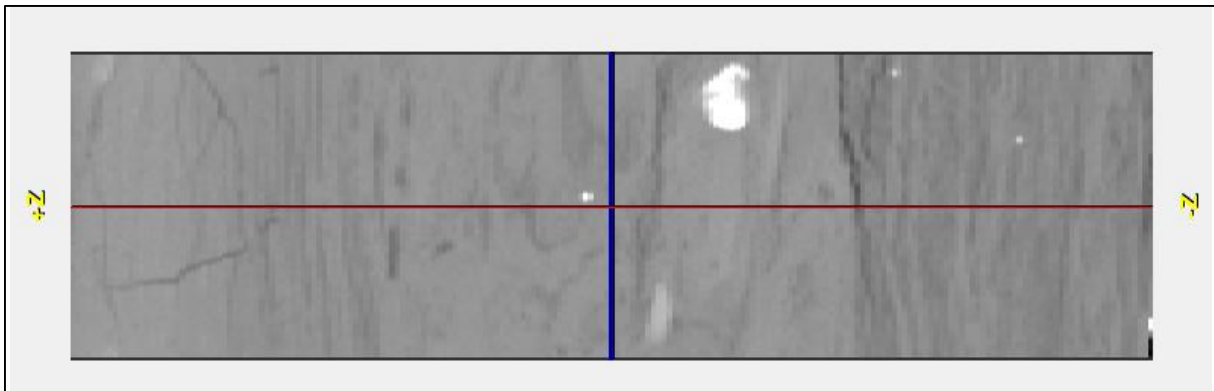
Figure 5-13 – MIHS core sample

According to the procedure described above the MIHS core sample is separated into different materials (masks) with different grain densities (see Table 5-2). Thermal properties of base materials and fluids are presented in Table 5-3 and Table 5-4 respectively.

Mask	Density		Base	Saturation		
name	Start	End	Material	Water	Oil	Air
MAT1_1	1844	1952	Sand1	0.55	0.1	0.35
MAT1_2	1952	2060	Sand1	0.55	0.1	0.35
MAT2_1	2060	2146	Sand2	0.55	0.1	0.35
MAT2_2	2146	2189	Sand2	0.55	0.1	0.35
MAT2_3	2189	2232	Sand2	0.55	0.1	0.35
MAT2_4	2232	2318	Sand2	0.55	0.1	0.35
MAT3_1	3638	3646	Siderite	0.55	0.1	0.35

Table 5-2 – Material for MIHS sample

Base material	Grain density kg/m^3	Grain thermal conductivity $W/(m \cdot K)$
Sand1	2650	7.08
Sand2	2550	2.44
Siderite	3811	3

Table 5-3 – Properties of base materials

Fluid	Density kg/m^3	Thermal conductivity $W/(m \cdot K)$
Oil	1014	0.14
Water	1007	0.61
Air	1.2	0.024

Table 5-4 – Properties of fluids

The thermal conductivity map of different masks is presented in Figure 5-14. The geometry presented on this figure was reconstructed using Simpleware Scan IP software and the procedure described above. After running the heat transfer model with fixed but different temperatures as the boundary conditions at the opposite sides of the parallelepiped, the scaled up thermal conductivity of the MIHS core sample was calculated.
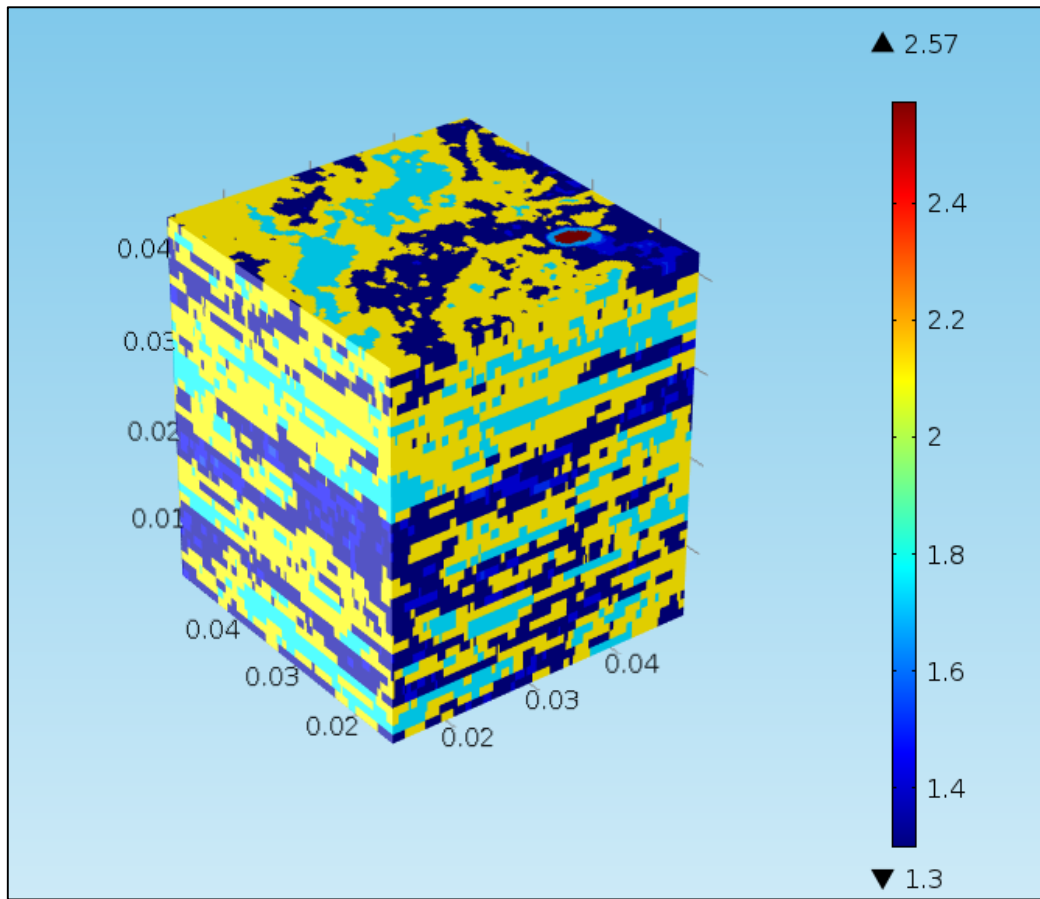
Figure 5-14 – MIHS core sample thermal conductivity map

The same procedure as described in MIHS example was repeated for several different cores: mudstone, sandstone, sandy inclined heterolithic stratification (SIHS), muddy inclined heterolithic stratification (MIHS). Experimental measurements of the effective thermal conductivity of the same core samples were taken from Arthur, *et al.* (Arthur, *et al.* 2015). The results are presented in Table 5-5 and the cross plot of comparison experimental results vs. prediction is presented in Figure 5-15. From the graph one can conclude that the upscaling using CT images gives fairly good prediction of effective thermal conductivity for Sandstone-1, Sandstone-2, MIHS and SIHS samples, while it overestimates the effective thermal conductivity for Mudstone-1 and Mudstone-2 samples; and underestimates the effective thermal conductivity of Breccia-1 sample. One of the possible reasons for the underestimation and overestimation of effective thermal conductivity is the mixing rule used to calculate the effective thermal conductivity of a mask from known fluid saturations and thermal conductivities of constituents

of porous media. In all the samples described in this section the geometric mean mixing rule was used. But as it was showed in the previous chapter the geometric mean mixing rules does not all the time accurately predicts the effective thermal conductivity of porous media. It was not possible to apply Sigmoid mixing rule as there was no data about particle size distribution available.

Sample name	Sample#	Modeling ETC $W/(m \cdot K)$	Experimental ETC $W/(m \cdot K)$
Mudstone-1	1	1.08	0.77
	2	1.13	0.58
	3	1.14	0.69
Sandstone-1	1	0.85	0.8
	2	0.89	0.8
	3	0.83	0.8
Sandstone-2	1	1.63	1.73
	2	1.56	1.73
	3	1.7	1.73
Mudstone-2	1	1.45	0.72
	2	1.4	1.09
	3	1.47	1.15
SIHS-1	1	1.3	1.39
	2	1.35	1.32
	3	1.35	1.32
MIHS-1	1	1.73	1.83
	2	1.59	1.52
	3	1.53	1.65
Breccia-1	1	2.4	3.98
	2	2.6	3.86
	3	3.54	3.84

Table 5-5 – Comparison of experimental and scaled up results
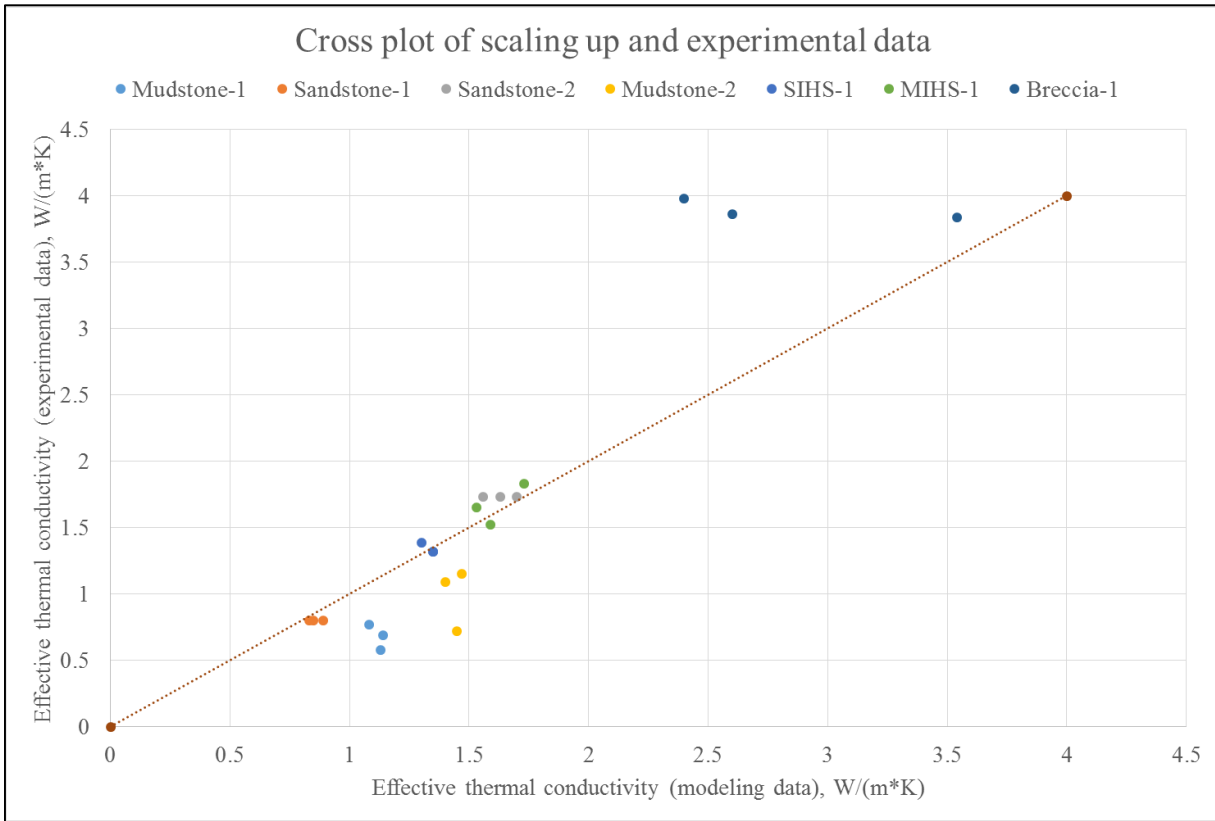
Figure 5-15 – Cross plot of experimental data and modeling data

The following resulting statements can be drawn as the outcome of this chapter:

- Two upscaling approaches were described and analyzed: network upscaling and upscaling using CT images

- The network upscaling approach was validated using model-by-model validation approach and it predicts the scaled up version of reservoir properties with a good accuracy for distributions of parameters with standard deviation of up to 30% of mean value

- The upscaling approach using CT images gives good prediction for the effective thermal conductivity of certain types of unconsolidated core samples with application of geometric mean mixing rule. But the application of custom created mixing rule based on particle size distribution is recommended.

Chapter 6: **Summary and conclusions and recommendations for future work**

6.1 Summary and conclusions

The following statements summarize the main steps performed in this thesis:

1) A literature review on the mixing rules for the effective thermal conductivity of porous media was performed. The advantages and disadvantages of mixing rules available in literature were discussed. Methods of experimental determination of effective thermal conductivity of porous media were discussed.

2) Different approaches of creating virtual porous media were discussed both at a pore scale level and at a core scale level. Two meshing approaches have been presented: voxel-based and geometry based.

3) A numerical model for heat transfer at the pore scale level has been developed and validated by experimental data available from literature. The effects of size of contact area between the grains, numerical mesh size and differences between voxel-based meshing and geometry-based meshing approaches were analyzed. The effective thermal conductivities of virtually generated sandstone samples were calculated.

4) A novel mixing rule to calculate the effective thermal conductivity of unconsolidated porous medium based on its particle size distribution was developed. The optimal number of grains was determined for the novel mixing rule generation. The effect of different particle size distributions was discussed. The physical meaning of the coefficients of the novel mixing rule was discussed. The novel mixing rule was compared to other literature available mixing rules and the differences were discussed.

5) Two different upscaling approaches were presented and discussed: equivalent network and upscaling based on computer tomography images. Network modelling approach was validated using model-by-model validation technique. The upscaling based on computer tomography was applied to predict the effective thermal conductivity of real oil sands core samples.

The following are the main conclusions drawn as the result of the work performed in this thesis:

1) The numerical model of steady-state heat conduction in porous media shows good prediction of the effective thermal conductivity of porous media within the range of solid to fluid thermal conductivity ratio of 10 to 100.

2) It has been numerically shown that the effect of contact area between the gains is very important in modelling the effective thermal conductivity of porous media, especially for the high values of solid to fluid thermal conductivity ratios.

3) Geometry-based meshing approach showed better results than the voxel-based meshing approach.

4) After a certain size of the mesh elements its effect on the effective thermal conductivity computations is negligible.

5) Particle size distribution data is an important piece of information regarding an oil sand sample. This information is not used in any available literature mixing rules to predict the effective thermal conductivity of porous media.

6) A novel mixing rule which uses the particle size distribution data as an input has been developed. The mixing rule involves only point contact between the grains of spherical shape.

7) None of the available literature mixing rules can accurately predict the effective thermal conductivity of porous media in the region of interest (solid to fluid thermal conductivity ratios of 10 to 100 which are typical for oil sand components). The novel mixing rule predicts the effective thermal conductivity with the coefficient of determination of one.

8) The Equivalent Network upscaling approach shows good results for the prediction of scaled up reservoir properties.

9) Upscaling using computer tomography images showed accurate prediction of effective thermal conductivity of sandstone, muddy and sandy inclined heterolithic stratification core samples. It under predicted the results for Breccia core samples and over predicts for the mudstone core samples.

6.2 Recommendations for future work

There are no ideal results in the research work, as any models and experiments have certain underlying assumptions. Thus any model can be improved or extended. The following are suggestions and recommendations for future work:

1) Introduce contact area between the spherical grains by adding the hyperbolical or cylindrical inclusion (rings) around the point of contact between the grains.

2) Analyze the correlations between the coefficients of novel mixing rule and statistical parameters of particle size distributions (mean, standard deviation, etc.)

3) Use three dimensional printing technologies to "print" the core sample and conduct experiments to validate the numerical models and novel mixing rule.

References

Arthur, J. K., H Sadeghi, O Akinbolabola, S Cameron, and A Kantzas. 2015. "Thermal Conductivity Measurements of Surmont Reservoir Samples.", TIPM Report#380, Calgary, Alberta.

Arthur, James Kofi, Oluwaseyi Akinbobola, Sergey Kryuchkov, and Apostolos Kantzas. 2015. "Thermal Conductivity Measurements of Bitumen Bearing Reservoir Rocks.", SPE-174434-MS, *SPE Canada Heavy Oil Technical Conference.* Calgary, Alberta, Canada: Soociety of Petroleum Engineers.

Birch, F., and H. Clark. 1940. "The Thermal Conductivity of Rocks and its Dependence Upon Temperature and Composition." *American Journal of Science* 238 (8): 529-558.

Bird, R. B., W. E. Stewart, and E. N. Lightfoot. 2007. *Transport phenomena.* John Willey and Sons.

Bland, W. F., and R. L. Davidson. 1967. *Petroleum Processing Handbook.* New York: McGraw-Hill.

Brandt, Adam R., Jacod Englander, and Sharad Bharadwaj. 2013. "The energy efficeincy of oil sands extraction: Energy return ratios from 1970 to 2010." *Energy* 55: 693-702.

Butler, Roger M. 1991. *Thermal Recovery of Oil and Bitumen.* Prentice Hall.

Canadian Association of Petroleum Producers. 2015. *January 2015 Capital Investment and Drilling Forecast Update.* Canadian Association of Petroleum Producers.

Canet, Daniel. 1996. *Nuclear Magnetic Resonance. Concepts and Methods.* John Wiley and Sons Ltd.

Carson, J. K., S. J. Lovatt, D. J. Tanner, and A. C. Cleland. 2005. "Thermal conductivity bounds for isotropic, porous materials." *International Journal of Heat and Mass Transfer* 48: 2150-2158.

Clayton, R P. 2001. *Fundamentals of Electric Circuit Analysis.* John Wiley & Sons, Inc.

Eucken, A. 1932. "Die Wärmeleitfähigkeit keramischer feuerfester Stoffe." *VDI-Forschungsh* 353.

Farouq Ali, S. M. 1974. "*Steam Injection" in Secondary and Tertiary Oil Recovery Processes.* Published by the Interstate Oil Compact Commission, Oklahoma City, Oklahoma.

Gates, Ian D., and Stephen R. Larter. 2014. "Energy efficiency and emissions intensity of SAGD." *Fuel* 115: 706-713.

Hashin, Z, and S Shtrikman. 1962. "A Variational Approach to the Theory of the Effective Magnetic Permeability of Multiphase Materials." *Journal of Applied Physics* 33 (10): 3125-3131.

Hestenes, M R, and E Stiefel. 1952. "Methods of Conjugate Gradients for Solving Linear Systems." *Journal of Research of the National Bureau of Standards* 409-436.

Holly, Christopher, Martin Mader, and Jesse Toor. 2012. *Oil sands production profile.* Edmonton: Alberta Department of Energy.

Kantzas, Apostolos. 1985. *Computer Simulation of Relative Permeability Properties of Porous Media (Master's Thesis).* Waterloo, Ontario, Canada.

Kaviany, Massoud. 1999. *Principles of Heat Transfer in Porous Media.* Springer.

Krupiczka, R. 1967. "Analysis of thermal conductivity in granular materials." *International Chemical Engineering* 7 (1): 122-144.

Kunii, Daizo, and J M Smith. 1960. "Heat Transfer Characteristics of Porous Rocks." *AIChE Journal* 6 (1): 71-78.

Maxwell, J C. 1873. *A Treatise on Electricity and Magnetism.* Oxford: Clarendon Press.

McQuillan, F. J., J. R. Culham, and M. M. Yovanovich. 1984. "Properties of Dry Air at One Atmosphere." Microelectronics Heat Transfer Lab, University of Waterloo, Waterloo, Ontario.

National Energy Board. 2013. *Canada's Energy Future 2013. Energy Surplus and Demand Projections 2035.* National Energy Board.

Nield, D. A. 1991. "Estimation of the stagnant thermal conductivity of saturated porous media." *International Journal of Heat and Mass Transfer* 34 (6): 1575-1576.

Nozad, I, R G Carbonell, and S Whitaker. 1985. "Heat conduction in multiphase systems II. Experimental method and results for three phase systems." *Chemical Engineering Scinece* 40 (5): 857-863.

Prasad, V, N Kladias, A Bandyopadhaya, and Q Tian. 1989. "Evaluation of correlations for stagnant thermal conductivity of liquid-saturated porous beds of spheres." *International Journal of Heat and Mass Transfer* 32 (9): 1793-1796.

Tsotsas, E., and H. Martin. 1987. "Thermal conductivity of packed beds: a review." *Chemical Engineering and Processing: Process Intensification* 22 (1): 19-37.

Van Antwerpen, W, C G Du Toit, and P G Rousseau. 2010. "A review of correlations to model the packing structure and effective thermal conductivity in packed beds of mono-sized spherical particles." *Nuclear Engineering and Design* 240: 1803-1818.

Woodside, W, and J H Messmer. 1961. "Thermal Conductivity of Porous Media. I. Unconsolidated Sands." *Journal of Applied Physics* 32 (9): 1688-1699.

Xu, Conglin, and Laura Bell. 2014. "Global reserves, oil production show increases for 2014." *Oil and Gas Journal* 112 (12): 30-33.

Zehner, P, and E U Schlunder. 1970. "Wärmeleitfähigkeit von Schüttungen bei mäßigen Temperatu." *Chemie. Ingr.-Tech.* 42 (14): 933-941.

Appendices A – Results of numerical experiments

d, mm	$\dfrac{d}{r_s}$	Effective thermal conductivity, $\dfrac{W}{m \cdot K}$			
		Ratio=10000	Ratio=1000	Ratio=100	Ratio=10
-0.00100	-1.00	2.35	2.35	2.32	2.03
-0.00098	-0.98	2.37	2.37	2.33	2.04
-0.00097	-0.97	2.38	2.38	2.35	2.05
-0.00095	-0.95	2.40	2.39	2.36	2.06
-0.00094	-0.94	2.41	2.41	2.37	2.07
-0.00092	-0.92	2.43	2.42	2.39	2.08
-0.00091	-0.91	2.44	2.44	2.40	2.09
-0.00089	-0.89	2.46	2.46	2.42	2.10
-0.00088	-0.88	2.48	2.47	2.43	2.11
-0.00086	-0.86	2.49	2.49	2.45	2.12
-0.00085	-0.85	2.51	2.51	2.47	2.14
-0.00083	-0.83	2.53	2.52	2.48	2.15
-0.00082	-0.82	2.55	2.54	2.50	2.16
-0.00080	-0.80	2.57	2.56	2.52	2.17
-0.00079	-0.79	2.59	2.58	2.54	2.18
-0.00077	-0.77	2.61	2.60	2.56	2.20
-0.00076	-0.76	2.63	2.62	2.58	2.21
-0.00074	-0.74	2.65	2.64	2.60	2.22
-0.00073	-0.73	2.67	2.66	2.62	2.23
-0.00071	-0.71	2.69	2.69	2.64	2.25
-0.00070	-0.70	2.72	2.71	2.66	2.26
-0.00068	-0.68	2.74	2.73	2.68	2.28
-0.00067	-0.67	2.76	2.76	2.71	2.29
-0.00065	-0.65	2.79	2.78	2.73	2.31
-0.00064	-0.64	2.82	2.81	2.76	2.32
-0.00062	-0.62	2.84	2.84	2.78	2.34
-0.00061	-0.61	2.87	2.87	2.81	2.36
-0.00059	-0.59	2.90	2.89	2.84	2.37
-0.00058	-0.58	2.93	2.92	2.86	2.39
-0.00056	-0.56	2.96	2.96	2.89	2.41
-0.00055	-0.55	2.99	2.99	2.92	2.43
-0.00053	-0.53	3.03	3.02	2.96	2.45
-0.00052	-0.52	3.06	3.06	2.99	2.47
-0.00050	-0.50	3.10	3.09	3.02	2.49

d, mm	$\dfrac{d}{r_s}$	Effective thermal conductivity, $\dfrac{W}{m \cdot K}$			
		Ratio=10000	Ratio=1000	Ratio=100	Ratio=10
-0.00048	-0.48	3.14	3.13	3.06	2.51
-0.00047	-0.47	3.18	3.17	3.10	2.53
-0.00045	-0.45	3.22	3.21	3.14	2.55
-0.00044	-0.44	3.26	3.26	3.18	2.58
-0.00042	-0.42	3.31	3.30	3.22	2.60
-0.00041	-0.41	3.36	3.35	3.26	2.63
-0.00039	-0.39	3.41	3.40	3.31	2.65
-0.00038	-0.38	3.46	3.45	3.36	2.68
-0.00036	-0.36	3.52	3.51	3.41	2.71
-0.00035	-0.35	3.58	3.57	3.47	2.74
-0.00033	-0.33	3.64	3.63	3.53	2.77
-0.00032	-0.32	3.70	3.69	3.59	2.80
-0.00030	-0.30	3.77	3.76	3.65	2.83
-0.00029	-0.29	3.85	3.84	3.72	2.87
-0.00027	-0.27	3.93	3.92	3.79	2.91
-0.00026	-0.26	4.02	4.00	3.87	2.95
-0.00024	-0.24	4.11	4.10	3.96	2.99
-0.00023	-0.23	4.21	4.20	4.05	3.03
-0.00021	-0.21	4.32	4.30	4.15	3.08
-0.00020	-0.20	4.44	4.42	4.26	3.13
-0.00018	-0.18	4.57	4.55	4.37	3.18
-0.00017	-0.17	4.72	4.70	4.50	3.23
-0.00015	-0.15	4.88	4.86	4.65	3.29
-0.00014	-0.14	5.06	5.04	4.81	3.36
-0.00012	-0.12	5.27	5.24	4.99	3.43
-0.00011	-0.11	5.51	5.48	5.20	3.51
-0.00009	-0.09	5.80	5.76	5.45	3.59
-0.00008	-0.08	6.14	6.10	5.74	3.68
-0.00006	-0.06	6.58	6.53	6.10	3.79
-0.00005	-0.05	7.15	7.09	6.56	3.90
-0.00003	-0.03	7.98	7.91	7.21	4.04
-0.00002	-0.02	9.46	9.34	8.27	4.21
0.00000	0.00	33.37	22.28	12.13	4.43
0.00002	0.02	1661.20	170.75	21.61	4.67
0.00003	0.03	2296.40	233.06	26.89	4.87

d, mm	$\dfrac{d}{r_s}$	Effective thermal conductivity, $\dfrac{W}{m \cdot K}$			
		Ratio=10000	Ratio=1000	Ratio=100	Ratio=10
0.00005	0.05	2769.90	279.76	31.01	5.06
0.00006	0.06	3160.10	318.51	34.50	5.23
0.00008	0.08	3497.10	352.18	37.57	5.40
0.00009	0.09	3796.60	381.88	40.32	5.55
0.00011	0.11	4065.90	408.61	42.81	5.70
0.00012	0.12	4313.20	433.17	45.10	5.83
0.00014	0.14	4541.30	455.84	47.24	5.97
0.00015	0.15	4754.00	476.98	49.23	6.09
0.00017	0.17	4952.70	496.75	51.10	6.21
0.00018	0.18	5140.30	515.41	52.88	6.33
0.00020	0.20	5317.30	533.02	54.56	6.44
0.00021	0.21	5485.00	549.71	56.15	6.55
0.00023	0.23	5644.50	565.59	57.67	6.65
0.00024	0.24	5795.90	580.66	59.11	6.75
0.00026	0.26	5941.30	595.14	60.50	6.85
0.00027	0.27	6080.00	608.96	61.83	6.95
0.00029	0.29	6212.30	622.13	63.10	7.04
0.00030	0.30	6340.00	634.85	64.32	7.13
0.00032	0.32	6461.70	646.98	65.49	7.21
0.00033	0.33	6579.50	658.72	66.63	7.29
0.00035	0.35	6692.10	669.94	67.71	7.37
0.00036	0.36	6801.40	680.83	68.77	7.45
0.00038	0.38	6905.80	691.25	69.77	7.53
0.00039	0.39	7007.40	701.37	70.76	7.60
0.00041	0.41	7105.00	711.09	71.70	7.67
0.00042	0.42	7198.90	720.46	72.61	7.74
0.00044	0.44	7290.40	729.58	73.49	7.81
0.00045	0.45	7378.20	738.34	74.34	7.88
0.00047	0.47	7463.70	746.86	75.17	7.94
0.00048	0.48	7546.00	755.07	75.97	8.00
0.00050	0.50	7625.30	762.98	76.74	8.06

Table A-1 – Results of numerical experiment #02: effect of contact area (wide range)

d, mm	$\dfrac{d}{r_s}$	Effective thermal conductivity, $\dfrac{W}{m \cdot K}$			
		Ratio=10000	Ratio=1000	Ratio=100	Ratio=10
-0.000100	-0.100	5.620	5.589	5.294	3.538
-0.000098	-0.098	5.658	5.626	5.327	3.549
-0.000096	-0.096	5.697	5.664	5.360	3.560
-0.000094	-0.094	5.736	5.703	5.394	3.572
-0.000092	-0.092	5.777	5.743	5.428	3.583
-0.000090	-0.090	5.818	5.784	5.464	3.595
-0.000088	-0.088	5.861	5.826	5.500	3.607
-0.000086	-0.086	5.905	5.869	5.537	3.619
-0.000084	-0.084	5.949	5.913	5.575	3.631
-0.000082	-0.082	5.995	5.958	5.614	3.643
-0.000080	-0.080	6.043	6.005	5.654	3.656
-0.000078	-0.078	6.092	6.053	5.695	3.669
-0.000076	-0.076	6.142	6.103	5.738	3.682
-0.000074	-0.074	6.194	6.154	5.781	3.695
-0.000072	-0.072	6.248	6.206	5.826	3.708
-0.000070	-0.070	6.303	6.261	5.872	3.722
-0.000068	-0.068	6.360	6.317	5.919	3.735
-0.000066	-0.066	6.419	6.375	5.968	3.750
-0.000064	-0.064	6.480	6.435	6.019	3.764
-0.000062	-0.062	6.544	6.497	6.071	3.778
-0.000060	-0.060	6.609	6.562	6.125	3.793
-0.000058	-0.058	6.677	6.628	6.181	3.808
-0.000056	-0.056	6.748	6.698	6.238	3.823
-0.000054	-0.054	6.822	6.770	6.298	3.839
-0.000052	-0.052	6.899	6.846	6.360	3.855
-0.000049	-0.049	6.979	6.924	6.425	3.871
-0.000047	-0.047	7.063	7.006	6.492	3.888
-0.000045	-0.045	7.151	7.092	6.562	3.904
-0.000043	-0.043	7.243	7.183	6.636	3.922
-0.000041	-0.041	7.340	7.278	6.712	3.939
-0.000039	-0.039	7.443	7.378	6.793	3.957
-0.000037	-0.037	7.551	7.483	6.877	3.975
-0.000035	-0.035	7.665	7.595	6.966	3.994
-0.000033	-0.033	7.786	7.713	7.058	4.013
-0.000031	-0.031	7.916	7.840	7.158	4.032

d, mm	$\dfrac{d}{r_s}$	Effective thermal conductivity, $\dfrac{W}{m \cdot K}$			
		Ratio=10000	Ratio=1000	Ratio=100	Ratio=10
-0.000029	-0.029	8.056	7.975	7.263	4.052
-0.000027	-0.027	8.206	8.121	7.375	4.073
-0.000025	-0.025	8.368	8.279	7.495	4.094
-0.000023	-0.023	8.544	8.450	7.625	4.116
-0.000021	-0.021	8.738	8.638	7.765	4.138
-0.000019	-0.019	8.952	8.845	7.917	4.161
-0.000017	-0.017	9.191	9.076	8.084	4.185
-0.000015	-0.015	9.462	9.336	8.269	4.210
-0.000013	-0.013	9.772	9.635	8.476	4.235
-0.000011	-0.011	10.137	9.984	8.712	4.262
-0.000009	-0.009	10.578	10.405	8.986	4.289
-0.000007	-0.007	11.133	10.931	9.315	4.318
-0.000005	-0.005	11.880	11.634	9.725	4.348
-0.000003	-0.003	13.020	12.692	10.278	4.379
-0.000001	-0.001	15.484	14.895	11.175	4.413
0.000001	0.001	459.760	55.901	13.399	4.448
0.000003	0.003	773.380	85.227	15.161	4.482
0.000005	0.005	985.650	105.510	16.557	4.514
0.000007	0.007	1156.300	121.970	17.764	4.546
0.000009	0.009	1302.700	136.160	18.845	4.577
0.000011	0.011	1432.300	148.760	19.833	4.608
0.000013	0.013	1549.500	160.190	20.748	4.638
0.000015	0.015	1657.500	170.750	21.607	4.667
0.000017	0.017	1757.900	180.570	22.417	4.696
0.000019	0.019	1852.100	189.800	23.186	4.725
0.000021	0.021	1940.700	198.500	23.919	4.753
0.000023	0.023	2025.200	206.800	24.623	4.780
0.000025	0.025	2105.600	214.710	25.299	4.807
0.000027	0.027	2182.300	222.250	25.949	4.834
0.000029	0.029	2256.200	229.530	26.578	4.860
0.000031	0.031	2327.300	236.530	27.187	4.887
0.000033	0.033	2395.600	243.260	27.777	4.912
0.000035	0.035	2461.800	249.790	28.349	4.938
0.000037	0.037	2526.300	256.150	28.910	4.963
0.000039	0.039	2588.800	262.320	29.455	4.988

d, mm	$\dfrac{d}{r_s}$	Effective thermal conductivity, $\dfrac{W}{m \cdot K}$			
		Ratio=10000	Ratio=1000	Ratio=100	Ratio=10
0.000041	0.041	2649.000	268.270	29.983	5.013
0.000043	0.043	2708.000	274.090	30.502	5.037
0.000045	0.045	2765.400	279.760	31.008	5.061
0.000047	0.047	2821.500	285.300	31.504	5.085
0.000049	0.049	2875.900	290.690	31.987	5.109
0.000052	0.052	2929.300	295.970	32.462	5.132
0.000054	0.054	2981.600	301.140	32.928	5.155
0.000056	0.056	3032.200	306.150	33.380	5.178
0.000058	0.058	3083.900	311.260	33.840	5.201
0.000060	0.060	3132.900	316.100	34.280	5.223
0.000062	0.062	3181.100	320.880	34.714	5.246
0.000064	0.064	3228.300	325.550	35.139	5.268
0.000066	0.066	3274.500	330.120	35.556	5.290
0.000068	0.068	3321.200	334.750	35.977	5.312
0.000070	0.070	3366.000	339.190	36.383	5.333
0.000072	0.072	3411.700	343.720	36.796	5.355
0.000074	0.074	3455.000	348.000	37.189	5.376
0.000076	0.076	3497.100	352.180	37.573	5.398
0.000078	0.078	3539.100	356.340	37.957	5.418
0.000080	0.080	3580.300	360.430	38.333	5.439
0.000082	0.082	3621.100	364.470	38.706	5.460
0.000084	0.084	3661.100	368.440	39.073	5.480
0.000086	0.086	3700.200	372.320	39.432	5.501
0.000088	0.088	3739.100	376.180	39.789	5.521
0.000090	0.090	3777.600	380.000	40.142	5.541
0.000092	0.092	3814.900	383.700	40.486	5.561
0.000094	0.094	3852.200	387.400	40.830	5.581
0.000096	0.096	3888.300	390.980	41.163	5.600
0.000098	0.098	3924.700	394.600	41.499	5.619
0.000100	0.100	3961.000	398.190	41.833	5.638

Table A-2 - Results of numerical experiment #02: effect of contact area (near contact region)

Number of grains	Target porosity	#	Porosity	ETC in direction, $W/(m \cdot K)$			
				Z (in)	Z (out)	X (in)	X (out)
300	Phi1	1	0.523	1.793	1.769	1.824	1.824
		2	0.527	1.767	1.793	1.780	1.781
		3	0.520	1.795	1.813	1.802	1.802
		4	0.519	1.813	1.798	1.807	1.807
		5	0.526	1.756	1.776	1.814	1.814
	Phi2	1	0.489	1.913	1.884	1.944	1.944
		2	0.495	1.901	1.886	1.888	1.888
		3	0.498	1.895	1.895	1.894	1.894
		4	-	-	-	-	-
		5	0.492	1.916	1.916	1.923	1.923
	Phi3	1	0.469	2.000	1.999	2.012	2.012
		2	0.462	2.052	2.052	2.046	2.046
		3	0.472	1.989	1.937	2.004	2.000
		4	0.473	1.928	1.905	2.018	2.018
		5	0.459	1.992	2.009	2.042	2.042
	Phi4	1	0.448	2.063	2.103	2.099	2.099
		2	0.444	2.112	2.112	2.118	2.118
		3	0.440	2.133	2.089	2.132	2.132
		4	0.450	2.004	2.060	2.091	2.091
		5	0.430	2.187	2.156	2.201	2.199
	Phi5	1	0.400	2.218	2.242	2.342	2.342
		2	0.401	2.278	2.252	2.302	2.302
		3	0.400	2.227	2.273	2.307	2.307
		4	0.406	2.222	2.211	2.271	2.271
		5	0.401	2.269	2.267	2.303	2.303

Number of grains	Target porosity	#	Porosity	ETC in direction, $W/(m \cdot K)$			
				Z (in)	Z (out)	X (in)	X (out)
700	Phi1	1	0.495	1.907	1.907	1.905	1.905
		2	-	-	-	-	-
		3	0.479	1.991	1.960	2.003	2.003
		4	0.479	2.013	2.013	1.999	1.999
		5	0.494	1.899	1.911	1.906	1.906
	Phi2	1	0.455	2.062	2.088	2.100	2.100
		2	0.465	2.026	2.026	2.004	2.004
		3	0.463	2.032	2.031	2.025	2.025
		4	0.467	2.003	2.023	2.013	2.013
		5	0.466	2.018	2.001	2.013	2.013
	Phi3	1	0.438	2.133	2.115	2.141	2.141
		2	0.439	2.130	2.110	2.129	2.129
		3	0.438	2.143	2.143	2.143	2.143
		4	0.439	2.096	2.107	2.128	2.128
		5	0.439	2.139	2.139	2.138	2.138
	Phi4	1	0.415	2.216	2.221	2.240	2.240
		2	0.415	2.210	2.202	2.229	2.229
		3	0.414	2.225	2.239	2.224	2.224
		4	0.410	2.241	2.247	2.262	2.262
		5	0.411	2.223	2.212	2.252	2.252
	Phi5	1	0.382	2.389	2.374	2.407	2.421
		2	0.383	2.400	2.372	2.421	2.421
		3	0.381	2.400	2.372	2.425	2.425
		4	0.380	2.403	2.383	2.430	2.430
		5	0.379	2.372	2.399	2.435	2.435

Number of grains	Target porosity	#	Porosity	ETC in direction, $W/(m \cdot K)$			
				Z (in)	Z (out)	X (in)	X (out)
1100	Phi1	1	0.484	1.940	1.928	1.958	1.958
		2	0.478	1.975	1.965	1.976	1.976
		3	0.470	2.022	2.023	2.039	2.039
		4	0.485	1.941	1.941	1.937	1.937
		5	-	-	-	-	-
	Phi2	1	0.440	2.140	2.153	2.146	2.146
		2	0.436	2.176	2.143	2.166	2.166
		3	0.453	2.057	2.066	2.065	2.064
		4	0.450	2.086	2.073	2.078	2.079
		5	0.447	2.096	2.096	2.102	2.102
	Phi3	1	0.490	1.862	1.862	1.852	1.852
		2	0.422	2.200	2.188	2.208	2.209
		3	0.488	1.864	1.841	1.862	1.862
		4	0.424	2.165	2.192	2.188	2.188
		5	-	-	-	-	-
	Phi4	1	0.399	2.291	2.290	2.305	2.305
		2	0.401	2.274	2.262	2.293	2.293
		3	0.401	2.290	2.274	2.294	2.294
		4	0.399	2.296	2.281	2.308	2.308
		5	0.382	2.381	2.402	2.419	2.418
	Phi5	1	0.378	2.408	2.415	2.441	2.441
		2	0.379	2.413	2.437	2.432	2.432
		3	0.380	2.377	2.410	2.426	2.426
		4	-	-	-	-	-
		5	0.385	2.400	2.384	2.409	2.409

Number of grains	Target porosity	#	Porosity	ETC in direction, $W/(m \cdot K)$			
				Z (in)	Z (out)	X (in)	X (out)
1500	Phi1	1	0.476	1.966	1.966	1.972	1.972
		2	0.475	1.980	1.980	1.975	1.975
		3	0.461	2.072	2.072	2.058	2.058
		4	0.476	1.979	1.970	1.973	1.973
		5	0.474	1.983	1.983	1.980	1.980
	Phi2	1	0.441	2.120	2.120	2.127	2.127
		2	0.429	2.195	2.177	2.202	2.202
		3	0.429	2.198	2.198	2.193	2.193
		4	-	-	-	2.117	2.117
		5	0.443	2.104	2.110	2.112	2.112
	Phi3	1	0.400	2.304	2.324	2.334	2.334
		2	0.414	2.234	2.234	2.237	2.237
		3	-	-	-	2.243	2.243
		4	0.415	2.221	2.223	2.233	2.233
		5	0.413	2.225	2.243	2.242	2.242
	Phi4	1	0.379	2.404	2.400	2.431	2.431
		2	0.382	2.400	2.380	2.420	2.420
		3	0.380	2.417	2.417	2.429	2.429
		4	0.381	2.389	2.417	2.433	2.433
		5	0.380	2.418	2.404	2.432	2.432

Number of grains	Target porosity	#	Porosity	ETC in direction, $W/(m \cdot K)$			
				Z (in)	Z (out)	X (in)	X (out)
2000	Phi1	1	0.468	2.007	1.995	2.006	2.006
		2	0.462	2.030	2.030	2.031	2.031
		3	0.466	2.015	2.015	2.012	2.012
		4	-	-	-	-	-
		5	0.467	2.012	2.012	2.011	2.011
	Phi2	1	0.433	2.157	2.151	2.145	2.145
		2	0.431	2.158	2.158	2.167	2.167
		3	0.434	2.139	2.134	2.149	2.149
		4	0.433	2.156	2.156	2.151	2.151
		5	0.435	2.137	2.121	2.145	2.145
	Phi3	1	0.404	2.270	2.269	2.273	2.273
		2	0.409	2.247	2.256	2.260	2.260
		3	0.405	2.257	2.272	2.276	2.276
		4	0.405	2.261	2.257	2.270	2.270
		5	0.407	2.261	2.262	2.272	2.272
	Phi4	1	0.382	2.404	2.397	2.415	2.415
		2	0.379	2.411	2.415	2.430	2.430
		3	0.381	2.416	2.422	2.429	2.429
		4	-	-	-	-	-
		5	-	-	-	-	-

Number of grains	Target porosity	#	Porosity	ETC in direction, $W/(m \cdot K)$			
				Z (in)	Z (out)	X (in)	X (out)
2500	Phi1	1	0.461	2.035	2.038	2.037	2.037
		2	0.449	2.117	2.117	2.120	2.120
		3	0.463	2.014	2.022	2.028	2.028
		4	0.461	2.033	2.028	2.033	2.033
		5	0.460	2.037	2.037	2.031	2.031
	Phi2	1	0.431	2.161	2.155	2.159	2.159
		2	0.419	2.244	2.253	2.243	2.243
		3	0.430	2.149	2.153	2.170	2.170
		4	0.427	2.172	2.178	2.172	2.172
		5	0.428	2.173	2.180	2.170	2.170
	Phi3	1	0.388	2.372	2.368	2.385	2.385
		2	0.402	2.285	2.277	2.287	2.287
		3	0.400	2.297	2.297	2.295	2.295
		4	0.388	2.379	2.371	2.392	2.392
		5	0.401	2.283	2.273	2.297	2.297
	Phi4	1	0.383	2.401	2.394	2.416	2.416
		2	0.380	2.431	2.406	2.427	2.427
		3	0.384	2.405	2.397	2.405	2.405
		4	0.385	2.392	2.389	2.401	2.401
		5	0.383	2.384	2.385	2.415	2.415
	Phi5	1	0.382	2.394	2.391	2.416	2.416
		2	0.383	2.392	2.395	2.418	2.418
		3	0.383	2.404	2.399	2.413	2.413
		4	0.386	2.395	2.380	2.403	2.403
		5	0.379	2.403	2.406	2.428	2.428

Table A-3 – Results of numerical experiment #06

K_s	K_e			
	PSD1	PSD2	PSD3	PSD4
0.001	0.280	0.257	0.258	0.254
0.0016	0.281	0.257	0.259	0.254
0.0026	0.282	0.258	0.260	0.255
0.0042	0.283	0.260	0.261	0.257
0.0067	0.285	0.262	0.264	0.259
0.0108	0.289	0.266	0.268	0.263
0.0174	0.295	0.272	0.274	0.269
0.0281	0.305	0.282	0.284	0.279
0.0452	0.320	0.298	0.301	0.295
0.0728	0.344	0.323	0.326	0.320
0.1172	0.382	0.362	0.366	0.359
0.1887	0.440	0.423	0.427	0.420
0.3039	0.531	0.515	0.520	0.513
0.4894	0.666	0.655	0.659	0.654
0.78805	0.868	0.863	0.865	0.862
1.269	1.158	1.164	1.162	1.165
2.043	1.563	1.587	1.579	1.591
3.290	2.105	2.160	2.144	2.169
5.298	2.790	2.900	2.879	2.917
8.53	3.598	3.802	3.783	3.832
13.74	4.476	4.828	4.825	4.875
22.12	5.343	5.901	5.935	5.970
35.62	6.119	6.927	7.017	7.019
57.36	6.753	7.820	7.980	7.934
92.4	7.233	8.534	8.765	8.666
148.7	7.574	9.063	9.359	9.212
239.5	7.807	9.437	9.780	9.597

K_s	K_e	9.687	10.067	9.852
	PSD1	PSD2	PSD3	PSD4
385.7	7.959	9.687	10.067	9.852
621	8.058	9.853	10.258	10.026
1000	8.124	9.949	10.381	10.164

Table A-4 – Results of numerical experiment #07

Appendices B – Numbering system for network modeling

The 3x3x3 equivalent network is presented in Figure B-1. The nodes of the upper layer are connected to the nodes of the bottom layer respectively. The nodes of the front layer are connected to the nodes of the rear layer respectively. The nodes of the left side layer are connected to the artificial node 0 and the nodes of the right side layer are connected to the artificial node 28. The nodes are numbered by layers as shown in Figure B-1 starting from the top layer. The edges are numbered in layers as well as shown in Figure B-2 starting from the top layer.
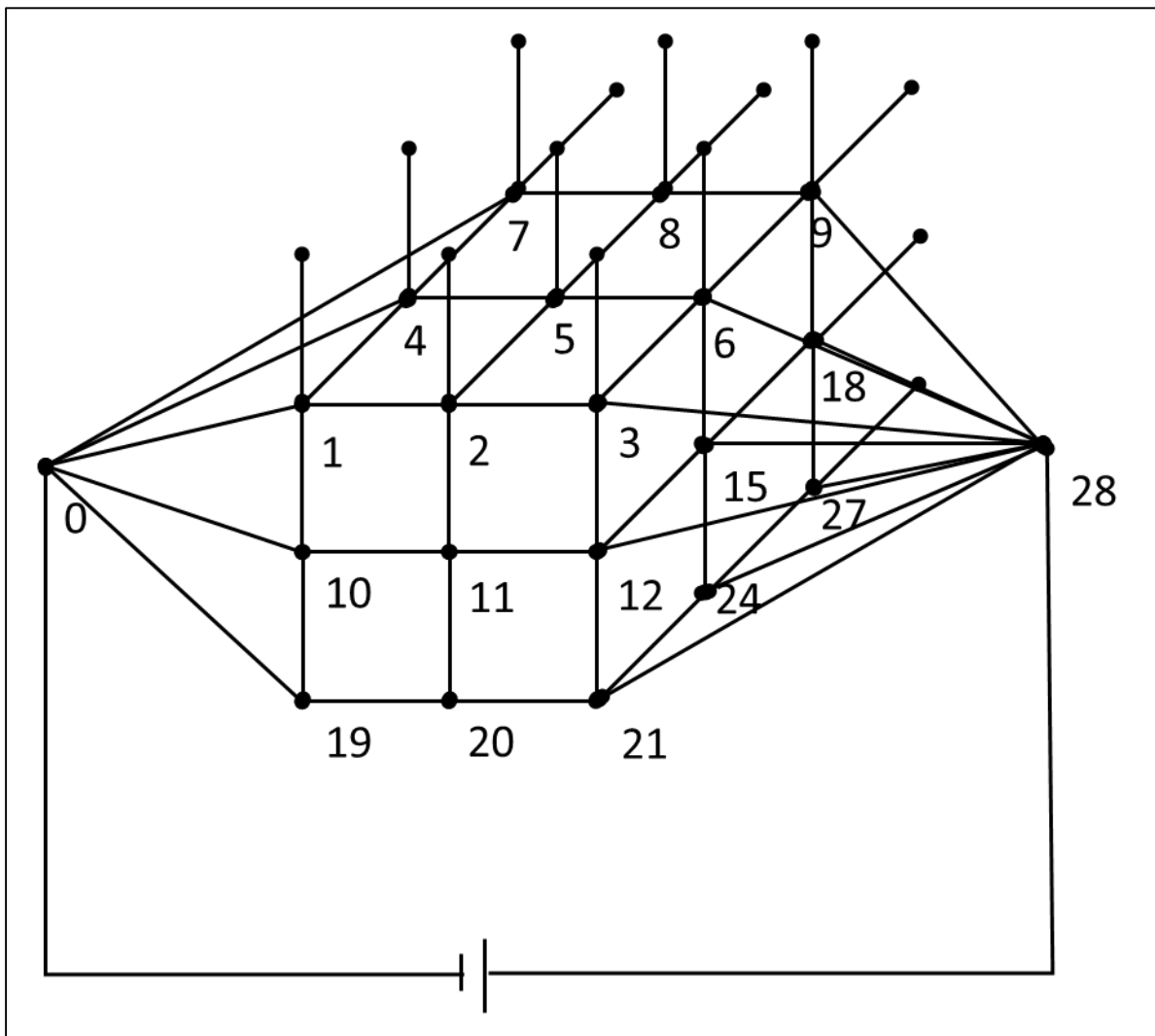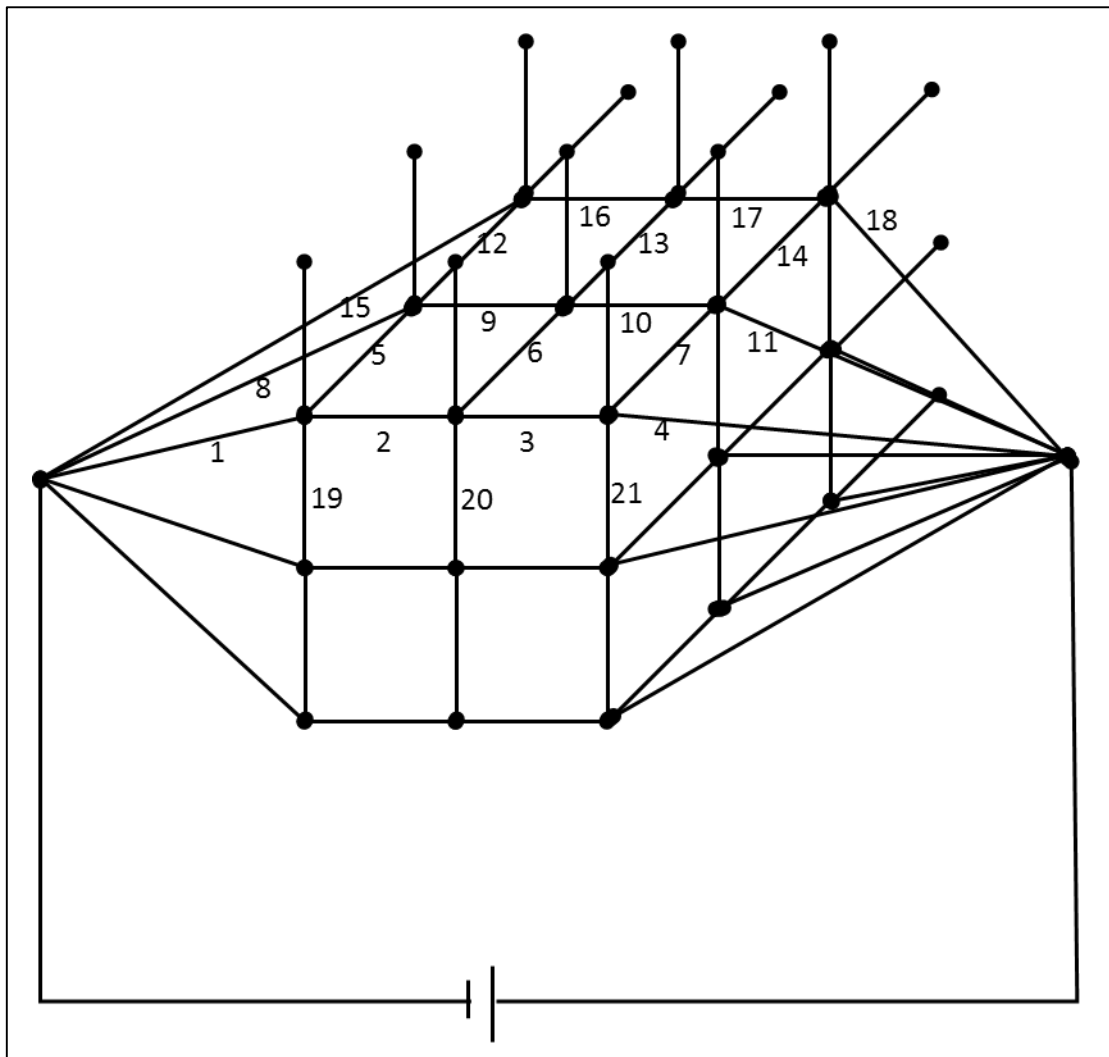

Figure B-1 – Numbering of nodes

Figure B-2 – Numbering of edges